

TECHNISCHE UNIVERSITÄT MÜNCHEN

Lehrstuhl für Grundwasserökologie

# Impact of organic acids and mineral properties on microbial iron oxide reduction

Juliane Braunschweig

Vollständiger Abdruck der von der Fakultät Wissenschaftszentrum Weihenstephan für Ernährung, Landnutzung und Umwelt der Technischen Universität München zur Erlangung des akademischen Grades eines

Doktors der Naturwissenschaften

genehmigten Dissertation.

Vorsitzende: Univ.-Prof. Dr. I. Kögel-Knabner

Prüfer der Dissertation:

1. Univ.-Prof. Dr. R. U. Meckenstock
2. Univ.-Prof. Dr. K. U. Totsche  
(Friedrich-Schiller-Universität Jena)

Die Dissertation wurde am 28.02.2013 bei der Technischen Universität München eingereicht und durch die Fakultät Wissenschaftszentrum Weihenstephan für Ernährung, Landnutzung und Umwelt am 12.06.2013 angenommen.



Zwei Dinge sind zu unserer Arbeit nötig: Unermüdliche Ausdauer und die Bereitschaft, etwas, in das man so viel Zeit und Arbeit gesteckt hat, wieder wegzuwerfen.

(Albert Einstein)

## Zusammenfassung

Die mikrobielle Reduktion von Eisenoxiden, wichtigen Bestandteilen in Böden und Sedimenten, gehört zu den wesentlichen anaeroben Atmungsprozessen im Untergrund. Umsatzraten dieses Prozesses werden von Eigenschaften der Eisenoxide bestimmt, mit weitreichenden Auswirkungen auf die Biogeochemie bis hin zur Grundwassersanierung. Biotische und abiotische Reaktivitäten von Eisenoxidmakropartikeln unterscheiden sich wesentlich von nanopartikulären Eisenoxiden, die für gewöhnlich eine höhere Reaktivität aufweisen. Partikelgröße, Löslichkeit, Fe(II), Kristallstruktur und organische Moleküle beeinflussen die Reaktivität. Arbeiten der letzten Jahre zeigten das hohe Potenzial von nanopartikulären Eisenoxiden in der Umwelt, beispielsweise als Elektronendonator für mikrobielle Atmungsprozesse oder als Adsorbens für Schwermetalle. Das Ziel der vorliegenden Arbeit war es, mineralogische Einschränkungen auf die abiotische und mikrobielle Reaktivität zu identifizieren und den Einfluss von niedermolekularen organischen Säuren auf die Löslichkeit und mikrobielle Verfügbarkeit von Eisenoxiden zu untersuchen. Außerdem wurden zwei häufig verwendete photometrische Eisenbestimmungsmethoden im Bezug auf Extraktionsverfahren und Störsubstanzen getestet.

Für die methodologische Untersuchung wurden synthetischer Goethit, Ferrihydrit und Pyrit, mikrobiell gebildeter Magnetit und eine Mischung aus Goethit und Magnetit sowie  $\text{Fe(II)}_{\text{aq}}$ -,  $\text{Fe(III)}_{\text{aq}}$ - und gemischt valente Lösungen verwendet. Die Güte der Ferrozin- und Phenanthrolin-Methoden wurde nach der Eisenextraktion in 1 M und 6 M HCl bei 21 und 60 °C unter oxidischen und anoxischen Bedingungen bestimmt. Beide Methoden erzielten gut reproduzierbare Eisenkonzentrationen, wobei Ferrozin für die Bestimmung von Gesamteisen und Phenanthrolin für Fe(II) geeigneter waren. Erhitzen der Proben und die Verwendung höherer Säurekonzentrationen verbesserten die Löslichkeit der kristallinen Eisenoxide, machten jedoch die anschließende Messung von Fe(II) durch schnelle abiotische Oxidation unmöglich. Deswegen ist es notwendig, vor der Fe(II)-Bestimmung das Eisen durch Auflösung in 1 M HCl bei 21 °C zu extrahieren und anschließend zu zentrifugieren, um Interferenzen ungelöster Eisenoxide mit dem photometrischen Reagens zu vermeiden.

Die Inkubation von synthetischen Ferrihydrit-Makroaggregaten mit Citrat als organische Modellsubstanz zeigte die Stabilisierung von Kolloiden im Größenbereich von 106 ( $\pm 6$ ) bis 202 ( $\pm 2$ ) nm für molare Citrat:Fe-Verhältnisse von 0,1 bis 0,5 sowie die partielle Auflösung von Ferrihydrit bei Citrat:Fe-Verhältnissen  $\geq 0,1$ . Es ist zu vermuten, dass die Adsorption von Citrat als Voraussetzung für die Auflösung des Ferrihydrits, zur elektrostatischen Abstoßung zwischen Subaggregaten des Ferrihydrits führte, sobald ein kritisches Citrat:Fe-Verhältnis ( $\sim 0,1$ ) überschritten wurde. Geringere Verhältnisse resultierten in stärkerer Aggregation des Ferrihydrits

anstelle von Kolloidstabilisierung infolge der Neutralisierung der positiven Oberflächenladung. Folglich erhöhte sich die mikrobielle Reduktion mit steigender Citratkonzentration um das Sechsfache von 0.03 auf 0.18 mM h<sup>-1</sup>. Die Modellierung der mikrobiellen Reduktion zeigte, dass Auflösung allein die erhöhten mikrobiellen Reduktionsraten nicht erklären kann. Vielmehr ist die Anwesenheit von stabil dispergierten Ferrihydrit-Kolloiden als leicht bioverfügbare Eisenphase notwendig, um die beobachteten Reduktionsraten zu erklären. Diese Ergebnisse demonstrieren die wichtige Rolle von niedermolekularen Säuren in Böden und Sedimenten, nicht nur für die Lösung von Mineralen, sondern auch für die Stabilisierung von Kolloiden.

Die Abhängigkeit der Reaktivität von Eisenoxiden von ihrer Mineralogie wurde mit fünf verschiedenen synthetischen Ferrihydriten in mikrobiologischen Batchexperimenten mit *Geobacter sulfurreducens* und abiotischen Lösungsexperimenten mit Ascorbinsäure untersucht. Die Proben wurden mittels Röntgendiffraktometrie, Fourier-Transformations-Infrarotspektroskopie, Röntgenphotoelektronenspektroskopie und N<sub>2</sub>-Physisorptionsmessungen charakterisiert. Die Ergebnisse deuteten darauf hin, dass der Grad der Aggregation einzelner Ferrihydrit-Kristallite die biotische und abiotische Reaktivität kontrollierte. Sobald Ferrihydritaggregate eine kritische Größe unterschritten, dominierten Oberflächeneigenschaften einzelner Kristallite den Auflösungsprozess. Fehlende Oberflächendefekte schienen die Bildung von Senken auf der Oberfläche zu behindern, die als Vorläufer von wellenförmig verlaufenden Lösungsstufen dienen. Die Auflösung größerer Aggregate wurde wiederum durch die Menge an Oberflächendefekten der Kristallstruktur bestimmt. Diese Ergebnisse deuten darauf hin, dass abnehmende Aggregatgrößen nicht zwangsläufig zur erhöhten Reaktivität von Ferrihydrit führen. Die Ergebnisse der vorliegenden Arbeit implizieren, dass die Reaktivität von Ferrihydrit mit abnehmender Aggregatgröße bis zu einem bestimmten Größenbereich (100-200 nm) steigt. Aufspaltung von Makroaggregaten durch niedermolekulare organische Säuren kann daher möglicherweise die Bioverfügbarkeit von Eisen in Böden erhöhen. Weitere Verringerung der Aggregatgröße unterhalb eines kritischen Bereichs vermindert die Reaktivität, da bestimmte Lösungsprozesse nicht mehr effektiv wirken können. Diese Beobachtung kann für technologische Anwendungen von Ferrihydrit von entscheidender Bedeutung sein, z. B. in der Sanierung von Grundwasserkontaminationen, ermöglicht aber auch einen tieferen Einblick in die Mechanismen der Interaktion zwischen Eisenoxiden und organischem Material in Böden und Grundwasser.

## Abstract

Iron oxides are important constituents of soils and sediments and microbial iron reduction is a major anaerobic respiration process in the subsurface. Turnover rates in this process are determined by the iron oxide particle properties with widespread implications from biogeochemistry to groundwater remediation. Biotic and abiotic reactivity of iron oxide macroparticles differs significantly from nano-sized Fe oxides, which are usually much more reactive. Particle size, solubility, ferrous iron, crystal structure, and organic molecules were identified to influence reactivity. Recent studies showed the high potential of nano-sized Fe oxides in the environment e.g. as electron donor for microbial respiration or scavenger for heavy metals. The aim of the thesis was to identify mineralogical constraints on abiotic and biotic iron oxide reactivity and to describe the influence of low molecular weight organic acids on iron oxide solubility and microbial accessibility. Furthermore, two commonly used photometric iron determination methods were tested regarding extraction procedures of different iron oxides and interfering substances.

Synthetic goethite, ferrihydrite, and pyrite, as well as microbially-formed magnetite and a mixture of goethite and magnetite and  $\text{Fe(II)}_{(\text{aq})}$ ,  $\text{Fe(III)}_{(\text{aq})}$ , and mixed valence solutions were used for the methodological approach. The performances of the ferrozine and phenanthroline assays were examined after iron extraction in 1 M and 6 M HCl at 21 and 60 °C and under oxic and anoxic conditions. Both methods revealed a good reproducibility of measured iron concentrations with ferrozine being more suitable for total iron and phenanthroline for ferrous iron. Heating of samples and higher acid concentrations increased solubility of crystalline iron oxides but fast abiotic oxidation of ferrous iron made subsequent ferrous iron determination impossible. Therefore, extraction prior to measurement of ferrous iron requires dissolution in 1 M HCl at 21 °C and subsequent centrifugation to avoid interferences of undissolved iron oxides with the photometric reagent.

Incubation of synthetic ferrihydrite macroaggregates with citrate as model organic compound revealed the formation of stably dispersed colloids in the size range of 106 ( $\pm 6$ ) to 202 ( $\pm 2$ ) nm for molar citrate:Fe ratios of 0.1 to 0.5 and partial dissolution of ferrihydrite at citrate:Fe ratios  $\geq 0.1$ . I hypothesize that adsorption of citrate, necessary for dissolution, led to electrostatic repulsion between sub-aggregates of the ferrihydrite over a critical citrate:Fe ratio ( $\sim 0.1$ ). Lower ratios resulted in stronger ferrihydrite aggregation instead of colloid stabilization owing to neutralization of the positive surface charge. Consequently, microbial ferrihydrite reduction increased sixfold with increasing citrate concentration from 0.03 to 0.18 mM  $\text{h}^{-1}$ . Modelling of microbial reduction revealed that dissolution alone did not totally explain the high microbial

reduction rates and that the presence of stably dispersed ferrihydrite colloids as highly bioavailable iron phase is essential for the observed reduction rates. These results demonstrated the important role of low molecular weight organic acids in soils and sediments not only for mineral dissolution but also for the stabilization of colloids.

Dependency of iron oxide reactivity on mineralogy was tested with five different synthetic ferrihydrites in microbial batch incubations with *Geobacter sulfurreducens* and abiotic dissolution experiments with ascorbic acid. Samples were characterized with X-ray diffraction, scanning electron microscopy, X-ray photoelectron spectroscopy, Fourier-transform infrared spectroscopy, and N<sub>2</sub>-physisorption measurements. Results indicated that the aggregation state of the ferrihydrite crystallites controlled biotic and abiotic reactivity. When ferrihydrite aggregate sizes dropped below a critical value, surface properties of the single crystallites dominated the dissolution process. Missing surface defects seemed to impede the development of pits on the surface which are the precursors of dissolution stepwaves. In turn, dissolution of larger aggregates was controlled by the amount of surface defects. These findings suggested that decreasing aggregate size does not necessarily lead to higher reactivities of ferrihydrite.

The results of the study imply that the reactivity of ferrihydrite increases with decreasing aggregate size up to a certain size range (100-200 nm). Disintegration of macroaggregates by low molecular weight organic acids can potentially increase the bioavailability of iron in soils. Further decrease of the aggregate size below a critical size diminishes the reactivity because certain dissolution processes cannot occur effectively. This observation is of importance for understanding the factors controlling microbial Fe(III) reduction, and also for the optimization of technological applications of ferrihydrite e.g. in groundwater contaminant remediation, but also opens a deeper view into the mechanisms of iron-organics interaction in soils and groundwater.

# Table of contents

<b>Zusammenfassung</b> .....	<b>i</b>
<b>Abstract</b> .....	<b>iii</b>
<b>Table of contents</b> .....	<b>5</b>
<b>1 Introduction</b> .....	<b>8</b>
1.1 Nano-sized minerals in global biogeochemistry .....	8
1.2 High reactivity of Fe oxide nanoparticles in geomicrobiological reactions: The role of solubility, surface area, and ferrous Fe .....	10
1.3 Impact of organic matter on reactivity of synthetic and environmental Fe oxide nanoparticles .....	14
1.4 Redox cycling of Fe .....	17
1.5 Transport of Fe oxide colloids .....	17
1.6 Fe oxide-based remediation technologies .....	19
1.7 Objectives of the thesis .....	21
<b>2 Materials and Methods</b> .....	<b>23</b>
2.1 Cultivation of microorganisms .....	23
2.2 Preparation of cell suspensions .....	24
2.3 Fe bearing solutions and minerals .....	25
2.3.1 Fe oxides and solutions prepared for the reevaluation of colorimetric Fe determination methods commonly used in geomicrobiology .....	25
2.3.2 Ferrihydrite used for the influence of low molecular weight organic acids on microbial Fe oxide reduction .....	25
2.3.3 Ferrihydrites used for the reduced biotic and abiotic reactivity of ferrihydrite nanoparticles below a critical aggregate size .....	26
2.4 Characterization of Fe oxides and organic substances .....	27
2.5 Reagents .....	29
2.5.1 Ferrozine assay .....	29
2.5.2 Phenanthroline assay .....	30
2.6 Experimental procedures for the reevaluation of colorimetric Fe determination methods commonly used in geomicrobiology .....	30
2.6.1 Influence of acid concentration on Fe extraction .....	30
2.6.2 Anoxic preparation of samples .....	31
2.6.3 Growth experiments .....	31
2.6.4 Influence of medium composition .....	32
2.6.5 Influence of light on ferrous Fe determination with ferrozine .....	32
2.6.6 Statistical analysis .....	32



2.7	Experimental procedures for the influence of low molecular weight organic acids on microbial Fe oxide reduction .....	33
2.7.1	Microbial reduction experiments .....	33
2.7.2	Abiotic dissolution experiments .....	33
2.7.3	Fe analysis .....	34
2.7.4	Calculation of dissolution and reduction kinetics .....	34
2.8	Experimental procedures for the reduced biotic and abiotic reactivity of ferrihydrite nanoparticles below a critical aggregate size .....	35
2.8.1	Abiotic dissolution in 1 M HCl .....	35
2.8.2	Abiotic reduction with ascorbic acid .....	36
2.8.3	Microbial reduction experiments .....	36
<b>3</b>	<b>Results .....</b>	<b>37</b>
3.1	Reevaluation of colorimetric Fe determination methods commonly used in geomicrobiology .....	37
3.1.1	Efficiency of total Fe determination .....	38
3.1.2	Ferrous Fe determination .....	40
3.1.3	Oxic vs. anoxic extraction .....	41
3.1.4	Growth experiments .....	41
3.1.5	Influence of medium composition .....	43
3.2	Low molecular weight organic acids influence microbial Fe oxide reduction via a dissolution-disaggregation mechanism .....	44
3.2.1	Sample characterization .....	44
3.2.2	Dissolution of ferrihydrite and particle stabilization .....	46
3.2.3	Microbial reduction by <i>G. sulfurreducens</i> .....	47
3.2.4	Calculation of dissolution and reduction kinetics .....	49
3.3	Reduced biotic and abiotic reactivity of ferrihydrite nanoparticles below a critical aggregate size .....	50
3.3.1	Characterization of synthesized Fe oxides .....	50
3.3.2	Reduction kinetics .....	52
3.3.3	Abiotic dissolution in 1 M HCl .....	53
<b>4</b>	<b>Discussion .....</b>	<b>56</b>
4.1	Reevaluation of colorimetric Fe determination methods commonly used in geomicrobiology .....	56
4.1.1	Quantification of total Fe content .....	56
4.1.2	Ferrous Fe determination .....	58
4.2	Low molecular weight organic acids influence microbial Fe oxide reduction via a dissolution-disaggregation mechanism .....	60
4.2.1	Sample characterization .....	60
4.2.2	Dissolution and colloid stabilization .....	60

4.2.3	Microbial reduction of ferrihydrite in the presence of citrate .....	63
4.3	Reduced biotic and abiotic reactivity of ferrihydrite nanoparticles below a critical aggregate size .....	64
4.3.1	Secondary minerals .....	64
4.3.2	Influence of specific surface area and micropores on initial reduction rates .....	65
4.3.3	Adsorbed anions .....	65
4.3.4	The role of adsorbed Fe <sup>2+</sup> .....	67
4.3.5	Structural properties of ferrihydrite .....	67
4.3.6	Dissolution self-inhibition for small aggregates .....	68
<b>5</b>	<b>Summary, conclusions, and outlook .....</b>	<b>70</b>
	<b>References .....</b>	<b>76</b>
	<b>Appendix .....</b>	<b>I</b>
	<b>Authorship clarifications .....</b>	<b>XVII</b>
	<b>Publications .....</b>	<b>XIX</b>
	<b>Acknowledgments .....</b>	<b>XX</b>

# 1 Introduction<sup>1</sup>

## 1.1 Nano-sized minerals in global biogeochemistry

Iron (Fe) is one of the most abundant elements of the earth's crust and therefore ubiquitous in many biogeochemical compartments. Fe oxides occur in the atmosphere, pedosphere, biosphere, hydrosphere, and lithosphere in a great diversity of morphologies, minerals, and associations [1, 2]. They appear as anhydrous forms like hematite ( $\alpha\text{-Fe}_2\text{O}_3$ ) and maghemite ( $\gamma\text{-Fe}_2\text{O}_3$ ), mixed-valent oxides like magnetite ( $\text{Fe}_3\text{O}_4$ ) and wuestite ( $\text{Fe}_{1-x}\text{O}$ ), and oxyhydroxides with the common formula  $\text{FeOOH}$  (goethite, lepidocrocite, akaganeite). More hydrated forms like ferrihydrite with variable water contents are often described as  $\text{Fe}(\text{OH})_3$  [3] (referred to as Fe oxides in this thesis).

Like many environmental minerals, Fe oxides also occur as nanoparticles. Nanoparticles have a size of one to several tens of nanometers (but smaller than 1  $\mu\text{m}$ ) in three dimensions [4]. Stably dispersed in a medium like water, such nanoparticles are defined as colloids [5]. According to the DLVO theory, aggregation is inhibited if electrostatic repulsion forces dominate over van der Waals attraction [6, 7]. Owing to the balance between gravity and buoyancy, colloids do not sediment. When Fe oxide minerals form by precipitation from ferrous solutions, their primary nucleation sites are within the nanometer range. Ferrihydrite, as an exceptional Fe oxide, is a nanomineral that only exists in nanometer-sized crystallites [4]. Those crystallites form aggregates of 100-300 nm (nanoaggregates) [8] which may have colloidal properties. Ferrihydrite

---

<sup>1</sup> This chapter was accepted with minor revisions by the journal *New Biotechnology* on 12.02.2013

macroaggregates larger than 1  $\mu\text{m}$  [9] are formed by agglomeration of nanoaggregates and do not form stable suspensions but precipitate in aqueous solutions. For other Fe oxides, the nanoparticle stage is naturally a transitory phase to macroparticle growth [4], defined here as particles larger than 1  $\mu\text{m}$ . However, the growth process can be interrupted by e.g. depletion of the ferrous source or complexation of ferric or ferrous Fe with organic matter, leading to a decrease of the mineral saturation index [10]. Solid, bulk minerals in contrast are exposed to shearing, straining, weathering, and a multitude of other dissolutive reactions [11], also yielding nanoparticles. Therefore, a fraction of the global pool of environmental Fe minerals is constantly present as nanoparticles [12]. A study with sediment from the Mediterranean Sea revealed an abundance of nano-sized goethite of 7 to 30% of the total Fe in dependence of sampling site and depth [13].

In soils and aquifers, chemical or physical perturbation of the ambient groundwater conditions can lead to mobilization of already existing nano-sized minerals [14]. This raises questions on the reactivity of this fraction in global biogeochemistry.

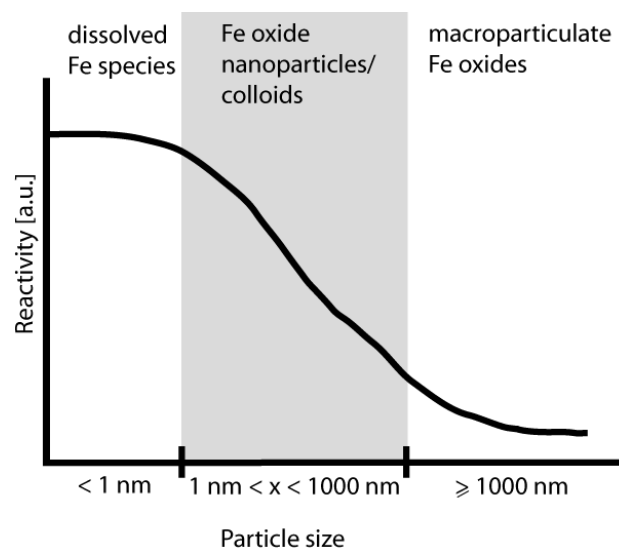
The reactivity and the role of Fe oxides in the environment might have been underestimated until now because at particle sizes within the nanometer range minerals show variations in their crystal structure as compared to their macroparticulate counterparts. With particle size decreasing to the nanometer-range, physical, chemical, and magnetic properties can change [1, 15, 16]. Several studies indicate that these effects have an impact on the reactivity of nanominerals in microbial redox reactions. Anaerobic microbial oxidation of pyrite ( $\text{FeS}_2$ ) by *Thiobacillus denitrificans* was observed with pyrite nanoparticles but not with larger crystals [17], indicating that minerals which do not react as macroparticles may become reactive in nanoparticulate forms. Another example showed that the oxidation of  $\text{Mn}^{2+}$  on hematite surfaces was up to 1.5 orders of magnitude faster for 7.3-nm hematite relative to 37-nm hematite, resulting in a faster formation of Mn oxides [18]. In the environment, the fast mineralization of Mn induced by Fe oxide nanoparticles probably leads to a much faster increase of available adsorption surface sites for heavy metal uptake than previously assumed. Furthermore, the thermodynamic stabilities of Fe oxides relative to the formation of other Fe oxides were shown to be a function of surface area and therefore particle size [3].

## 1.2 High reactivity of Fe oxide nanoparticles in geomicrobiological reactions: The role of solubility, surface area, and ferrous Fe

Factors controlling microbial Fe oxide reduction were intensively studied during the last decades and several key factors for Fe oxide reactivity were identified. Maximum microbial reduction rates by *S. putrefaciens* were positively correlated with the solubility of Fe oxides in the order amorphous Fe(III) oxide (2-line ferrihydrite)  $\geq$  6-line ferrihydrite  $\gg$  nanohematite = lepidocrocite  $\gg$  goethite  $>$  macroparticulate hematite [19-21]. According to the modified Kelvin equation, the solubility of minerals increases exponentially with decreasing particle size to the nanometer-scale (Fig. 1.1) [16, 22]:

$$\frac{S}{S_0} = e^{\frac{2\gamma V}{RT r}} \quad (\text{eq. 1.1})$$

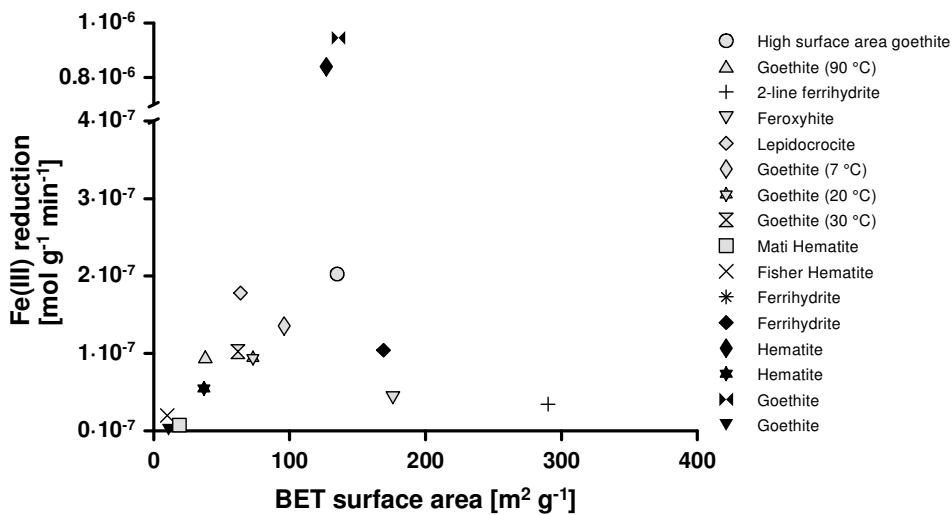
where  $S$  is the solubility ( $\text{mol kg}^{-1}$ ) of fine grains with the radius  $r$  (m),  $S_0$  is the solubility of the bulk material.  $\gamma$  is the surface free energy ( $\text{mJ m}^{-2}$ ),  $V$  is the molecular volume ( $\text{m}^3 \text{mol}^{-1}$ ),  $R$  is the universal gas constant ( $\text{mJ mol}^{-1} \text{K}^{-1}$ ), and  $T$  is the temperature (K). This indicates in conclusion that decreasing particle size enhances solubility, which in turn increases microbial reduction rates. However, it is not known how generally applicable this is for all minerals. Some minerals like e.g. hydroxyapatite became less soluble with particle sizes decreasing to a critical value [23]. The critical value depended on the size of pits on the crystallite surface which induced the dissolution of hydroxyapatite. When the crystallite sizes were in the same order as the formed pits, dissolution became self-inhibiting.



**Fig. 1.1:** Generalized trend of Fe oxide reactivity in dependence of particle size. (modified from [24])

In general, one should distinguish between large crystal sizes and aggregates of smaller particles. The solubility, mostly tested under acidic conditions and thereby leading to disaggregation (e.g. [21, 25]), is dependent on the crystal size and largely independent on the aggregate size of precipitated nanoparticles [21, 26].

A study by Roden [25] showed that the rate-limiting steps of abiotic reductive dissolution by ascorbate for a wide set of amorphous, nanoparticulate and highly crystalline, macroparticulate Fe oxides were different from microbial reduction by *S. putrefaciens*. Comparison of the specific surface areas of different Fe oxides with their reduction rates showed an approximately linear relationship for microbial reduction whereas the relationship for abiotic reduction was logarithmic (Fig. 1.2). This logarithmic behavior was attributed to differences in the thermodynamic properties (e.g. crystal order) which are correlated with the specific surface area and the Fe(II) detachment from Fe oxide surfaces during reduction. The linear relationship between microbial reduction rates and the specific surface area indicated that the rate-limiting step in microbial Fe oxide reduction was the rate of electron transfer from the cell to the Fe oxide surface. In contrast to abiotic reduction, microbial reduction led to an Fe(II) coating on the Fe oxide surfaces. Outliers showing a low reactivity compared to specific surface area (Fig. 1.2) were most likely caused by strong aggregation [25].



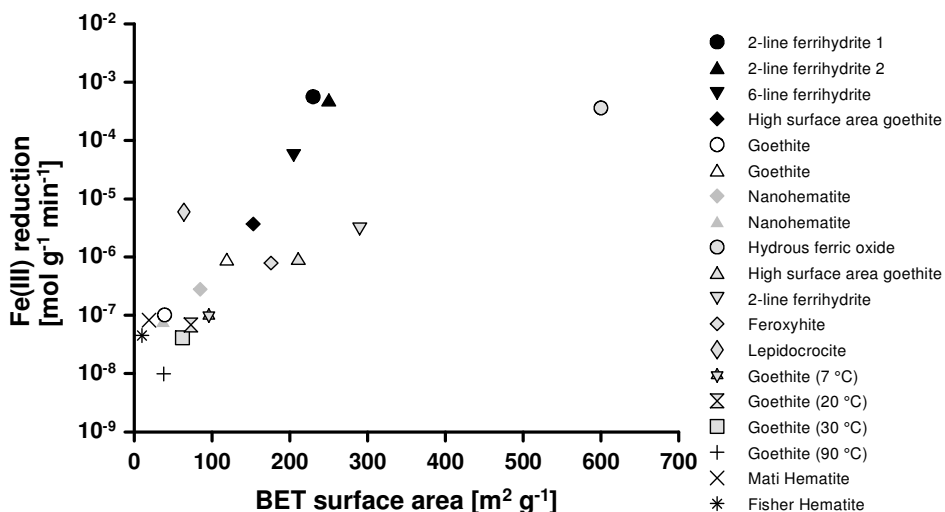


**Fig. 1.2:** Relationship between oxide surface area and initial microbial (A) and abiotic reduction rates (B). Different experimental procedures in respective studies (e.g. different microorganisms or reducing agents) cause different slopes but approximately linear and logarithmic correlations are discernible for biotic and abiotic reduction, respectively. (Data taken from [25] and Tab. 1.1).

Recent studies investigated the abiotic dissolution behavior of hematite nanoparticles in the size-range between 7 to 40 nm [22, 26]. Initial reduction rates of 7 and 8 nm-hematites were triggered by dispersed and rapidly dissolved particles and exceeded initial reduction rates of 30 and 40 nm particles by 2- to 10-fold. Here, reduction was mainly initiated by internal defects and nanoscale surface steps. This indicates that not only the specific surface area and the Fe(II) detachment from the surface control the initial reduction rates, but also structural defects and surface roughness. Especially the reduction rates of environmental nanoparticles are very likely underestimated. They precipitate in the presence of ions and organic molecules and are therefore characterized by defect structures [27] (Fig. 1.3).

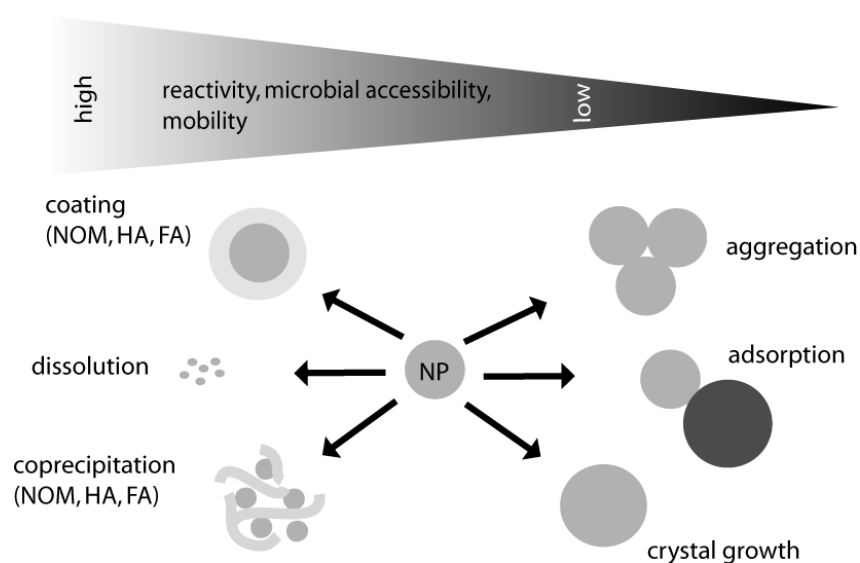


**Fig. 1.3:** Possible interactions of nanoparticles in the environment or laboratory systems. NOM = natural organic matter, HA = humic acids, FA = fulvic acids (modified from [28]).

In accordance with both findings, the microbial reduction rates of differently sized hematite nanoparticles by *G. sulfurreducens* decreased in the order 30 nm > 10 nm > > 50 nm due to stronger aggregation of the 10 and 50 nm particles compared to the 30 nm particles [29] (Fig. 1.3). Aggregation diminished the specific surface area and therefore the number of available Fe(III) centers at the Fe oxide surfaces available for the electron issuing sites of the cell membranes [25]. Direct Fe(III) reduction by microorganisms requires attachment of the cells to the nanoparticles [19, 20, 30], but reduction kinetics of larger aggregates might subsequently be controlled by crystal properties [22, 31]. The latter studies observed no influence of the aggregation behavior of hematite nanoparticles on microbial reduction rates. Initial reduction rates of 30 and 43 nm particles were similar to rates of 500 nm aggregates, even though the large aggregates presented less surface area for cell contact. Thus, not only particle size but also particle morphology, shape, and the degree of aggregation seem to determine both the contact between Fe oxides and cells and the reduction mechanism (e.g. direct or indirect electron transfer) used by *S. oneidensis*.

However, higher microbial reduction rates of colloidal Fe oxides compared to their macroparticulate counterparts have been observed [32, 33]. The microbial reduction of different Fe oxide colloids by *G. sulfurreducens* was up to two orders of magnitude faster compared to the macroparticulate oxides of the same mineral (Tab. 1.1). Surprisingly, all colloidal Fe oxides were almost totally reduced, to extents of 78 to 100% [33]. The high biotic reactivity of different Fe oxide nanoparticles was also proven with soil microbial communities grown in electrochemical cells [34]. Amendment of Fe oxide nanoparticles to the electrochemical cells led to an > 30-fold increase in current production, probably caused by constructed electrically conductive networks between microbial cells, Fe oxide nanoparticles, and electrodes. The authors assumed that it is likely that only nanoparticles can take this role because larger crystals cannot get into the intercellular spaces of microbial assemblages to form electron conduits. Furthermore, the ability of electrically conductive nano-magnetite to facilitate electron transfer between *G. sulfurreducens* to *Thiobacillus denitrificans* was recently shown [35]. These findings indicate the important and diverse functions of Fe oxide nanoparticles as electron acceptor and electron mediator in nature due to their high bioavailability.



### 1.3 Impact of organic matter on reactivity of synthetic and environmental Fe oxide nanoparticles

The mechanisms of microbial Fe oxide reduction as discussed above were investigated with synthetic Fe oxides in artificial laboratory systems. In nature, not only Fe oxides but many other minerals are commonly associated with organic molecules [36-38]. This leads to the question whether this association limits or accelerates microbial reduction rates of naturally occurring Fe oxides.

Humic acids, extracts of natural organic matter at strong alkaline conditions, were reduced by Fe-reducing organisms belonging to the family of the *Geobacteraceae* with acetate as sole electron donor [39-41]. The electron accepting capacity of humic acids and especially their quinone moieties seemed to enable humic substances to enhance microbial reduction of Fe oxide macroparticles via electron shuttling between cells and minerals. This was observed with dissolved and solid-state humic acids [42].

The abiotic electron transfer from reduced organic molecules to Fe oxides is essential for this mechanism. Chen et al. [43] proved that polyphenylic-rich and carbohydrate-rich fractions of aquatic natural organic matter from a wetland pond, and soil humic acids were able to partly reduce dissolved Fe(III) and an amorphous Fe(III) precipitate abiotically at acidic (pH < 4) but also at neutral pH values. Electron transfer from microbially reduced humic acids to ferrihydrite turned out to be at least 7-fold faster than the electron transfer from *G. sulfurreducens* to ferrihydrite macroaggregates [44] (Fig. 1.3). Redox potentials of quinones are a controlling factor in electron shuttling-mediated Fe oxide reduction, with redox potentials of most effective quinones in a range of -137 to -225 mV vs. standard hydrogen electrode at pH 7 [45].

In aquatic systems, small fulvic compounds (0.8 – 3 nm) adsorb on inorganic colloids and prevent aggregation by electrostatic repulsion. Thus, Fe oxide nanoparticles can be stabilized in suspension in the environment [46-48]. In contrast, adsorption of large rigid biopolymers (consisting of structural and fibrillar polysaccharides with total lengths up to 1  $\mu\text{m}$ ) destabilized colloids due to formation of larger aggregates [46, 47]. Biopolymers acted as long distance bridges between single colloids and formed loose aggregates of large dimensions. Smaller polymers also adsorbed on colloidal Fe oxide surfaces. However, charge neutralization of the Fe oxides led to the collapse of colloids rather than polymer bridging [46]. A stabilizing effect was also observed for goethite colloids coated with tannic and polygalacturonic acid whereas colloids coated with dissolved organic matter formed large aggregates [49]. In summary, stabilization of nanoparticles by electrostatic repulsion as well as aggregation by polymer bridging affect the specific surface areas of the nanoparticles and therefore also their reactivity.

In natural systems, Fe oxide colloids generally form in the presence of natural organic matter, leading to distorted crystal structures [50-52]. For example, complexation of Fe(II) and Fe(III) inhibited hydrolysis and therefore Fe oxide formation [53-56]. Coprecipitation experiments of Fe(III) nitrate solutions with different hydroxybenzoic acids showed that especially the position rather than the number of phenol groups of the respective acid controlled the interaction with Fe(III) and was therefore decisive for the formed crystallite sizes [55]. Two-line ferrihydrite macroaggregates coprecipitated with microbial exopolysaccharides revealed no changes of Fe(III) coordination, but a slightly reduced crystallite size and crystallinity [57]. Water extractable natural organic matter from a forest topsoil interfered strongly with the crystal growth of synthetic ferrihydrite during coprecipitation [58]. Even small amounts led to smaller ferrihydrite crystallites, increased lattice spacings, and more distorted  $\text{Fe}(\text{O},\text{OH})_6$  octahedra. Furthermore, organic ligands like citrate, oxalate, but also humic acids and natural organic matter increased the solubility of Fe oxides [59-61]. In a structural study of natural ferrihydrite from an acid mine drainage environment, increasing Al, Si, and organic matter contents caused decreasing crystallite size, while an increase of structural disorder occurred [62]. Aluminum substituted  $\text{Fe}^{3+}$  while Si and organic matter coprecipitated with ferrihydrite inhibited Fe polymerization and particle growth. This led to additional structural disorder. Coprecipitation of ferrihydrite macroaggregates with acid polysaccharides affected the surface reactivity of ferrihydrite due to the increase of accessible surface area for dissolving ligands like citrate. Coprecipitation therefore controlled ligand-promoted dissolution at neutral pH [63].

All the discussed factors and heterogeneities occurring in nature have the potential to accelerate microbial Fe oxide reduction. Natural ferrihydrite colloids, derived from a soil column experiment were precipitated in the presence of natural organic matter and applied to microbial reduction experiments [9]. Microbial reduction rates of natural colloids exceeded reduction rates of synthetic ferrihydrite macroaggregates in literature by about two orders of magnitude and were almost similar to dissolved ferric Fe species like ferric citrate. The fast reduction stemmed from the increased solubility of ferrihydrite induced by incorporated natural organic matter. Furthermore, complexed Fe(III) was readily bioavailable for microbial cells and enhanced initial microbial reduction [64]. Similar results with synthetic lepidocrocite nanoparticles precipitated in the presence and absence of humic and fulvic acids were obtained by Pédrot et al. [60]. Here, microbial reduction with *S. putrefaciens* led to an 8-times faster reduction of the coprecipitated lepidocrocite compared to the pure lepidocrocite. Furthermore, natural organic molecules increase the potential of abiotic photochemical reduction of Fe oxides by the generation of highly reactive intermediates (e.g. organic radicals) and reactive oxygen species (e.g. singlet oxygen, hydrogen peroxide, hydroxyl radicals) [10, 65].

**Tab. 1.1:** Comparison of initial biotic and abiotic reduction rates of different Fe oxides from literature.

Fe oxide	Particle/aggregate size [nm]	Specific surface area [m <sup>2</sup> g <sup>-1</sup> ]	Reducing agent	Abiotic reduction rate [mol m <sup>-2</sup> min <sup>-1</sup> ]	Microorganism	Cell density [cells mL <sup>-1</sup> ]	Biotic reduction rate [mol m <sup>-2</sup> min <sup>-1</sup> ]	source
2-line ferrihydrite 1	3.29	230	Ascorbic acid	2.46E-06	-	-	-	[21]
2-line ferrihydrite 2	3.03	250	Ascorbic acid	1.98E-06	-	-	-	[21]
6-line ferrihydrite	3.70	205	Ascorbic acid	2.70E-07	-	-	-	[21]
High surface area goethite	10.67	153	Ascorbic acid	2.40E-08	-	-	-	[21]
Goethite	(1006 ± 55) <sup>1</sup> x (43 ± 7) <sup>2</sup>	39 ± 2	HNO <sub>3</sub>	2.61E-09	-	-	-	[66]
Goethite	(75 ± 20) <sup>1</sup> x (10 ± 3) <sup>2</sup>	119 ± 3	HNO <sub>3</sub>	7.70E-09	-	-	-	[66]
Nanohematite	6.8 ± 0.8	84.7 <sup>3</sup> , 117.5 <sup>4</sup>	Ascorbic acid	3.27E-09	-	-	-	[22]
Nanohematite	30.5 ± 3.5	37.1 <sup>3</sup> , 39.1 <sup>4</sup>	Ascorbic acid	2.15E-09	-	-	-	[22]
Hydrous ferric oxide	1.3	600	Ascorbate	6.05E-07	<i>Shewanella putrefaciens</i> CN32	2.0E+08	3.97E-09	[25]
High surface area goethite	7.7	211	Ascorbate	4.92E-09	<i>Shewanella putrefaciens</i> CN32	2.0E+08	1.21E-09	[25]
Goethite (90 °C)	43.4	38	Ascorbate	2.59E-10	<i>Shewanella putrefaciens</i> CN32	2.0E+08	2.52E-09	[25]
Ferrihydrite	336 ± 40	275 ± 0.6	-	-	<i>Geobacter sulfurreducens</i>	2.1E+08	5.49E-08	[33]
Ferrihydrite	70,200 ± 30%	169 ± 0.3	-	-	<i>Geobacter sulfurreducens</i>	2.1E+08	6.17E-10	[33]
Hematite	123 ± 4	127 ± 1.1	-	-	<i>Geobacter sulfurreducens</i>	2.1E+08	6.62E-09	[33]
Hematite	27,600 ± 30%	37 ± 0.9	-	-	<i>Geobacter sulfurreducens</i>	2.1E+08	1.48E-09	[33]
Goethite	64 ± 3	136 ± 0.5	-	-	<i>Geobacter sulfurreducens</i>	2.1E+08	6.95E-09	[33]
Goethite	11,900 ± 30%	11 ± 0.1	-	-	<i>Geobacter sulfurreducens</i>	2.1E+08	1.33E-10	[33]
Soil effluent ferrihydrite	281 ± 146	n.d.	-	-	<i>Geobacter sulfurreducens</i>	4.8E+07	160 μM h <sup>-1</sup>	[9]
Soil effluent ferrihydrite	100 ± 43	n.d.	-	-	<i>Geobacter sulfurreducens</i>	4.8E+07	93 μM h <sup>-1</sup>	[9]

<sup>1</sup>length <sup>3</sup>degassed for 4 h at 120 °C under N<sub>2</sub> flow before measurement

<sup>2</sup>width <sup>4</sup>degassed for 4 h at 90 °C under N<sub>2</sub> flow before measurement

## 1.4 Redox cycling of Fe

The production of biogenic dissolved Fe(III) or colloidal Fe oxides by Fe(II)-oxidizing bacteria and its depletion by Fe(III)-reducing bacteria occur simultaneously within the same sediment layer [67, 68]. A sustained Fe redox cycling was already proposed for different redox interfacial habitats like hot springs and hydrothermal vents [69, 70], at sediment-water interfaces in aquatic ecosystems under circumneutral [67, 68] and acidic conditions [71], plant roots [72, 73], and groundwater Fe seeps [74]. Synthetic Fe oxides inoculated with cocultures of Fe(II)-oxidizing and Fe(III)-reducing microorganisms [67] or enrichment cultures of freshwater sediment microorganisms [75, 76], showed repeated reduction of goethite nanoparticles or ferrihydrite aggregates. This was observed in co-occurrence with Fe(II) oxidation at oxic-anoxic interfaces. These findings were supported by Bloethe and Roden [74] who could show the rapid Fe oxide reduction and the subsequent Fe(II) oxidation in freshly collected, anaerobic seep material. A conceptual model for the bacterial Fe redox cycling is based on the close juxtapositioning of Fe(II)-oxidizing bacteria and Fe(III)-reducing bacteria in cocultures within the Fe(II)-O<sub>2</sub> reaction zone [67, 68]. Here, clumping of Fe(II)-oxidizing and Fe(III)-reducing bacteria around Fe oxide aggregates suggested that Fe(III)-reducers take advantage of anaerobic microzones within the aggregates. These microzones are generated by O<sub>2</sub>-scavenging during microbial Fe(II) oxidation, leading to “ultramicrogradients” of O<sub>2</sub> at the surface of the aggregates. Anoxic conditions at the aggregate surface allow proceeding Fe(III) reduction within a bulk aerobic environment.

The higher reactivity of Fe oxide nanoparticles compared to their macroparticulate counterparts suggests that the efficiency of Fe redox cycling strongly depends on their availability. Recently a field site study proved Fe redox cycling within a floating puffball structure. The authors assumed, based on a former scanning electron microscopy study from the same site [77], that nanometer-sized amorphous Fe oxide particles are the ferric Fe source in this process [78]. Therefore, it is likely that nanoparticulate Fe oxides are a driving force in the Fe redox cycling process in the environment due to their high reactivity.

## 1.5 Transport of Fe oxide colloids

Organic and inorganic colloids have a significant impact on pollutant, trace element, heavy metal, and radionuclide mobilization in soils and groundwater due to adsorption or incorporation [14, 79-82]. During the last decades many laboratory studies were conducted to get insights into mechanisms and factors controlling mobility of colloids [83-87] and the concomitant co-

transport of trace elements and pollutants [88-92]. Experiments with columns filled with quartz sand and Fe oxide colloids [80] or with natural soil [79, 93] demonstrated the strong association of numerous elements (e.g. Ti, U, Pb, Ga, rare earth elements, Y, Cd, V, Sn) to Fe oxide colloids. Chemical mobilization of colloidal Fe oxides and other minerals occurs mainly in response to decreasing ionic strength, increasing pH and increasing concentrations of dissolved organic carbon or surfactants. Infiltration of dilute precipitation water, irrigation or injection of fresh water for secondary oil extraction leads to the decrease of the ionic strength, an increase of repulsive electrostatic forces, and therefore to the mobilization of colloids. With pH values of 6 to 9, infiltrating water decreases the hydraulic conductivity of soils through clay dispersion. Surfactants introduced to aquifers e.g. for enhancement of oil recoveries or remediation of contaminated aquifers but also infiltration of organic matter-rich groundwater from swampy streams can cause colloid mobilization [14]. Colloid formation occurs very often in contaminant plumes. Here, high concentrations of organic acids, organic macromolecules, and reductants promote the mobilization of colloids [14]. Physical perturbation is mainly induced by increased flow velocities, e.g. in fractured media or induced by pumping [14].

The stability of colloids against aggregation is essential for their transport and fate in porous media. The stability of colloidal systems can be predicted by the DLVO theory based on repulsive electrostatic forces and attractive van der Waals forces [6, 7]. Strength of these forces depends mainly on ionic strength, pH, surface charge, and presence of adsorbed polymers. At high ionic strength (~100 mM) [94] the electric double layer shrinks and repulsive electrostatic forces diminish, leading to irreversible aggregation. Depending on the initial thickness of the electrical double layer, moderate ionic strength (10-30 mM) leads to an excess of van der Waals attraction. This results in the formation of a weaker secondary minimum where colloids can reversibly agglomerate to unstable aggregates [94]. Simulations have shown that an absolute value of surface potential, diffuse layer potential, and zeta potential of at least 25 mV stabilizes metal oxide nanoparticles over a huge range of ionic strengths [95]. Pure synthetic amorphous Fe oxide colloids are therefore predicted to be stable only in rainwater and in extreme pH river water because higher ionic strength causes immediate aggregation [96]. Coatings of natural organic matter prevented metal colloids effectively from aggregation because they induced a strongly negative surface charge [95] (Fig. 1.3).

Other factors controlling the mobility of colloids are hetero-domains of attractive surface charge and roughness of the surfaces [97] as well as particle and pore sizes [98]. During the last decades, these interactions were mostly investigated in laboratory systems with glass beads and/or quartz sand as porous media and latex particles [94, 98, 99]. Apart from enhanced retention at high ionic strength, retention was increased at large colloid sizes relative to pore sizes [98]. Under

unsaturated conditions, repulsive interactions between colloids and the liquid-gas interface (e.g. air bubbles) help to overcome repulsive forces between colloids and the porous medium [100]. Requirements for retention were thin water films of a thickness comparable to the colloid diameters. Transport behavior of synthetic ferrihydrite colloids in quartz sand depended on different ionic strengths and flow velocities. At low ionic strength ( $< 5$  mM) the influence of the flow rate on particle deposition was negligible, but became more important with increasing ionic strength [101]. The authors calculated travel lengths in clean groundwater (ionic strength  $\sim 2$ -5 mM) of 10-20 m. Increasing ionic strength (up to 10 mM) resulted in a calculated travel distance of a few meters. These findings were in accordance with results on hematite colloids with and without coatings of natural organic matter [102]. Natural organic matter increased stabilization of colloids against aggregation in NaCl-containing solutions. No stabilizing effect was observed in the presence of  $\text{CaCl}_2$ , according to the Schulze-Hardy rule. Furthermore,  $\text{Ca}^{2+}$  is well known to act as bridging agent between humic acids coated ferrihydrite colloids and therefore to promote aggregation [103].

## 1.6 Fe oxide-based remediation technologies

Recent and historical industrial and agricultural activities led to numerous sites with elevated contaminant concentrations in soils, sediments, surface-, and groundwater. In 2007 the European Environment Agency (EEA) estimated 250,000 soil contaminated sites where remediation was required [104]. Widespread contaminants are trace elements, metalloids, and aromatic, polyaromatic, and chlorinated organic compounds. During the last decades Fe oxides were drawn into focus of the development of new remediation technologies due to their sorptive and reactive character [105]. *In-situ* Fe based treatment methods are potentially cost-effective remediation options (Tab. 1.2) [106].

**Tab. 1.2:** Different Fe-based remediation technologies: stage of development, mode of application, and estimated costs (modified from [106]).

Technology	Stage of development	<i>In-situ</i> or <i>ex-situ</i>	Remedial mechanism	Estimated cost (US \$)
Assisted natural remediation	Laboratory and pilot field trials	<i>In-situ</i>	Contaminant immobilization	Likely to be relatively low (<\$50 per ton material treated)
Chemical reduction via addition of Fe(II)-containing solutions	Commercial systems available	<i>In-situ</i> or <i>ex-situ</i>	Reductive precipitation	Cost varies depending on surrounding conditions. \$250,000-\$300,000 per site
Permeable reactive barriers	Commercial systems available	<i>In-situ</i>	Sorption or degradation in barrier	\$60-\$245 per ton material treated

Permeable reactive barriers (PRB) are engineered zones below the water table. The intention is to remove dissolved groundwater contaminants by immobilization, by adsorption or transformation to less harmful products [107]. The materials within the barrier of PRBs depend on the respective contaminant. Iron oxides are used for the removal of e.g. U, Mo, and Cr by adsorption and the chemical reduction of nitroaromatics and dechlorinated aliphatics [107]. Iron oxides have a significant impact on the fate of organic contaminants via oxidative and reductive transformation processes [108]. Structural and mineral-bound Fe(II) reduces chlorinated hydrocarbons and nitroaromatic compounds [109-116]. Interestingly, no size-effect was observed for Fe(II)-mediated abiotic reduction of nitrobenzene with goethite nanoparticles between 7-670 nm after specific surface area normalization [117]. However, the authors explain this observation with aggregation of the particles and that the BET values should not be used for the determination of surface site densities of aggregated particles.

The dechlorination reaction of carbon tetrachloride by microbially formed nano-magnetite in a study of McCormick et al. [118] was estimated to be 260-fold faster than the enzymatic degradation by *G. metallireducens*. Similar results were found by Tobler et al. [119]. Ferrous Fe, formed during the microbial oxidation of toluene with amorphous Fe oxides as electron acceptor by *G. metallireducens*, bound to highly crystalline, macroparticulate Fe oxide surfaces and led to abiotic reduction of 4-nitroacetophenone. Both results indicate the potential of ferrihydrite nanoaggregates as highly reactive material by coupling fast microbial Fe oxide reduction and abiotic Fe(II)-induced reduction of organic contaminants. Use of highly reactive nano-sized Fe oxides could putatively increase the efficiency of the aforementioned remediation technologies.

Arsenic is a widespread natural occurring contaminant especially in inland or closed basins in arid or semi-arid regions, in strongly reducing aquifers, or in geothermal and mining areas [120]. Different Fe oxides were tested for their potential to remove As by adsorption, with amorphous Fe oxides as the most effective due to the high specific surface area [121, 122]. High phosphate concentrations can reduce the sorption capacity of Fe oxides because phosphate competes for

adsorption sites with As on hydrous ferric oxides and inhibits therefore As adsorption [106]. However, a study with ferrihydrite colloids derived from a soil column experiment revealed the strong binding of As to ferrihydrite surfaces via inner-sphere complexes which was not impeded by the presence of phosphate and polymerized silica [123].

Magnetite nanoparticles coated with SiO<sub>2</sub> [124] or organic molecules [125] or goethite [106] were shown to be highly efficient for metal ion removal (e.g. Cu<sup>2+</sup>, Hg<sup>2+</sup>, Pb<sup>2+</sup>). Aggregation of Fe oxide nanoparticles decrease the sorption capacity of Cu<sup>2+</sup> again [126], proving the high efficiency of nanoparticulate Fe oxides for metal ion removal. Those “assisted natural remediation” treatments decrease metal concentrations in soil leachates and soil water and reduce microbial toxicity [106]. Therefore, highly reactive barriers could be easily implemented by using Fe oxide nanoparticles as these are mobile when injected as stable suspensions.

Several Fe-based remediation technologies are still at an experimental or pilot stage and there is a need to verify their effective application in the large-scale field [106]. Widespread applied PRB systems revealed limitations, which include installation methods and the precipitation of minerals derived from reactions with groundwater over time and therefore the significant loss of porosity and permeability within the PRB system [106].

Alternatively, we propose a new *in-situ* remediation technology for aquifers contaminated with aromatic hydrocarbons. Direct stimulation of microbial Fe reduction seems feasible by injecting Fe oxide colloids into the plume. The fast microbial reduction of the Fe oxide colloids with contaminants as electron donor makes the development of a cost-effective remediation technology possible.

## 1.7 Objectives of this thesis

This thesis focuses on the different factors influencing biotic and abiotic reactivity of ferrihydrite. The thesis research is part of the research unit FOR 580 “Electron Transfer Processes in Anoxic Aquifers”, funded by the German Research Foundation (DFG). The project investigates different electron transfer mechanisms between microbe-mineral interfaces.

In geomicrobiological studies the ferrozine and phenanthroline photometric assays are commonly applied for the determination of Fe(II) and total Fe. Therefore, the starting point of this thesis is the reevaluation of both assays under different conditions and with respect to various Fe oxides. The effects of different disintegration procedures and the microbial medium composition are shown in the chapters 3.1 and 4.1.



Chapters 3.2 and 4.2 are dealing with the impact of low molecular weight organic acids on the aggregation behavior of ferrihydrite and how it influences microbial reduction kinetics.

In the chapters 3.3 and 4.3 the biotic and abiotic reactivities of several synthetic ferrihydrites are compared as a function of aggregation state, specific surface area, and adsorbed ions. The aim is to get more insights into mineralogical factors influencing the reactivity of ferrihydrite.

The aim of this thesis is to gain further insights into the role of (i) mineralogical properties of ferrihydrite and (ii) organic acids on microbial Fe oxide reduction. A deeper understanding of limiting factors regarding Fe oxide reactivity is necessary for estimations about microbial turnover rates in soils and aquifers. This is of importance especially in anoxic aquifers at contaminated sites where Fe reduction is coupled to oxidation of these organic substances as a major respiratory process. This is helpful for both the assessment of the natural remediation potential of a contaminated site and the optimization of Fe-based remediation technologies.

## 2 Materials and Methods

All experiments, Fe oxide preparations, measurements, and calculations described below were conducted by the PhD candidate unless otherwise stated.

### 2.1 Cultivation of microorganisms

*Geobacter sulfurreducens* DSMZ 12127 [127] was obtained from the German Collection of Microorganisms and Cell Cultures (DSMZ, Germany). This strain, as well as a yet undefined, Fe-reducing enrichment culture (for the production of a goethite-magnetite mixture), were cultivated in two-fold diluted, modified freshwater medium modified after Widdel and Bak [128] and Widdel and Hansen [129], containing  $0.5 \text{ g L}^{-1}$  NaCl,  $0.2 \text{ g L}^{-1}$   $\text{MgCl}_2 \cdot 6\text{H}_2\text{O}$ ,  $0.1 \text{ g L}^{-1}$   $\text{KH}_2\text{PO}_4$ ,  $0.125 \text{ g L}^{-1}$   $\text{NH}_4\text{Cl}$ ,  $0.25 \text{ g L}^{-1}$  KCl,  $0.075 \text{ g L}^{-1}$   $\text{CaCl}_2 \cdot 2\text{H}_2\text{O}$ , and  $0.71 \text{ mg L}^{-1}$   $\text{Na}_2\text{SO}_4$ . The pH was adjusted to 6.5 – 6.9. This medium was supplemented with  $0.1 \text{ mL L}^{-1}$  trace elements solution SL10 [130],  $0.1 \text{ mL L}^{-1}$  selenite-tungsten solution,  $0.03 \text{ mL L}^{-1}$  of 7 vitamins solution [131], and  $5 \text{ }\mu\text{M}$  anthraquinone-2,6-disulfonate (AQDS). As stimulating agent for anaerobic growth, cAMP was added at  $10 \text{ }\mu\text{M}$ . Fifty  $\text{mmol L}^{-1}$  synthesized ferrihydrite [132] was used as electron acceptor. Electron sources and pH buffer systems were different for individual problems of the thesis (Tab. 2.1).

**Tab. 2.1:** Differing medium additives used in projects of this thesis.

	Reevaluation of colorimetric Fe determination methods	Influence of low molecular weight organic acids on microbial Fe oxide reduction	Reduced biotic and abiotic reactivity of ferrihydrite
Electron source	10 mM sodium acetate or 500 $\mu$ M toluene	5 mM sodium acetate	5 mM sodium acetate
pH buffer	Marble pearls [133]	10 mM NaHCO <sub>3</sub>	10 mM NaHCO <sub>3</sub>
Electron acceptors in precultures		50 mM ferric citrate (technical grade)	50 mM sodium fumarate

Microorganisms were cultivated in 60 mL medium in 100 mL glass serum bottles sealed with butyl rubber stoppers and flushed with 20/80% CO<sub>2</sub>/N<sub>2</sub>. The adsorber resin XAD-7 (0.3 g) was added to each toluene-containing bottle to decrease the actual toluene concentration to sub-toxic levels. The bottles were incubated at 30 °C in the dark. Addition of toluene, inoculation of the media with bacteria, and sampling were performed carefully with anoxic syringes through the closed stoppers. If not otherwise stated, all chemicals (Sigma-Aldrich, Germany) were analytical grade quality.

## 2.2 Preparation of cell suspensions

An anoxic low-salt medium was used for the batch cell suspension experiment. The cultivation medium described above was modified to 10 mg L<sup>-1</sup> NaCl, 0.4 mg L<sup>-1</sup> MgCl<sub>2</sub> · 6H<sub>2</sub>O, 2.5 mg L<sup>-1</sup> NH<sub>4</sub>Cl, 5 mg L<sup>-1</sup> KCl, and 0.15 mg L<sup>-1</sup> CaCl<sub>2</sub> · 2H<sub>2</sub>O. The medium was buffered with 10 mM Tris-HCl (pH 6.8) instead of NaHCO<sub>3</sub>. All other ingredients remained unchanged.

After growth to the late exponential phase, the preculture (1 L and 3 L for sodium fumarate- and ferric citrate-containing medium, respectively) was harvested by centrifugation for 20 min at 11,328 x g and at 20 °C (Avanti J-E centrifuge with JA-10 rotor; Beckman-Coulter, California). The cell pellet was resuspended in 50 mL fresh acetate-free low-salt medium in an anoxic glove box (O<sub>2</sub> < 3 ppm, N<sub>2</sub>/H<sub>2</sub> = 95/5 %, v/v, Coy Laboratory Products, USA). To remove residual electron donors and acceptors from the cell suspensions, centrifugation and resuspension was repeated once. The cell suspension was immediately added to the reduction experiments in a 1:10 ratio and yielded final cell densities of 2.2 x 10<sup>9</sup> and 2.7 x 10<sup>10</sup> cells L<sup>-1</sup> in chapter 3.2 and 3.3, respectively.

For the normalization of reduction rates, flow cytometry was applied to measure cell numbers of the cell suspension for each individual experiment using a Cytomics FC 500 cell analyzer

(Beckman-Coulter, USA). Paraformaldehyde-fixed cells from the cell suspension were stained by SYBR green I nucleic acid stain (Molecular Probes, Eugene, OR), diluted in 0.22- $\mu\text{m}$ -filtered Dulbecco's phosphate-buffered saline, and counted at a wavelength of 510 nm in Trucount bead (Becton Dickson) calibrated measurements.

## 2.3 Fe bearing solutions and minerals

### 2.3.1 *Fe oxides and solutions prepared for the reevaluation of colorimetric Fe determination methods commonly used in geomicrobiology*

As reference solutions for the evaluation of crystalline Fe oxide dissolution, 9 mM Fe(II) and Fe(III) solutions were prepared with  $\text{FeSO}_4 \cdot 7 \text{H}_2\text{O}$  (A.C.S. grade, Sigma-Aldrich, Inc., USA) and  $\text{Fe}(\text{NO}_3)_3 \cdot 9 \text{H}_2\text{O}$  (A.C.S. grade, Sigma-Aldrich) in 1 M HCl, respectively. Additionally, both solutions were mixed at the ratio 1:40 (v/v) to mimic potentially reduced or oxidized minerals. Macroaggregate 2-line ferrihydrite was synthesized according to the protocol of Lovley and Phillips [132]. Five hundred millilitres of a 0.4 M  $\text{FeCl}_3 \cdot 6\text{H}_2\text{O}$  solution (reagent grade, Sigma-Aldrich, Germany) were titrated to a pH of 7.0 with 1 M NaOH (p.a., A.C.S. reagent, Sigma-Aldrich). After precipitation of ferrihydrite, the supernatant was discarded. To remove remaining ions from the preparation the precipitate was washed with MilliQ water ( $R=18.2 \text{ M}\Omega$ , 4 ppb TOC, MilliporeElix + Milli-Q Advantage 10A, USA) for at least 5 times, until the supernatant remained turbid. Fifty-one  $\text{mmol L}^{-1}$  synthesized ferrihydrite was dissolved in 1 M and 6 M HCl (1:10, v/v). Magnetite and a mixture of goethite and magnetite, formed during a batch experiment by anaerobic microbial reduction of synthetic ferrihydrite, were also dissolved in 1 M and 6 M HCl (1:10, v/v) with final  $\text{Fe}(\text{tot})$  concentrations of 31 and 36  $\text{mmol L}^{-1}$ , respectively. Solid synthetic goethite (Bayferrox 920Z, Lanxess GmbH, Germany) was dissolved in 1 M and 6 M HCl with final concentrations of 10  $\text{mmol L}^{-1}$ , whereas pyrite (Georg Maisch, Freising, Germany) was dissolved only in 6 M HCl (1:10, v/v) with a final concentration of 35  $\text{mmol L}^{-1}$ .

### 2.3.2 *Ferrihydrite used for the influence of low molecular weight organic acids on microbial Fe oxide reduction*

Macroaggregate 2-line ferrihydrite was synthesized as described in chapter 2.3.1 [132]. Possible recrystallization of ferrihydrite in the presence of citrate was tested by adding 24 mL of  $\text{Na}_3\text{-citrate}$  (0.05 M, puriss., Riedel-de Haën, Germany) to 30 mL of macroaggregate 2-line ferrihydrite (0.25  $\text{mol L}^{-1}$ ). The suspension was shaken in the dark at 30 °C for seven days. To separate the ferrihydrite from the supernatant, the sample was centrifuged for 20 min with 2,890 x g at 4 °C

(Heraeus Megafuge 1.0R, Thermo Scientific, USA). The ferrihydrite was washed three times by resuspending in MilliQ water and centrifugation as described above.

All Fe oxides were stored at 4 °C in the dark. Autoclaving was omitted to avoid changes in crystal structures.

To investigate the effect of humic acids on colloidal ferrihydrite stability, natural aquatic humic acids extracted from the deep borehole Gohy-573 in the Gorleben aquifer (Lower Saxony, Germany) were used [45]. A stock solution was prepared by adding 1 g Gohy humic acids to 1 L MilliQ water. The pH of the solution was adjusted to 7.0 with 1 M NaOH and continuously stirred over night. The humic acid solution was filtered through a 0.22 µm filter to a previously autoclaved glass bottle, sealed with a butyl rubber stopper, flushed with 20/80% CO<sub>2</sub>/N<sub>2</sub>, and stored at 4 °C in the dark until further use.

### 2.3.3 *Ferrihydrites used for the reduced biotic and abiotic reactivity of ferrihydrite nanoparticles below a critical aggregate size*

Five different ferrihydrites, three 2-line (2LFh 1-3) and two 6-line (6LFh 1,2), were synthesized according to protocols described in the literature. 2LFh 1 [134], was prepared by adjusting the pH of 0.5 L of a 0.1 M solution of Fe(NO<sub>3</sub>)<sub>3</sub> · 9H<sub>2</sub>O (A.C.S. grade, Sigma-Aldrich, Inc., USA) with 0.1 M KOH under constant stirring to pH 7-8. The solution was centrifuged (4 °C, 11,328 x g, 30 min) and the pellet obtained was resuspended in MilliQ water (R=18.2 MΩ, 4 ppb TOC, MilliporeElix + Milli-Q Advantage 10A, USA) and washed repeatedly.

Another 2-line ferrihydrite [135], referred to as 2LFh 2, was obtained by grinding 20.25 g of Fe(NO<sub>3</sub>)<sub>3</sub> · 9H<sub>2</sub>O (A.C.S. grade, Sigma-Aldrich) and 11.91 g of NH<sub>4</sub>CO<sub>3</sub> (pure food grade, AppliChem GmbH, Germany) for roughly 15 min using mortar and pestle until bubbling ceased. The resulting slurry was dried at 100 °C for 24 h. The precipitate was resuspended in MilliQ water, centrifuged, and washed repeatedly as described above. After the last washing step the pellet was resuspended in 0.5 L MilliQ water.

A third 2-line ferrihydrite, referred to as 2LFh 3, was produced using the protocol for 2-line ferrihydrite of Cornell and Schwertmann [136]. 1 M FeCl<sub>3</sub> · 6H<sub>2</sub>O (reagent grade, Sigma-Aldrich) solution was dropwise titrated with 1 M KOH (p.a., Merck KGaA, Germany) under continuous stirring until pH 7-8 was reached. The suspension was centrifuged and washed as described above.

A 6-line ferrihydrite, referred to as 6LFh 1 [132], was prepared as described in chapter 2.3.1.

A second 6-line ferrihydrite, referred to as 6LFh 2, was prepared after the protocol of Anschutz and Penn [137]. 20 g of Fe(NO<sub>3</sub>)<sub>3</sub> · 9H<sub>2</sub>O (A.C.S. grade, Sigma-Aldrich) were added to MilliQ water, preheated to 75 °C. The temperature was kept constant under continuous stirring. After 12

min the solution was plunged into an ice bath until the temperature reached  $\sim 20$  °C. The cooled suspension was dialyzed (ZelluTrans, MWCO=6,000-8,000 Da, regenerated cellulose, Carl Roth GmbH + Co. KG, Germany) against MilliQ water until the conductivity of the surrounding water column remained constant ( $\sim 1.7 \mu\text{S cm}^{-1}$ ) over 24 h.

All Fe oxides were stored anoxically at 4 °C in the dark in glass bottles until further use, but for less than three months.

## 2.4 Characterization of Fe oxides and organic substances

X-ray diffraction (XRD), analysis of the specific surface area, Fourier-transform infrared (FTIR), X-ray photoelectron spectroscopy measurements (XPS), and Mössbauer spectroscopy were performed with dialyzed (ZelluTrans, MWCO=6,000-8,000 Da, regenerated cellulose, Carl Roth GmbH + Co KG, Germany) and freeze-dried (Sentry 8L, Virtis, USA) aliquots of the Fe oxides. XRD diffractograms were obtained using a Philips PW 1050 diffractometer (Philips, Eindhoven, The Netherlands) equipped with a diffracted-beam graphite monochromator and a Bruker AXS microdiffractometer equipped with a General Area Detection Diffraction System (GADDS) detector.  $\text{CoK}\alpha$  X-ray radiation was applied. Random powder specimens were measured from  $10^\circ$  to  $80^\circ 2\theta$  in steps of  $0.02^\circ 2\theta$ , with a counting time of 5 s for each increment. Analysis of the data was conducted using the diffraction file data book of the International Centre for Diffraction Data [138] and the American Mineralogist Crystal Structure Database [139]. Measurements and analysis were done by Dr. Katja Heister.

FTIR spectra were recorded by Matthias Händel using a Nicolet iS 10 spectrometer (Thermo Fisher Scientific, Dreieich, Germany) to study the mineral and organic composition. Mortared samples were mixed with KBr (Alfa Aesar, FTIR grade) at a ratio of 1:200 and pressed to pellets. The pellets were studied in transmission mode in the mid-infrared range between 4000 and  $400 \text{ cm}^{-1}$  with 16 scans per spectrum and a resolution of  $4 \text{ cm}^{-1}$ . Evaluation of the data was done by the PhD candidate together with Matthias Händel.

Iron speciation and magnetic properties were analyzed by  $^{57}\text{Fe}$  Mössbauer spectroscopy in transmission geometry by Dr. Christian Schröder. The measurement was performed with a  $^{57}\text{Co}$  source in Rh matrix at room temperature, 77 K, and  $\sim 5$  K. The source remained always at room temperature. The spectrometer was constructed by WissEL (Wissenschaftliche Elektronik GmbH, Starnberg, Germany). A Janis closed-cycle cryostat with a helium atmosphere was used to vary the temperature of the sample. Spectra were evaluated with the Recoil software using the Voigt-based fitting method. Spectra were calibrated against an  $\alpha$ -Fe foil at room temperature, and

values of the isomer and center shift are quoted relative to  $\alpha$ -Fe at room temperature. Interpretation of the obtained spectra was done by Dr. Christian Schröder.

The XPS spectra were recorded and interpreted by Dr. Paul L. Wincott and Prof. Jonathan R. Lloyd. A Kratos Axis Ultra spectrometer was used, employing a monochromated Al K $\alpha$  X-ray source and an analyzer pass energy of 80 eV for survey scans and 20 eV for elemental scans, resulting in a total energy resolution of ca. 1.2-1.4 eV or 0.6-0.7 eV, respectively. Uniform charge neutralization of the photoemitting surface was achieved by exposing the surface to low energy electrons in a magnetic immersion lens system (Kratos Ltd.). The system pressure was  $1 \times 10^{-9}$  mBar. Spectra were analyzed by first subtracting a Shirley background and then obtaining accurate peak positions by fitting peaks using a mixed Gaussian/Lorentzian (30/70) line shape. Quantification of surface atom percentage was achieved using a derived analyzer transmission function and Scofield theoretical elemental cross-sections. During fitting, spin orbit split components were constrained to have identical line width, elemental spin orbit energy separations and theoretical spin orbital area ratios. All photoelectron binding energies (BE) are referenced to C1s peaks set at 285 eV BE. The analyzer was calibrated using elemental references; Au4f $_{7/2}$  (83.98 eV BE), Ag3d $_{5/2}$  (368.26 eV BE) and Cu2p $_{3/2}$  (932.67 eV BE).

Scanning electron microscopy (SEM) images were recorded by Gabriele Mettenleiter using JSM-6300F scanning electron microscope (Jeol), equipped with a field emission electron gun operated at 5 kV. Ferrihydrite samples were diluted to a final concentration of 5 mmol L $^{-1}$  and air-dried on the sample holder. To reduce or avoid charging under electron impact, the samples were covered with a thin layer of platinum, sputter deposited prior to SEM analysis.

The specific surface area and micropore surface area of the freeze-dried sample material was determined by Dr. Katja Heister using N $_2$  physisorption at 77.35 K. The calculations were performed from 11-point isotherms according to the Brunauer-Emmett-Teller (BET) equation [140]. A Quantachrome Autosorb 1 analyzer (Syosset, NY) was used to perform the analysis. Prior to measurement, sample material was degassed under vacuum at 30 to 35 °C overnight. This mild treatment was chosen in order to prevent structural changes in the dried Fe oxides due to heating. All samples were measured two times with a reproducible standard deviation of less than 1% of the obtained specific surface area. An Al $_2$ O $_3$  bead standard with a specific surface area of  $79.8 \pm 0.4$  m $^2$  g $^{-1}$  (BAM, Germany) was applied for external calibration. All measured values of the standard fell within a 95% confidence interval.

The surface area of micropores, i.e. pores with an average width <2 nm, was assessed by the t-method of de Boer et al. [141].

Dynamic light scattering (DLS) was applied by the PhD candidate to measure hydrodynamic diameters ( $d_{ij}$ ) of the ferrihydrite samples, using a ZetaSizer Nano ZS (Malvern Instruments,

Worcestershire, United Kingdom), equipped with an He-Ne laser at 633 nm. Low-volume folded capillary sizing cuvettes were used to measure diluted ferrihydrite samples ( $5 \text{ mmol L}^{-1}$ ). Two measurements with 10 runs each were conducted per sample. The collection time per run was 10 s. The mean polydispersity index as a measure for the size distribution of the sample, was 0.723 ( $\pm 0.231$ ;  $n=6$ ), 0.242 ( $\pm 0.096$ ;  $n=9$ ), and 0.233 ( $\pm 0.051$ ;  $n=9$ ) for unfiltered, 0.45  $\mu\text{m}$ -filtered, and 0.22  $\mu\text{m}$ -filtered samples of citrate-incubated ferrihydrite (chapter 3.2) and 0.228 ( $\pm 0.142$ ;  $n=5$ ) for five different ferrihydrite preparations (chapter 3.3).

The concentration of citrate was analyzed in aqueous samples using a Shimadzu LC-10A series HPLC system (Shimadzu, Japan) equipped with an Aminex HPX-87H analytical column (300 x 7.8 mm; Bio-Rad, USA) at 50 °C. Samples were analyzed by an isocratic method (5 mM  $\text{H}_2\text{SO}_4$ ) at a flow rate of 0.5 mL  $\text{h}^{-1}$ . Retention time was 15.2 min and total run time was 20 min. Analytes were detected by UV absorbance at 220 nm. Samples were prepared by adding 55  $\mu\text{L}$  of 35% perchloric acid to 0.5 mL of sample and incubated for 10 min on ice. Subsequently, 27  $\mu\text{L}$  of 7 M KOH was added and stored at -20 °C. Before measurements, the samples were thawed at room temperature, and centrifuged at 11,330 x g for 2 minutes (Centrifuge MiniSpin®plus, Eppendorf AG, Germany). The measurements were done by Sviatlana Marozava together with the PhD candidate. Evaluation and interpretation was done by the PhD candidate.

The concentration of dissolved organic carbon of the Gohy humic acid stock solution was measured with a total organic carbon analyzer TOC-5000A (Shimadzu, Kyoto, Japan) after internal acidification of the samples with 2 M HCl.

As external control of the quality of the ferrozine and phenanthroline assays and the dissolution procedures, the total Fe content of all samples was measured with inductively coupled plasma atomic emission spectrometry (ICP-AES) by Prof. Bernhard Michalke. Minerals were totally dissolved using *aqua regia* (mixture of HCl :  $\text{HNO}_3 = 3 : 1$ ) with heating at 70 °C for 1 h. Total Fe concentrations in the digestions were determined using an Ciros Vision ICP-AES (Spectro Analytical Instruments, Germany) in 15 L  $\text{min}^{-1}$  Ar. The PhD candidate interpreted the obtained data.

## 2.5 Reagents

### 2.5.1 Ferrozine assay

The ferrozine stock solution was prepared by dissolving 1 g of ferrozine (purum p.a., Fluka Sigma-Aldrich) in 1 L of a 6.5 M ammonium acetate solution (97%+, A.C.S., Sigma-Aldrich). A



1.4 M hydroxylamine stock solution (99%, Sigma-Aldrich) was prepared in 1 L of 1 M HCl. Both solutions were stored at 4 °C in the dark.

### 2.5.2 *Phenanthroline assay*

A 7 mM phenanthroline stock solution ( $\geq 99\%$ , Sigma-Aldrich) was prepared. If Fe(III) has been reduced to Fe(II) for determination of the total Fe content, a 1.2 M sodium acetate solution (99%, ReagentPlus®, Sigma-Aldrich) was used as buffer. When the sample contained Fe(III), a 1.3 M ammonium acetate solution was used instead. Furthermore, a 2 M ammonium fluoride solution (99.99+% trace metals basis, Sigma-Aldrich) was used as masking agent for Fe(III).

If not otherwise stated, all reagents were prepared with Millipore water ( $R = 18.2 \text{ M}\Omega$ , 4 ppb TOC, MilliporeElix + Milli-Q Advantage 10A, USA).

## 2.6 **Experimental procedures for the reevaluation of colorimetric Fe determination methods commonly used in geomicrobiology**

### 2.6.1 *Influence of acid concentration on Fe extraction*

Dissolved Fe(II) and Fe(III) (9 to 10 mM Fe(tot)) and solutions containing goethite (31 mmol L<sup>-1</sup>), a mixture of goethite and magnetite (36 mmol L<sup>-1</sup>), magnetite (31 mmol L<sup>-1</sup>), and ferrihydrite (51 mmol L<sup>-1</sup>) were diluted in 1 M or 6 M HCl in an Eppendorf tube (1:9, v/v in 1 mL) and shaken over night or for 4 days (goethite) at 21 °C. In parallel, all samples diluted in 6 M HCl were shaken at 60 °C over night or for 4 days (goethite and pyrite). One sample of each approach was taken and three aliquots per sample were measured with ferrozine or phenanthroline.

For the measurement with ferrozine, the acidified and shaken samples were mixed with the ferrozine solution at a ratio of 1:9 (v/v in 0.2 mL) in a microtiter plate (0.3 mL/well, Nunc, Denmark), enabling a faster measurement procedure for large sample numbers as compared to the use of cuvettes. Absorbance of three wells per sample was measured with a Wallac Victor<sup>3</sup> 1420 plate reader (PerkinElmer, Inc., USA) at 560 nm.

For the phenanthroline method, 0.16 mL of ammonium fluoride, 0.2 mL of phenanthroline, and 0.4 mL of ammonium acetate were filled in 2 mL reaction tubes (Eppendorf, Germany). The acidified Fe samples were added in 10  $\mu\text{L}$  steps to the mixture, until an appropriate orange color developed ( $> 0.2$  absorbance units). After 1 h incubation, three aliquots of 0.2 mL from each sample were filled into microtiter plates and absorbance was measured at 490 nm. For both methods, Fe concentrations and standard deviations were calculated from the mean value of the absorbance of three aliquots.

For determination of total Fe content with the phenanthroline method, the acidified samples were diluted and reduced with hydroxylamine (1:10, v/v in 1 mL) and shaken for 15 min at 21 °C to reduce all Fe(III) to Fe(II). Afterwards, the samples were diluted with ferrozine and measured as described above. For the phenanthroline procedure, 0.2 mL of phenanthroline and 0.4 mL of sodium acetate were mixed in a 2 mL tube and the acidified and reduced samples were added in 10 µL steps as described above. After 1 h incubation, the absorbance was measured. Masking of Fe(III) with ammonium fluoride was not necessary due to the prior reduction with hydroxylamine.

### 2.6.2 *Anoxic preparation of samples*

To investigate the impact of ambient oxygen during the procedure, the same experiments were also conducted under anoxic conditions in a glove box (< 3 ppm O<sub>2</sub>, N<sub>2</sub>/H<sub>2</sub> = 95/5%, v/v, Coy Laboratory Products, USA). One sample of each approach was prepared in 6 M HCl and shaken over night at 60 °C. Three aliquots per sample were analyzed as described above. All chemicals were filled into anoxic 100 mL glass serum bottles, sealed with butyl rubber stoppers and flushed with 20/80% CO<sub>2</sub>/N<sub>2</sub> for 3 min to exchange the headspace before introducing into the glove box.

### 2.6.3 *Growth experiments*

For evaluation of the performance of the different methods, *G. sulfurreducens* was grown in a freshwater medium as described above. Cells and ferrihydrite were added via anoxic syringes to a final concentration of 52 mmol L<sup>-1</sup>. The bottles were incubated at 30 °C in the dark. Immediately after inoculation, the first samples for Fe determination were taken under anoxic conditions and dissolved in 1 M and 6 M HCl as described above. Subsequently, the undiluted samples were transferred out of the glove box, exposed to O<sub>2</sub>, and dissolved in oxic 1 M or 6 M HCl, respectively. All samples dissolved in 1 M HCl and one reaction tube with samples in 6 M HCl were shaken over night at 21 °C. The remaining reaction tubes with samples diluted in 6 M HCl were shaken over night at 60 °C. The procedure of sampling remained unchanged over the entire experiment. Three aliquots of each sample were measured with the ferrozine and phenanthroline method as described above. Iron concentrations and standard deviations were calculated from the mean value of the absorbance of three aliquots.

Total Fe was determined with both methods for all time points, and mean values and standard deviations (n=11) are calculated in percent of the concentration measured with ICP-AES. Ferrous and total Fe were measured for all three batches separately. Data of one batch are shown, whereas the other two batches serve as independent replicates.

#### 2.6.4 Influence of medium composition

Ferric Fe solutions were prepared with  $\text{FeCl}_2 \cdot 4\text{H}_2\text{O}$  (p.a., Sigma-Aldrich) in different concentrations (Tab. 2.2). Every solution was mixed with a single medium additive. In order to visualize potential effects of additives, their added concentrations are increased. One part of the samples was flushed with  $\text{N}_2/\text{CO}_2$  (20/80%) (Tab. 2.2). All samples were dissolved in 1 M HCl with subsequent shaking over night at 21 °C. Ferrous and total Fe determinations were performed as described above under oxic conditions. All approaches were done twice to obtain independent replicas.

**Tab. 2.2:** Composition of  $\text{FeCl}_2$  solutions including different medium additives for the investigation of their interferences with ferrozine and phenanthroline.

	Fe(II)	$\text{CO}_2/\text{N}_2$	Medium	Medium+ $\text{CO}_2/\text{N}_2$	Acetate	Acetate + $\text{CO}_2/\text{N}_2$	TE	7 Vits
Vol% of additive in sample	-	-	90	90	1.5	1.5	1.0	25
Total Fe concentration <sup>1</sup>	4.4	4.4	5.5	5.5	4.5	4.5	10.6	7.5
pH <sup>2</sup>	1.2	1.2	1.2	1.2	1.2	1.2	1.0	1.0

<sup>1</sup> determined with ICP-AES

<sup>2</sup> determined after acidification of the samples with 1 M HCl and adjustment to 1.0 – 1.2 with 1 M NaOH

#### 2.6.5 Influence of light on ferrous Fe determination with ferrozine

To investigate the photochemical reduction of Fe(III)-ferrozine complexes, two aqueous Fe(III) samples with final concentrations of 1.4 or 0.7 mM were incubated for 0, 3, 5, 7, 10, or 30 min under ambient light irradiation, respectively. Three aliquots per sample were measured for ferrous Fe production. Iron concentrations and standard deviations were calculated from the mean absorbance values.

#### 2.6.6 Statistical analysis

Normal distribution of all data sets was tested with the Kolmogorov-Smirnov test. The Student's *t* test at 5% significance level [142] was used to compare the Fe concentrations obtained with ferrozine and phenanthroline, respectively. All statistical analyses were performed using SPSS Statistics 18 (IBM, Armonk, USA) and Microsoft Office Excel 2003.

## 2.7 Experimental procedures for the influence of low molecular weight organic acids on microbial Fe oxide reduction

### 2.7.1 *Microbial reduction experiments*

Experiments were performed in 60-mL medium batch incubations, initiated in 100-mL glass serum bottles sealed with butyl rubber stoppers and flushed with 20/80% CO<sub>2</sub>/N<sub>2</sub>. The Fe oxide aggregates, sodium citrate solution (50 mM), and the bacterial cell suspension were added to the medium via anoxic syringes at specific amounts to obtain comparable initial ferric Fe (4.2 mmol L<sup>-1</sup>) and citrate (0.0 – 2.4 mM) concentrations, resulting in molar citrate/Fe ratios (citr/Fe) of 0.0-0.58. Ferrihydrite was incubated with medium and the respective citrate concentrations for 12 h prior to inoculation. Abiotic controls were performed by adding the cell suspension through a 0.22- $\mu$ m filter (Millex-GP, Merck Millipore, USA), thereby retaining the microorganisms. Immediately after inoculation, the first samples for Fe<sup>2+</sup> analysis were withdrawn. Then, the experimental bottles were incubated at 30 °C in the dark and shaken at 300 rpm.

### 2.7.2 *Abiotic dissolution experiments*

To study the dissolution kinetics of ferrihydrite in the presence of citrate I used the same anoxic low-salt medium as for the microbial reduction experiments (ionic strength ~ 10 mM, EC ~680  $\mu$ S cm<sup>-1</sup>, pH 6.5). Experiments were done in triplicates and were performed in 60-mL medium batch incubations, in 100-mL glass serum bottles sealed with butyl rubber stoppers and flushed with 20/80% CO<sub>2</sub>/N<sub>2</sub>. The Fe oxide aggregates, sodium citrate solution (50 mM), and GoHy humic acids (HA) (1 g L<sup>-1</sup>) [45] were added to the medium via anoxic syringes to obtain comparable initial ferric Fe (2.8 - 3.3 mmol L<sup>-1</sup>), citrate (0.0 – 2.4 mM), and humic acid (2 – 60 mg L<sup>-1</sup>) concentrations. Molar citr/Fe ratios and organic carbon:Fe (OC/Fe) ratios were 0.0-0.5 and 0.0-0.9, respectively. To keep the maximum volume at 90 mL higher OC/Fe ratios were avoided. A positive control contained 4.7 mM citrate and 2.8 mmol L<sup>-1</sup> ferric Fe (citr/Fe = 1.7) to ensure complete dissolution of the ferrihydrite aggregates. Immediately after addition of citrate or HA, the first samples for total Fe (Fe(tot)) analysis were withdrawn and centrifuged (9,660 x g, 2 min, 20 °C, Centrifuge MiniSpin®plus, Eppendorf AG, Germany). Dissolved Fe was measured as total Fe in the supernatant. Then, the experimental bottles were shaken at 300 rpm at 30 °C in the dark to avoid photo-induced reduction.

After dissolution equilibrium was reached, samples were 0.22 and 0.45  $\mu$ m-filtered (Millex-GP, Merck Millipore Corp., USA) for determination of hydrodynamic diameters. For mineralogical analysis, samples were centrifuged for 20 min at 4 °C with 2,890 x g (Heraeus Megafuge 1.0R, Thermo Scientific, USA) and washed three times with MilliQ water. The supernatants were

dialyzed (MWCO = 6,000-8,000 Da, regenerated cellulose, Carl Roth GmbH + Co. KG, Germany) against MilliQ water until the electric conductivity of the surrounding water column remained constant ( $\sim 3 \mu\text{S cm}^{-1}$ ).

### 2.7.3 Fe analysis

Iron was measured using the ferrozine assay [143, 144]. Aliquots of 0.2 mL were withdrawn from the experiment, diluted 1:4 in 1 M HCl, and measured as described above. Absorbance of all samples was measured in triplicates.

### 2.7.4 Calculation of dissolution and reduction kinetics

Based on measured data of citrate-mediated dissolution of ferrihydrite and microbial ferrihydrite reduction in the presence of citrate, rate laws were applied to calculate the different kinetics.

Kinetic rate laws for the citrate-induced dissolution of ferrihydrite were formulated to allow a quantitative description of the dissolution experiments. Several types of mathematical expressions are available [134]. Since dissolution kinetics of ferrihydrite during the first 50 h are not linear, a parabolic rate law had to be applied:

$$\alpha^2 = kt \quad (\text{eq. 2.1})$$

Here,  $\alpha$  is the dissolved fraction at a certain time point  $t$  and  $k$  is the rate constant. The parabolic model meets its limitations at molar citr/Fe ratios  $\geq 0.2$ . Therefore, the model for the dissolution of spherical particles via three-dimensional diffusion was selected as the most suitable:

$$\left[1 - \left(1 - \alpha^{1/3}\right)\right]^2 = kt \quad (\text{eq. 2.2})$$

The simultaneous proceeding of both processes requires the combination of equations 1 and 2:

$$\alpha = m\sqrt{k_1 t} + n\left(\sqrt{k_2 t}\right)^3 \quad (\text{eq. 2.3})$$

With  $k_1$  and  $k_2$  being the rate constants for the parabolic and spherical dissolution rate law at a certain time point  $t$ , respectively. The variables  $m$  and  $n$  are weighting parameters, in dependence of citrate concentration with  $n+m=1$ .

The comparison of the weighted rate constants  $mk_1+nk_2$  with the respective citrate concentration revealed a sigmoid correlation (Fig. 3.9B):

$$mk_1 + nk_2 = \frac{a}{1 + \left(\frac{b}{[citr]}\right)^c} \quad (\text{eq. 2.4})$$

With  $[citr]$  being the citrate concentration [mM] and  $a, b, c$  being variables.

The relationship between microbial initial reduction rates and citrate concentrations can be described with a Michaelis-Menten kinetic (Fig. 3.9C):

$$R = \frac{R_{\max}[citr]}{k_{red} + [citr]} + 0.0286 \quad (\text{eq. 2.5})$$

Here,  $R$  is the microbial initial reduction rate [mM h<sup>-1</sup>];  $R_{\max}$  the maximum reduction rate [mM h<sup>-1</sup>];  $k_{red}$  the rate constant of microbial reduction [h<sup>-1</sup>]; and 0.0286 is the reduction rate of ferrihydrite without citrate.

Based on the relationships between citrate concentrations with both abiotic dissolution and microbial reduction, microbial reduction kinetics were simulated. Before that, two important assumptions had been made: (i) a certain percentage of macroaggregate ferrihydrite can be reduced by *G. sulfurreducens* per time with a corresponding low rate and (ii) dissolved Fe is bioavailable. An initial dissolved Fe fraction was calculated, stemming from incubation of ferrihydrite with citrate for 12 h prior to inoculation with *G. sulfurreducens* and a microbial lag phase of 2 h.

Calculations were done with Microsoft Office Excel 2003 and parameters were fitted by hand.

## 2.8 Experimental procedures for the reduced biotic and abiotic reactivity of ferrihydrite nanoparticles below a critical aggregate size

### 2.8.1 Abiotic dissolution in 1 M HCl

For abiotic dissolution experiments, ferrihydrite samples were diluted to a total Fe concentration of ~10 mmol L<sup>-1</sup> with MilliQ water. Aliquots of 0.1 mL per sample were diluted in 0.9 mL 1 M HCl in an oxic Eppendorf tube. Subsequently, the samples were centrifuged (9,660 x g, 30 sec) and aliquots of 0.05 mL of the supernatant were diluted in 0.95 mL hydroxylamine-HCl for total Fe determination with ferrozine [143, 144]. I defined Fe which did not sediment during centrifugation as dissolved. After sampling, the Eppendorf tubes were vortexed and shaken at 300 rpm.

### 2.8.2 *Abiotic reduction with ascorbic acid*

Abiotic reduction experiments were performed in triplicates in 50-mL glass serum bottles, containing 30 mL of anoxic 10 mM ascorbic acid, sealed with butyl rubber stoppers and flushed with 20/80% CO<sub>2</sub>/N<sub>2</sub> (v/v). The specific Fe oxide aggregates were added via anoxic syringes at specific amounts to obtain comparable initial ferric Fe concentrations (~5 mmol L<sup>-1</sup>). Immediately after addition of Fe oxides, the first samples for Fe<sup>2+</sup> analysis were withdrawn. Subsequently, the samples were centrifuged at 9,660 x g (Centrifuge MiniSpin®plus, Eppendorf AG, Germany) for 30 sec at 21 °C. Aliquots of 0.1 mL were taken from the supernatant and stabilized against re-oxidation in 0.4 mL of 1 M HCl and immediately measured with ferrozine [143, 144]. The experimental bottles were shaken at 100 rpm at 21 °C.

### 2.8.3 *Microbial reduction experiments*

Experiments were performed in triplicates in 60-mL batch incubations, in 100-mL glass serum bottles, sealed with butyl rubber stoppers and flushed with 20/80% CO<sub>2</sub>/N<sub>2</sub> (v/v). The Fe oxides and the bacterial cell suspensions were added to the medium via anoxic syringes at specific amounts to obtain initial ferric Fe concentrations of ~5 mmol L<sup>-1</sup>. Abiotic controls were performed by adding the cell suspension through a 0.22-µm filter (Millex-GP, Merck Millipore Corp., USA), thereby retaining the bacteria. Immediately after inoculation, the first samples for Fe<sup>2+</sup> analysis were withdrawn. Then, the experimental bottles were incubated at 30 °C in the dark and shaken at 300 rpm.

### 3 Results

#### 3.1 Reevaluation of colorimetric Fe determination methods commonly used in geomicrobiology<sup>2</sup>

To compare the photometric ferrozine and phenanthroline assays for Fe determination, I measured the Fe(II) and Fe(tot) contents of Fe(II)<sub>aq</sub> and Fe(III)<sub>aq</sub>, mixed valence solutions, synthetic goethite, ferrihydrite, and pyrite, as well as microbially-formed magnetite, and a microbially-formed mixture of goethite and magnetite.

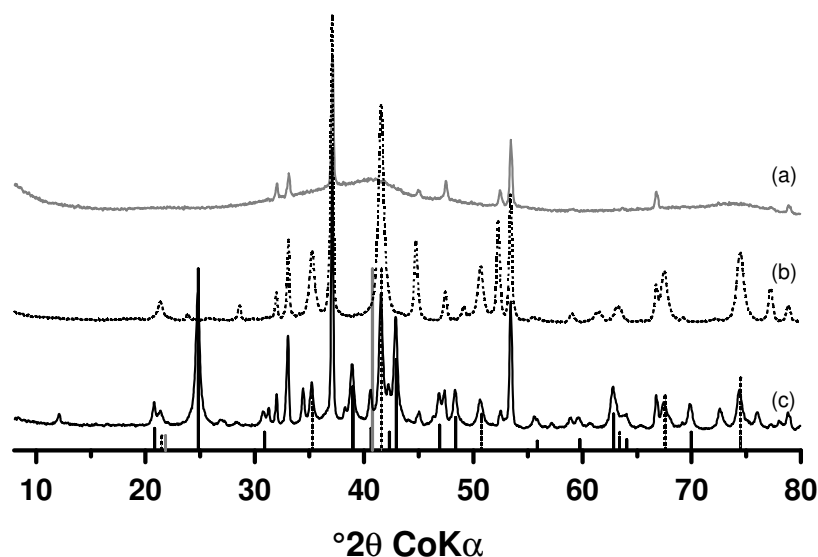


**Fig. 3.1:** X-ray diffraction patterns of Fe bearing minerals from anaerobic microbial reduction experiments: (a) ferrihydrite, (b) magnetite, and (c) mixture of goethite and magnetite. Bars show theoretical peaks of ferrihydrite (gray), magnetite (dotted), and goethite (black). Peaks of NaCl ( $32.04$ ,  $37.14$ ,  $53.42$ ,  $66.8^\circ 2\theta$ ) and KCl ( $33.12^\circ 2\theta$ ) originate from the cultivation medium, peak at  $45.02^\circ 2\theta$  from the aluminum sample holder.

<sup>2</sup> This chapter was published in *Journal of Microbiological Methods* 89 (2012) 41-48



The accuracy of each test for Fe(tot) was obtained by comparison with the *aqua regia* dissolved samples measured with ICP-AES.

The identity of synthesized ferrihydrite as well as the microbially-formed magnetite and the mixture of goethite and magnetite were confirmed by XRD analysis (Fig. 3.1).

### 3.1.1 Efficiency of total Fe determination

For Fe(II)<sub>aq</sub>, Fe(III)<sub>aq</sub>, ferrihydrite, and magnetite, the concentrations of Fe(tot) obtained from the phenanthroline assay after dissolution in 1 M HCl (at 21 °C) were significantly higher than those from the ferrozine method. For ferrihydrite and aqueous Fe(II) or Fe(III) standard solutions, the phenanthroline assay perfectly matched the concentrations of the external control measurements via ICP-AES (Fig. 3.2A), while the ferrozine assay led to systematic underestimation of Fe(tot) concentrations between 13 and 10%.

Due to the low solubility of goethite, microbially-formed magnetite, and the mixture of goethite and magnetite in 1 M HCl, the concentrations of these crystalline Fe forms were significantly underestimated with both assays by 78 to 92% for goethite and the mixture of goethite and magnetite and 5 to 12% for magnetite (Fig. 3.2A). In case of goethite and the mixture of goethite and magnetite, the minerals were visibly not dissolved completely, which led to additional disturbance of the photometric measurements by turbidity.

The Fe(tot) concentrations after dissolution in 6 M HCl at 21 °C for 4 days for goethite and pyrite were similarly low as concentrations obtained after shaking in 1 M HCl. For the other minerals, the phenanthroline method led to slightly higher values than the ferrozine test and in most cases to an overestimation of Fe(tot) in comparison to the external ICP-AES control (Fig. 3.2A). For ferrihydrite and the mixture of goethite and magnetite, the ferrozine test precisely matched the ICP-AES results, while the Fe(tot) concentrations of goethite, pyrite, and magnetite were underestimated by 71, 66, and 25%, respectively. However, the difference between both methods is not significant neither for aqueous Fe solutions nor ferrihydrite.

Elevation of the incubation temperature to 60 °C and an HCl concentration of 6 M completely dissolved all tested minerals, including highly crystalline oxides and sulfides like goethite, magnetite, and pyrite. Dissolution in 6 M HCl at 60 °C for 1 or 4 days for goethite and pyrite led to a good agreement of measured Fe(tot) concentrations vs. the external control for all sample types (Fig. 3.2A). Here, the ferrozine assay almost exactly reflected the ICP-AES results with a deviation of less than 5%. The phenanthroline method often led to an overestimation by 5 to 10% (Fig. 3.2A) but the difference between both methods is not significant. For pyrite, the measurements with phenanthroline resulted in 91% of the externally determined concentration, while the ferrozine method led to a severe overestimation of 145% of the actual concentration.

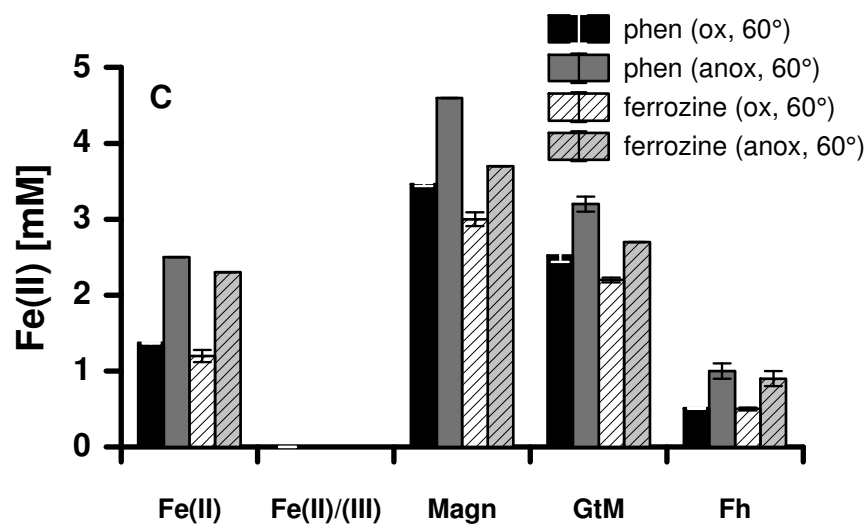
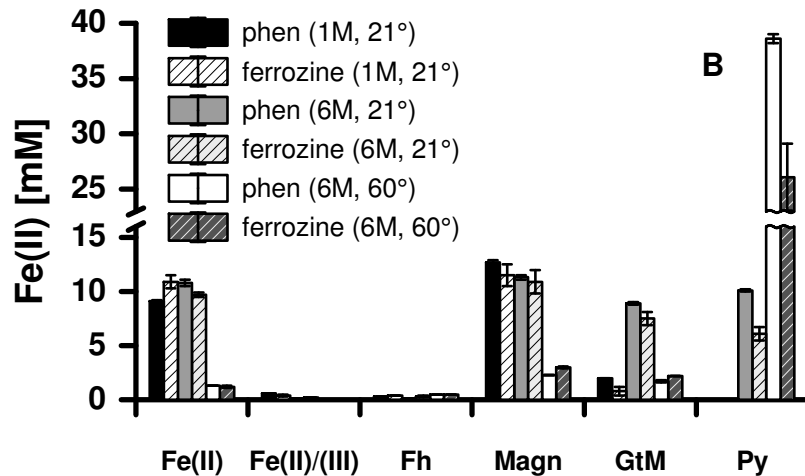
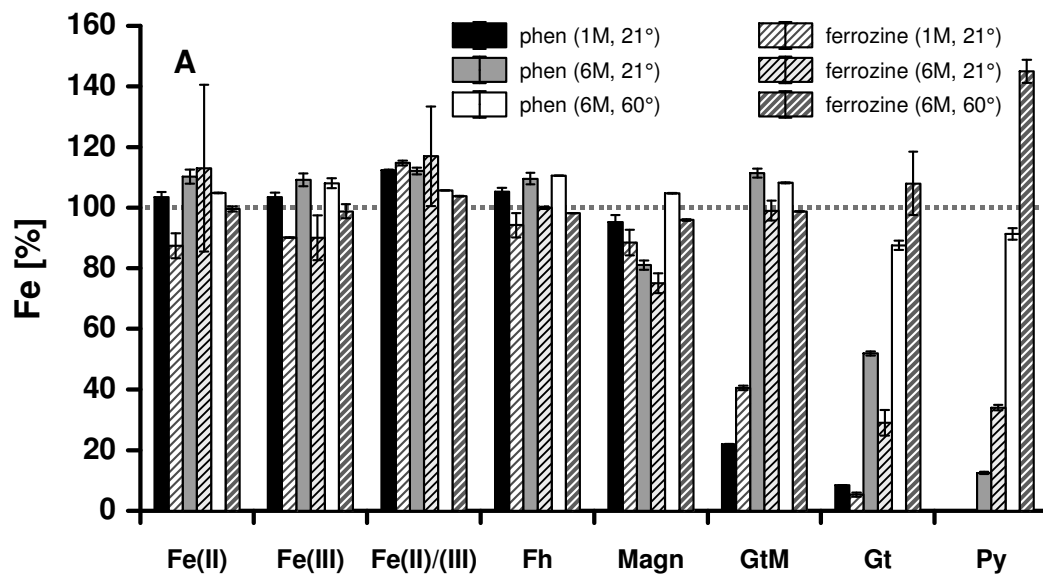


**Fig. 3.2:** Comparison of extraction methods and Fe determination from different samples. A) Total Fe related to ICP measurements as external standard. B) Ferrous Fe concentrations under oxic conditions and C) ferrous Fe under oxic (ox) and anoxic (anox) conditions. Values were obtained by the ferrozine and the phenanthroline (phen) assays. Error bars depict the standard deviations from three parallel measurements of one sample.

### 3.1.2 Ferrous Fe determination

When Fe(II) was the only Fe species, the phenanthroline method exactly matched the concentrations determined by ICP-AES, whereas ferrozine overestimated by 14% (1.5 mM). No reliable Fe(II) determination was achieved, when the concentration in the samples was below 0.5 mM, since deviations of expected to measured values were larger than 100%. Ferrous Fe concentrations of magnetite and the mixture of goethite and magnetite after dissolution in 1 M HCl at 21 °C (Fig. 3.2B) were higher for the phenanthroline assay than for ferrozine. However, the true amounts of Fe(II) in magnetite and in the mixture of goethite and magnetite are unknown.

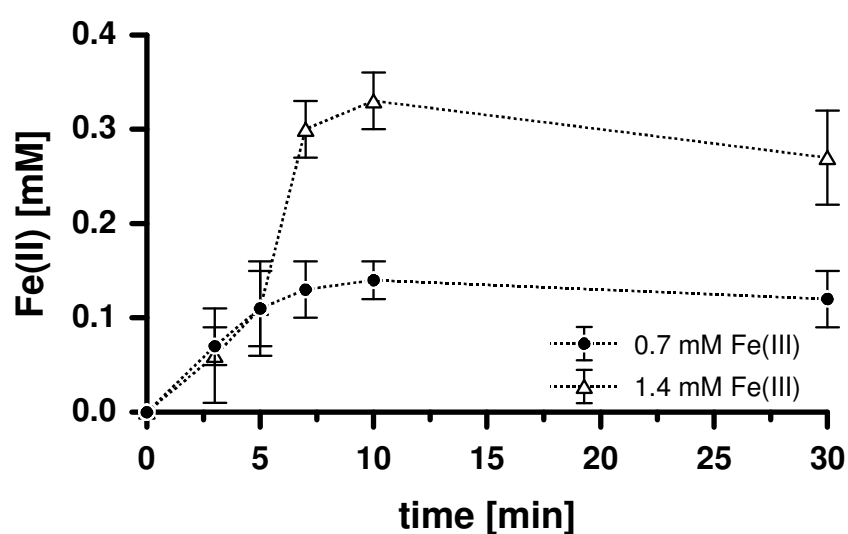


**Fig. 3.3:** Effect of photochemical reduction of Fe(III)-ferrozine complexes of pure Fe(III) stock solutions caused by light irradiation. Error bars depict the standard deviations from six parallel measurements of one sample.

Samples dissolved in 6 M HCl (at 21 °C) yielded slightly reduced Fe(II) concentrations as compared to 1 M HCl treatments (Fig. 3.2B). Ferrous Fe concentrations after 6 M HCl dissolution were somewhat higher for the phenanthroline assay than for the ferrozine assay. However, the Fe(II) concentrations determined with ferrozine matched the ICP-AES concentrations for the samples Fe(II) and Fe(II)/(III). The Fe(II) concentrations of pyrite were underestimated by 70 - 90% by the photometrical tests.

Determined Fe(II) concentrations for Fe(II), magnetite, and the mixture of goethite and magnetite after dissolution in 6 M HCl at 60 °C were 4 to 6-fold lower than after shaking at 21 °C in 1 M or 6 M HCl (Fig. 3.2B). At very low Fe<sup>2+</sup> concentrations as in the Fe(II)/(III) and ferrihydrite samples, Fe(II) was not detectable. For pyrite, the phenanthroline method overestimated the Fe(II) concentrations by about 10%, whereas the ferrozine method led to an underestimation of 23%. For pyrite, the dissolution in 6 M HCl at 60° C and the subsequent

measurement using the phenanthroline assay was the only method almost matching the externally determined concentration (90%).

For ferrozine, I could observe a photochemical reduction of Fe(III)-ferrozine complexes by light (Fig. 3.3). During a maximal incubation time of a sample with ferrozine in a microtiter plate of 5 min during which all samples were processed, 8 to 15% of the Fe(III) were reduced.

However, for ferrous Fe determinations the ferrozine and phenanthroline methods did not show systematic differences.

### 3.1.3 *Oxic vs. anoxic extraction*

For the minerals magnetite, ferrihydrite, a mixture of goethite and magnetite as well as the Fe(II)<sub>aq</sub> and mixed valence solutions, anoxic incubation almost doubled the detectable Fe<sup>2+</sup> concentrations after shaking in 6 M HCl at 60 °C for 4 days (Fig. 3.2C). Nevertheless, the measured concentrations were only 20 to 30% of the Fe<sup>2+</sup> measured after shaking in 1 M HCl at 21 °C, whereas the values obtained from the phenanthroline method were slightly higher than those obtained from ferrozine.

### 3.1.4 *Growth experiments*

When Fe(II) and Fe(tot) were analyzed in batch experiments with *G. sulfurreducens* and ferrihydrite as electron acceptor, the ferrozine method matched the externally determined Fe(tot) concentrations to 100% (Fig. 3.4A). In two other experiments, deviations of 5 and 8% occurred, respectively. Concentrations obtained with the phenanthroline method were 8 to 13% higher than the reference concentrations determined with ICP-AES. Single measurements of the samples dissolved in 1 M HCl showed that both methods overestimated the ICP-AES concentrations during the first 100 h. Afterwards, ferrozine tended to underestimate, whereas phenanthroline matched the ICP-AES results. After dissolution in 6 M HCl at 60 °C, the single values of every time point determined with ferrozine varied between ±5 mM (10% of total Fe), while phenanthroline overestimated in general about 10%, occasionally up to 40%.

For oxic treatment at 21 °C, the Fe(II) values after dissolution in 6 M HCl were less than 50% of the measured concentration after dissolution in 1 M HCl for both methods (Fig. 3.4B). After dissolution in 6 M HCl at 60 °C, no Fe(II) was detectable. Anoxic treatment improved all results. Especially after dissolution in 6 M HCl at 21 °C, the recovery was up to 40% of the Fe(tot) concentration and led to results close to 1 M HCl samples (Fig. 3.4C). However, the concentrations measured after dissolution at 60 °C in 6 M HCl were up to 50% lower than the results obtained after dissolution at 21 °C.

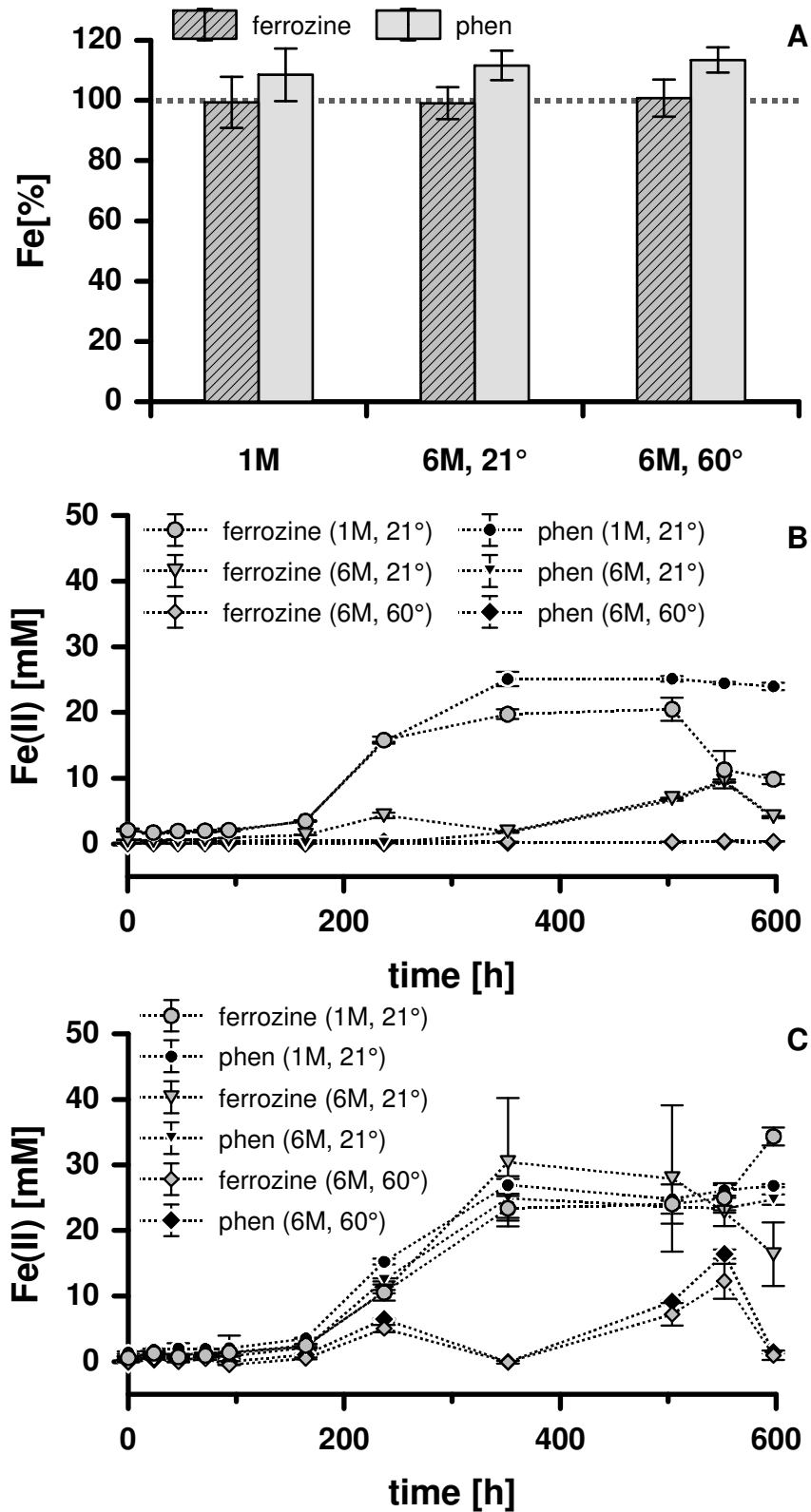


**Fig. 3.4:** Comparison of extraction methods and Fe determination from samples of a growth experiment of *G. sulfurreducens* on synthetic ferrihydrite. A) Total Fe concentrations of added Fe oxides related to ICP measurements as external standard and B) ferrous Fe concentrations under oxic and C) anoxic conditions. Total Fe concentrations and their standard deviations are calculated as mean values from all taken samples.

In almost all treatments, phenanthroline led to higher Fe(tot) concentrations than ferrozine, in a range of 1 to 9% of the total Fe concentration (Fig. 3.4A) and up to 22% in other batches (related to ICP-AES data). Only after treatment with 6 M HCl at 21 °C, ferrozine yielded higher concentrations of 1 and 8% of Fe(tot).

### 3.1.5 Influence of medium composition

In most cases, results determined for total Fe (Fig. 3.5A) showed significantly higher values for ferrozine than for phenanthroline, which contradicts to Fig. 3.2A and 3.4A. Addition of trace element solution as well as the vitamin solution led to underestimation of up to 20% for both methods.

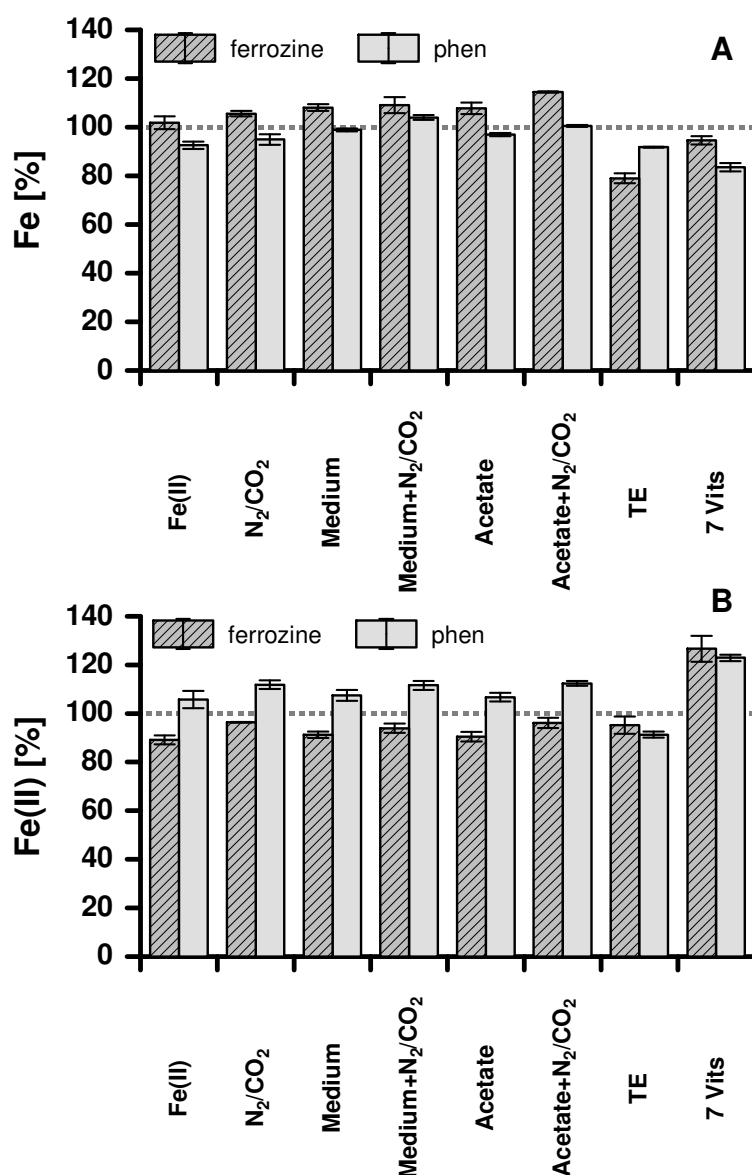


**Fig. 3.5:** Total A) and ferrous Fe concentrations B) of FeCl<sub>2</sub> solutions treated with different medium additives. N<sub>2</sub>/CO<sub>2</sub>: flushed with N<sub>2</sub>/CO<sub>2</sub>, Medium: freshwater medium, TE: trace elements, 7 Vits: vitamin solution.

For Fe(II) determination, the trend of significant phenanthroline over- and ferrozine underestimation of the ICP data could be confirmed (Fig. 3.5B). The addition of trace element solution led to an underestimation of 5 and 9% for the ferrozine and phenanthroline methods, respectively. An opposite effect was observed after mixing with the vitamin solution, which led to overestimations of >20% for both methods.

### 3.2 Low molecular weight organic acids influence microbial Fe oxide reduction via a dissolution-disaggregation mechanism

#### 3.2.1 Sample characterization

Mössbauer spectroscopy of ferrihydrite incubated in citrate-free low salt medium revealed no magnetic ordering at room temperature but the onset of magnetic ordering at 77 K (Tab. 3.1). Magnetic ordering of citrate-incubated ferrihydrite (molar citr:Fe = 0.16) was only observed at ~5 K. The absence of a magnetic ordering at 77 K in both samples identified 2-line ferrihydrite as the single ferric Fe phase, with a slight higher crystallinity of the citrate-incubated ferrihydrite.

**Tab. 3.1:** Hyperfine parameters of ferrihydrite and ferrihydrite incubated with citrate (citr:Fe = 0.16) at room temperature, 77 K, and ~ 5 K.

	room temperature		77 K			~ 5K		
	$\delta^1$ [mm s <sup>-1</sup> ]	$\Delta^2$ [mm s <sup>-1</sup> ]	$\delta$ [mm s <sup>-1</sup> ]	$\Delta$ [mm s <sup>-1</sup> ]	$B_{hf}^3$ [T]	$\delta$ [mm s <sup>-1</sup> ]	$\Delta$ [mm s <sup>-1</sup> ]	$B_{hf}$ [T]
ferrihydrite	0.35	0.74	0.46	0.77		0.46	-0.04	48.8
ferrihydrite + citrate	0.35	0.73	0.46	0.71	9.5	0.46	-0.03	48.4

<sup>1</sup>isomeric shift; <sup>2</sup>quadrupole splitting; <sup>3</sup>hyperfine field

The FTIR spectrum of ferrihydrite without citrate incubation showed the typical patterns of ferrihydrite with the H<sub>2</sub>O deformation mode at 1623 cm<sup>-1</sup> and the symmetric and asymmetric C-O stretches at 1346 and 1463 cm<sup>-1</sup>, respectively (Fig. 3.6). C-O stretches probably stemmed from adsorbed carbonate of ambient CO<sub>2</sub> [145]. Sorption of citrate on ferrihydrite surfaces caused the formation of two broad peaks of the symmetric and asymmetric stretches of the carboxylate groups of citrate at 1382 and near 1580 cm<sup>-1</sup>, which superimposed the H<sub>2</sub>O and C-O stretches of ferrihydrite and carbonate (Fig. 3.6A) [146]. With increasing citr/Fe ratio, the intensity of those two peaks also increased. A new band developed already at citr/Fe ratios of 0.04 at 1253 cm<sup>-1</sup>, stemming from C-O stretches of carboxylate groups. With increasing citrate concentrations, these C-O stretches became more pronounced and a further C-O stretch at 1066 cm<sup>-1</sup> occurred

[146]. Not adsorbed citrate caused the development of a band pair from C-H deformations at 908 and 851  $\text{cm}^{-1}$  at a citr/Fe ratio of 0.2.

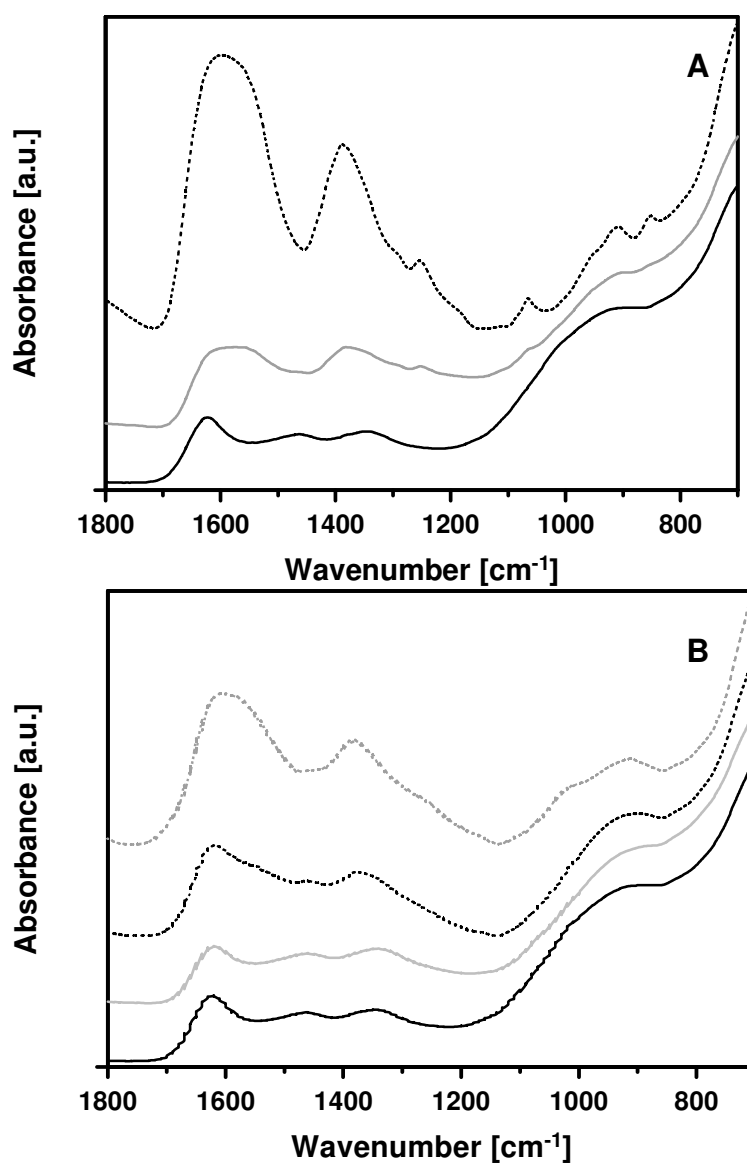


**Fig. 3.6:** FTIR spectra of ferrihydrite incubated with different citrate concentrations (A) with molar citrate:Fe ratios of 0.0 (solid black line), 0.04 (solid grey line), and 0.2 (dotted black line) and with different humic acid concentrations (B) with molar organic carbon (OC):Fe ratios of 0.0 (solid black line), 0.03 (solid grey line), 0.3 (dotted black line), and 0.9 (dotted grey line). Absorbance is given in arbitrary units (a.u.).

Adsorption of humic acids onto ferrihydrite surfaces led to increased peak intensities of symmetric and asymmetric C-O stretches, with a shift of the symmetric deformation from 1346  $\text{cm}^{-1}$  to 1380  $\text{cm}^{-1}$  at C/Fe ratios of 0.3 and more (Fig. 3.6B).



### 3.2.2 Dissolution of ferrihydrite and colloid stabilization

Incubation of ferrihydrite with citrate resulted in partial dissolution of the ferrihydrite within the first 70 h when citrate concentrations were  $> 0.5$  mM. With increasing molar citr/Fe ratios, the amount of released Fe increased up to 93% at a ratio of 0.5 and reached 100% at a ratio of 1.7 of the positive control (Fig. 3.7A). Dissolution rates increased from  $6.4 \mu\text{M h}^{-1}$  (citr/Fe = 0.1) up to  $37 \mu\text{M h}^{-1}$  (citr/Fe = 1.7) (Fig. 3.7A). The pH remained at a constant level of approximately 6.3 over the entire experiment.

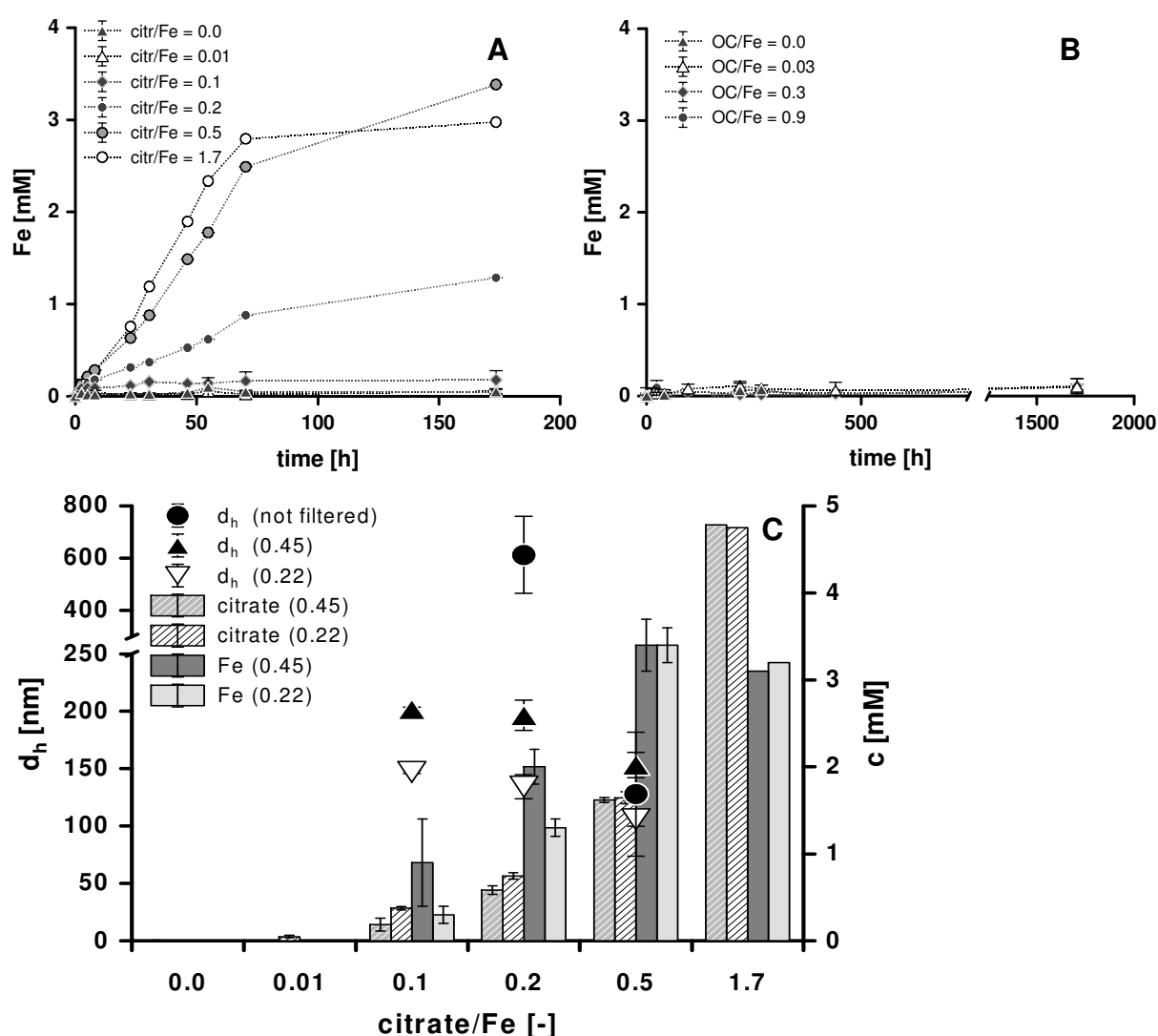


**Fig. 3.7:** Abiotic dissolution of ferrihydrite with citrate (A) with molar citrate:Fe ratios of 0.0-1.7 (average total Fe concentration:  $3.3 (\pm 0.3)$  mM) and humic acids (B) with molar organic carbon (OC):Fe ratios of 0.0-0.9 (average total Fe concentration:  $2.9 (\pm 0.3)$  mM). Characterization of filtrates of citrate-incubated ferrihydrite (C) depicts Fe and citrate concentrations as grey and striped bars, respectively; dots and triangles show hydrodynamic diameters ( $d_h$ ) of detected colloids. Error bars depict standard deviations of three measurements of three independent samples.

Incubation of ferrihydrite with Gohy humic acids (HA) did not lead to a detectable dissolution of ferrihydrite after 71 days (Fig. 3.7B). The pH decreased slightly from  $6.1 \pm 0.1$  to  $5.5 \pm 0.1$  during the experiment.

After filtration of the samples, both the positive control (citr/Fe = 1.7) and the citr/Fe = 0.5 sample showed a 100% recovery of the total Fe concentration (Fig. 3.7C). Iron concentrations in the filtrates of samples with molar citr/Fe ratios between 0.1 and 0.5 were at least twice as high as the citrate concentrations. No citrate or Fe was detectable in filtrates of samples without citrate or with a citr/Fe ratio of 0.01. No Fe was detected in filtrates of ferrihydrite incubated with HA (data not shown).

In samples with citr/Fe ratios between 0.1 and 0.5, colloidal dispersed particles with declining hydrodynamic diameters between  $153 (\pm 11) - 202 (\pm 2)$  nm and  $106 (\pm 6) - 147 (\pm 1)$  nm were detected in 0.45 and 0.22  $\mu\text{m}$ -filtrates, respectively. Unfiltered samples with molar citr/Fe ratios of 0.2 and 0.5 had respective hydrodynamic diameters of  $612 (\pm 147)$  and  $128 (\pm 54)$  nm. Zeta potentials of these particles were between  $-38.4 (\pm 0.5)$  mV and  $-41.2 (\pm 1.1)$  mV. In my experimental setup no stably dispersed particles could be detected in Gohy humic acids-containing samples (data not shown).

### 3.2.3 Microbial reduction by *G. sulfurreducens*

Microbial reduction of ferrihydrite incubated with different citrate concentrations revealed increasing initial reduction rates with increasing citrate concentrations, except for a citr/Fe ratio of 0.03 (Fig. 3.8). Here, the reduction rates decreased slightly from  $0.03 \text{ mM h}^{-1}$  (without citrate) to  $0.02 \text{ mM h}^{-1}$ . Complete reduction was reached after 30 h for a citr/Fe ratio of 0.58 and after 74 h for ratios of 0.14 and 0.27 (Fig. 3.8).

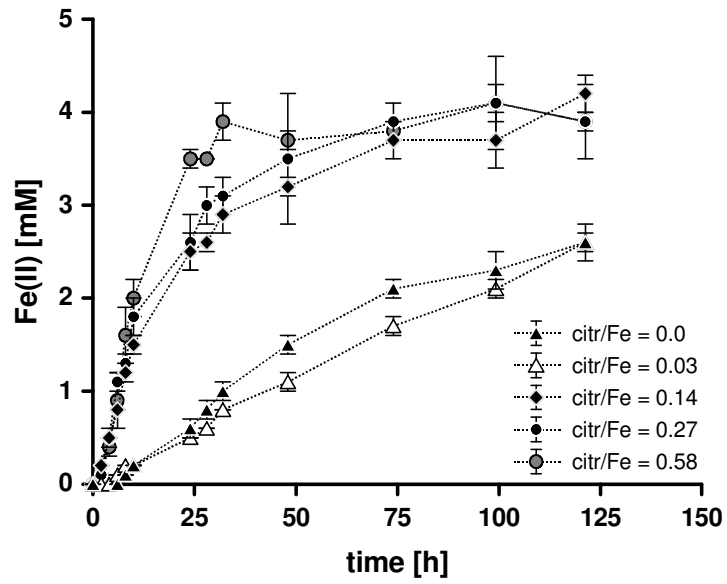


**Fig. 3.8:** Microbial reduction of ferrihydrite incubated with different citrate concentrations with molar citrate:Fe ratios of 0.0-0.58 by *Geobacter sulfurreducens*. Average total Fe concentrations of all samples:  $3.9 \pm 0.1$  mM (n=15). Error bars depict standard deviations of triplicate measurements of three independent samples.

### 3.2.4 Calculation of dissolution and reduction kinetics

Calculated initial dissolution kinetics reproduced measured dissolution kinetics during the first 50 h (Fig. 3.9A).

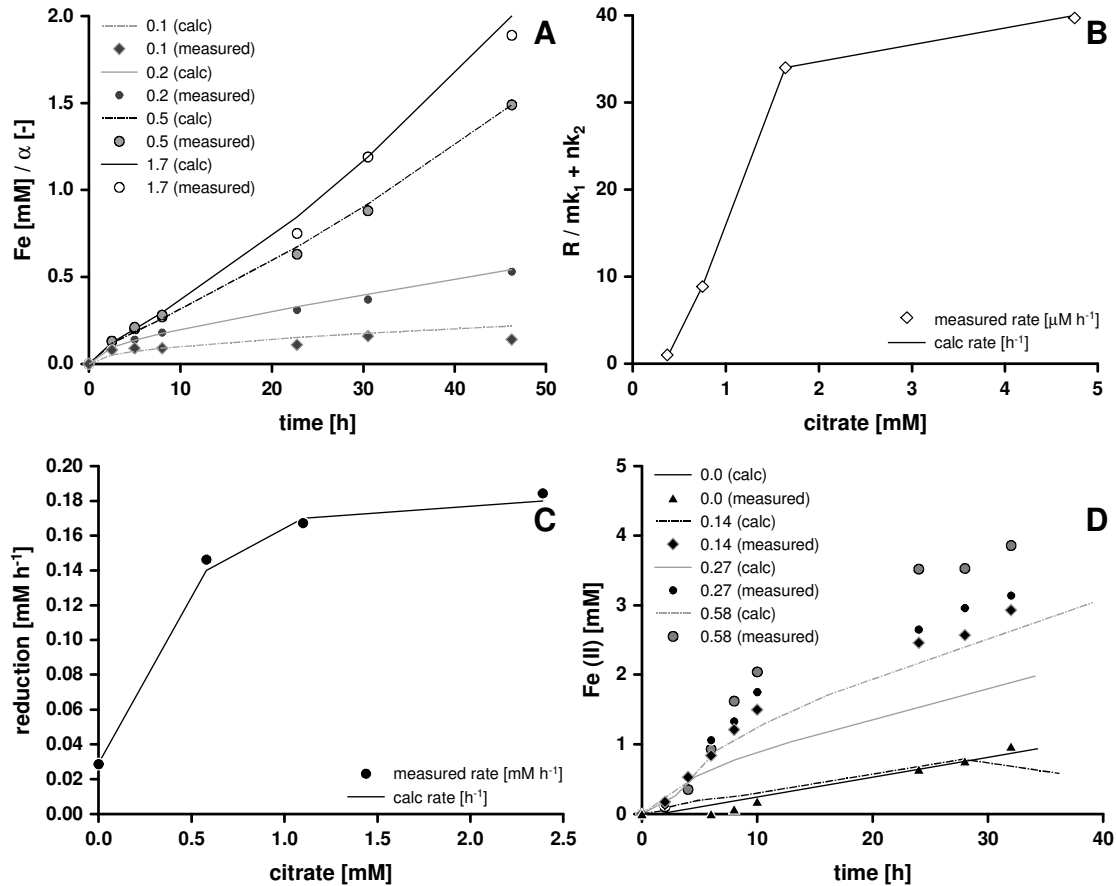


**Fig. 3.9:** Comparison of calculated data with measured citrate-induced dissolution kinetics of ferrihydrite over time (A) and dissolution rates in dependence of citrate concentrations (B). Microbial reduction rates of *Geobacter sulfurreducens* in dependence of citrate concentrations, causing dissolution of ferrihydrite and colloid stabilization, could be described with a Michaelis-Menten kinetic (C). Calculated microbial reduction kinetics excluding colloid stabilization compared to measured reduction kinetics over time (D). Symbols represent measured data points for respective molar citrate:Fe ratios (0.0-1.7), lines represent calculated data.

The stepwise determination of reduced Fe at different time points matched to microbial reduction within the first 35 h at a citr/Fe ratio of 0.0 (Fig. 3.9D). At a ratio of 0.14, the calculation did not fit and significantly underestimated the measured Fe oxide reduction. At ratios of 0.27 and 0.58 the measured first 5 h of reduction could be described. Afterwards, the calculated curves dropped faster than the measured reduction.

### 3.3 Reduced biotic and abiotic reactivity of ferrihydrite nanoparticles below a critical aggregate size<sup>3</sup>

#### 3.3.1 Characterization of synthesized Fe oxides

FTIR spectra of 2LFh 1 and 2LFh 2 showed typical ferrihydrite patterns (Fig. 3.10). The region between 1700 and 1200  $\text{cm}^{-1}$  showed the deformation mode of  $\text{H}_2\text{O}$  ( $\sim 1620 \text{ cm}^{-1}$ ) and the asymmetric and symmetric C-O stretching modes of adsorbed carbonate at  $\sim 1460 \text{ cm}^{-1}$  and  $\sim 1345 \text{ cm}^{-1}$ , respectively [145]. For 2LFh2, these bends were slightly shifted to higher wavenumbers. Fe-O lattice stretching modes and OH deformation modes appeared at  $\sim 420$ ,  $\sim 570$ , and  $\sim 690 \text{ cm}^{-1}$  for 2LFh 1 and at 464, 580, and  $700 \text{ cm}^{-1}$  for 2LFh 2 [134, 145]. Nitrate appeared in the spectrum of 2LFh 1 at  $1384 \text{ cm}^{-1}$ . The C-O total symmetric stretch of carbonate appeared at  $1090 \text{ cm}^{-1}$  in the spectrum of 2LFh 2 [145].

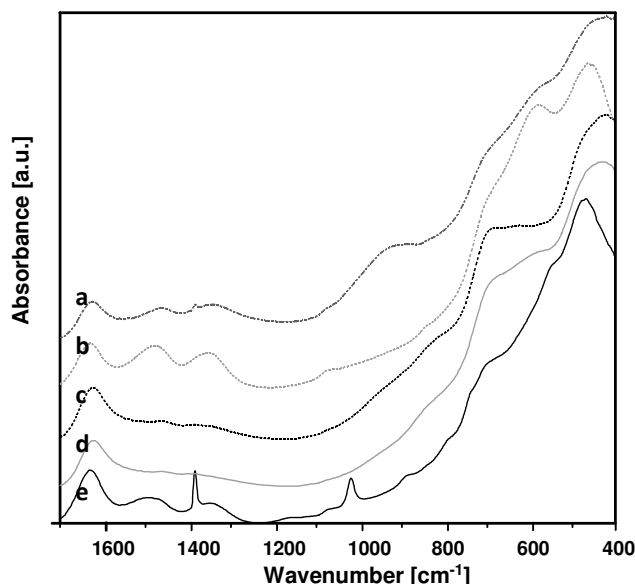


**Fig. 3.10:** FTIR spectra of (a) 2LFh 1, (b) 2LFh 2, (c) 2LFh 3, (d) 6LFh 1, and (e) 6LFh 2. Absorbance is given in arbitrary units (a.u.)

The spectrum of 2LFh 3 contained bends at  $1622 \text{ cm}^{-1}$  of the deformation mode of  $\text{H}_2\text{O}$  and both C-O stretching modes of adsorbed carbonate at  $1468$  and  $1370 \text{ cm}^{-1}$ . A plateau in the region between  $570$  and  $700 \text{ cm}^{-1}$  was formed by Fe-O stretches of akaganeite at  $623$  and  $686 \text{ cm}^{-1}$  [134, 147, 148] and of ferrihydrite at  $\sim 580 \text{ cm}^{-1}$  [134, 145]. A shoulder near  $810 \text{ cm}^{-1}$  was caused by libration modes of O-H-Cl [147]. The spectrum of 6LFh 1 contained the sharp  $\text{H}_2\text{O}$  deformation mode at  $1621 \text{ cm}^{-1}$  and very weak C-O stretching modes at  $1462$  and  $1386 \text{ cm}^{-1}$  [145]. O-H deformations appeared near  $690 \text{ cm}^{-1}$  [134] and Fe-O lattice stretching modes of ferrihydrite near  $570$  and  $431 \text{ cm}^{-1}$  [145]. The spectrum of 6LFh 2 showed O-H deformation bands near  $468$  and

<sup>3</sup> This chapter was submitted to *Geochimica et Cosmochimica Acta* on 27.02.2013

700  $\text{cm}^{-1}$  [134] and the Fe-O lattice stretching at 550  $\text{cm}^{-1}$  [145]. Weak shoulders near 877 and 800  $\text{cm}^{-1}$  showed Fe-OH inplane and out of-plane bending vibrations of goethite [149]. The band at 1019  $\text{cm}^{-1}$  stems from the O-H out of-plane bend of lepidocrocite [134]. Nitrate is visible at the peak at 1384  $\text{cm}^{-1}$ .

X-ray diffraction results (Fig. 3.11) confirmed the mineralogical composition obtained by the analysis of the FTIR spectra. Diffraction data of 2LFh 1 and 2LFh 2 showed two broad peaks at 39.6 and 73°2 $\theta$ , typical for 2-line ferrihydrite. The diffractogram of 2LFh 3 displayed eight sharp peaks with the peaks at 12.9, 18.5, 31.0, 45.6, 54.1, 65.5, and 72.6°2 $\theta$  stemming from akaganeite. At 41.1°2 $\theta$ , both ferrihydrite, and akaganeite formed distinct peaks. The diffractogram of 6LFh 1 consisted of a ferrihydrite peak at 41.1°2 $\theta$  and five weakly established, broad peaks at 45.6, 52.7, 66.3, 73.0, and 73.6°2 $\theta$  from 6-line ferrihydrite. 6LFh 2 showed peaks at 14.5 and 31.1°2 $\theta$  which can be assigned to akaganeite. The peak at 31.1°2 $\theta$  can be assigned to lepidocrocite as detected in the respective FTIR spectrum. The presence of akaganeite, which can be indicated by the peaks at 14.5 and 31.2°2 $\theta$  is unlikely, since no Cl<sup>-</sup> was present in the system. 6-line ferrihydrite formed the peaks at 41.4, 46.8, 61.7, and 72.5°2 $\theta$ . No peak could be assigned to goethite.

N<sub>2</sub> physisorption measurements revealed that all ferrihydrites contained micropores with the exception of 2LFh 3 and 6LFh 2 (Tab. 3.3).

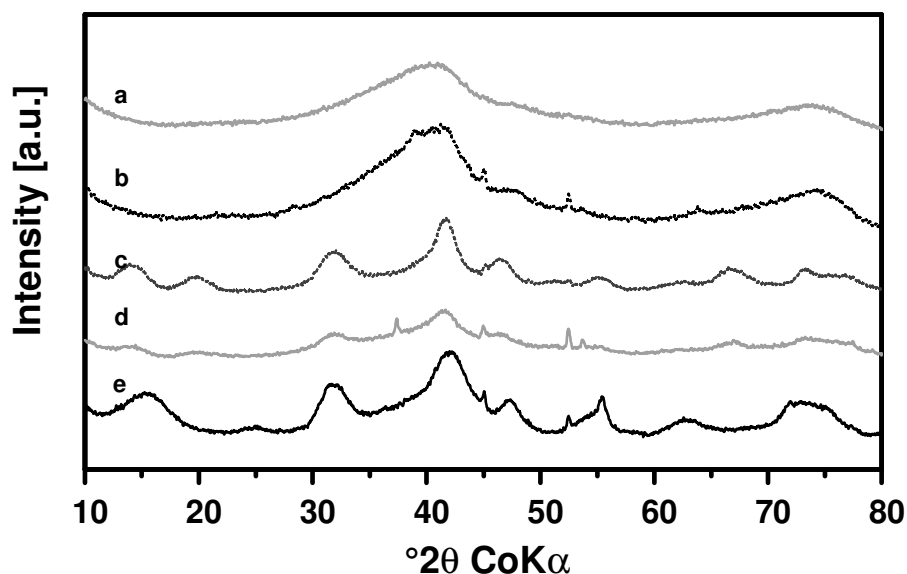


**Fig. 3.11:** XRD patterns of (a) 2LFh 1, (b) 2LFh 2, (c) 2LFh 3, (d) 6LFh 1, and (e) 6LFh 2. Peak of NaCl (37.2°2 $\theta$ ) originates from synthesis, peaks at 44 and 52°2 $\theta$  from the aluminum sample holder. Intensity is given in arbitrary units (a.u.).

The BET specific surface area measurements were in the range of  $213.5 \pm 1.2$  and  $331.2 \pm 0.3 \text{ m}^2 \text{ g}^{-1}$  (Tab.3.3) and thus were within the reported range for synthetic ferrihydrite [134]. 6LFh 2 was the only stable nanoparticulate suspension without particle aggregation. All other samples formed

large aggregates and tended to sediment in MilliQ purified water (Tab. 3.3). Consequently, SEM images of the samples showed strong aggregated crust-like structures (Appendix Fig. A4.1), most likely formed during air-drying on the sample holder.

**Table 3.2:** Binding energies of the Cl2p<sub>3/2</sub>, C1s photoemission peaks, and Fe2p<sub>3/2</sub> satellite features associated with the synthetic ferrihydrite samples used in microbial and abiotic reduction experiments

sample	Cl2p <sub>3/2</sub> (Cl) [eV BE]	C1s (CO <sub>3</sub> ) [eV BE]	Fe2p <sub>3/2</sub> (Fe(II)) satellite [eV BE]
2LFh 1		288.7 eV	(~715)*
2LFh 2		288.7 eV	~715
2LFh 3	198.4	288.7 eV	(~715)*
6LFh 1	198.4	288.7 eV	(~715)*
6LFh 2		288.7 eV	(~715)*

\*brackets indicate that occurrence of peak is uncertain

To gain additional information about adsorbed anions on ferrihydrite surfaces, XPS spectroscopy was used. Weak peaks at binding energies (BE) of 288.7 eV in all spectra correlated with carbonate bound C (Tab. 3.2) [150]. Distinct Cl2p<sub>3/2</sub> peaks at 198.4 eV, occurring in spectra of 2LFh 3 and 6LFh 1, were indicative of a Cl<sup>-</sup> species [150]. Fitting of the Fe2p<sub>3/2</sub> peak, using a multiplet Fe peak fitting strategy [151, 152], revealed Fe<sup>2+</sup> concentrations of 10.3% (2LFh 1), 17.9% (2LFh 2), 13.4% (2LFh 3), 11.3% (6LFh 1), and 4.3% (6LFh 2). The uncertainty of Fe<sup>2+</sup> estimation was ±2.5 %, caused by the background selection under the Fe 2p<sub>3/2</sub> peak.

### 3.3.2 Reduction kinetics

The reduction kinetics of the ferrihydrite samples with ascorbic acid showed no relationship to the specific surface area (Fig. 3.12A). The highest initial reduction rates were detected for 2LFh 1, 2LFh 2, and 6LFh 1, which did not contain secondary mineral phases like goethite or lepidocrocite. Surprisingly, 6LFh 2, which is the only stable colloidal suspension, revealed the lowest abiotic reduction rate. The maximum extent of abiotic reduction was reached after 43 h for all ferrihydrite samples but only 2LFh 1 and 2LFh 2 were completely reduced. 2LFh 3, 6LFh 1, and 6LFh 2 were reduced to 79, 87, and 78%, respectively.

Microbial reduction of 5 mmol L<sup>-1</sup> of the respective ferrihydrite samples by *G. sulfurreducens* was very slow, with a lag phase of about 2 days. Initial reduction rates were two orders of magnitude lower than abiotic reduction with ascorbic acid (Figure 3.12B).

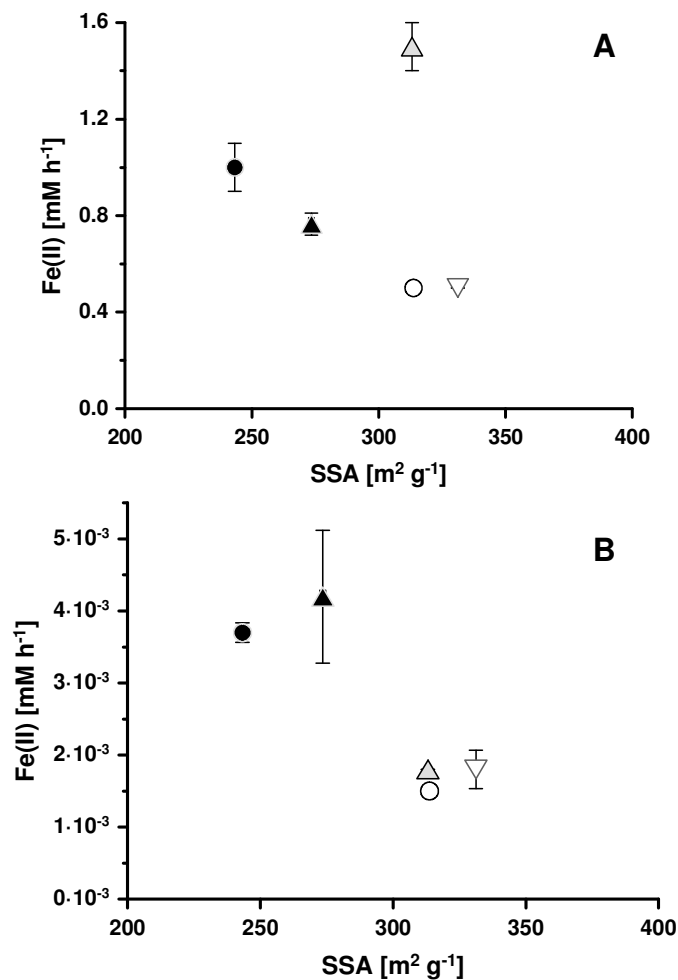


**Fig. 3.12:** Initial reduction rates of ferrihydrite samples [2LFh 1 (△), 2LFh 2 (▲), 2LFh 3 (▽), 6LFh 1 (●), and 6LFh 2 (○)] compared with their specific surface area for reductive dissolution with ascorbic acid (A) and microbial reduction by *Geobacter sulfurreducens* (B). Total Fe concentrations are  $4.9 \pm 0.7$  mM and  $4.7 \pm 0.3$  mM for abiotic reductive dissolution and microbial reduction, respectively. Error bars depict the standard deviations from triplicate batch incubations.

No relationship could be observed between the initial microbial reduction rates and the specific surface area of the ferrihydrite samples. The highest initial reduction rates were observed for 2LFh 2 and 6LFh 1. The lowest reactivities were obtained for the ferrihydrites with the highest surface areas, which are 2LFh 1, 2LFh 3, and 6LFh 2 (Fig. 3.12, Tab. 3.3). The most conspicuous difference between biotic and abiotic reduction was observed for 2LFh 1. Its high abiotic reactivity with ascorbic acid was in strong contrast to low microbial reduction rates.

### 3.3.3 Abiotic dissolution in 1 M HCl

Ferrihydrite samples which did not contain secondary mineral phases (2LFh 1, 2LFh 2, 6LFh 1) were dissolved immediately after addition to 1 M HCl (Fig. 3.13). The dissolution of 2LFh 3 and 6LFh 1, both containing higher crystalline Fe oxides like akaganeite or goethite and lepidocrocite, respectively, were dissolved more slowly. After 30 min, 100% of 2LFh 3 and 80% of 6LFh 2 were dissolved.



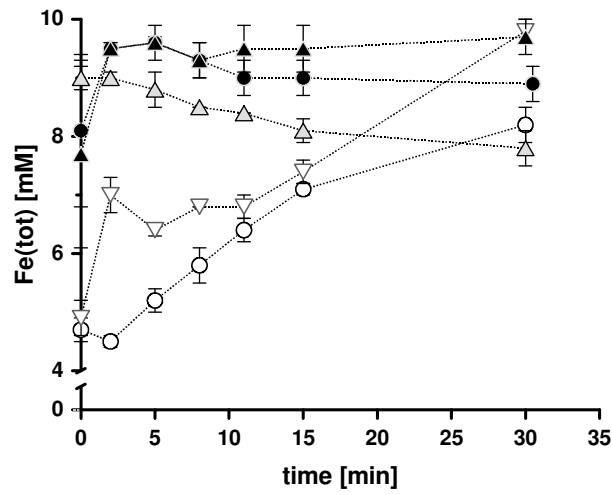


**Fig. 3.13:** Abiotic dissolution of all ferrihydrite samples [2LFh 1 (△), 2LFh 2 (▲), 2LFh 3 (▽), 6LFh 1 (●), 6LFh 2 (○)] in 1 M HCl. Total Fe concentration is  $9.4 \pm 0.7$  mM. Error bars depict standard deviations of triplicate batch incubations.

Tab. 3.3: Mineralogical composition and properties of Fe oxides and their respective initial reduction rates.

Mineral composition*		Adsorbed anions		Morphology			Initial reduction rates				
XRD	FTIR	FTIR	XPS	BET specific surface area [m <sup>2</sup> g <sup>-1</sup> ]	t-method micropore surface area [m <sup>2</sup> g <sup>-1</sup> ]	Hydrodynamic diameter ( $d_H$ ) [nm]	Abiotic (ascorbic acid)		Biotic ( <i>G. sulfurreducens</i> )		
							Initial reduction rate [mM h <sup>-1</sup> ]	% reduced	Cell normalized rate [fmol h <sup>-1</sup> cell <sup>-1</sup> ]	% reduced	
2LFh 1	2-line Fh	Fh	NO <sub>3</sub> <sup>-</sup> , CO <sub>3</sub> <sup>2-</sup>	Fe <sup>2+</sup> , (CO <sub>3</sub> <sup>2-</sup> )	313.1 ± 0.2	51.12 ± 0.07	2,402**	1.5 ± 0.1	97.3 ± 1.8	0.07 ± 0.02	28.0 ± 1.9
2LFh 2	2-line Fh	Fh	CO <sub>3</sub> <sup>2-</sup>	Fe <sup>2+</sup> , (CO <sub>3</sub> <sup>2-</sup> )	273.5 ± 1.1	56.23 ± 0.37	1,473**	0.8 ± 0.04	104.1 ± 2.5	0.19 ± 0.04	47.2 ± 11.0
2LFh 3	Akaganeite	Fh, Akaganeite	CO <sub>3</sub> <sup>2-</sup>	Fe <sup>2+</sup> , Cl <sup>-</sup> , (CO <sub>3</sub> <sup>2-</sup> )	331.2 ± 0.3	0	886	0.5 ± 0.02	78.6 ± 4.2	0.06 ± 0.01	19.0 ± 3.8
6LFh 1	6-line Fh	6-line Fh	CO <sub>3</sub> <sup>2-</sup>	Fe <sup>2+</sup> , Cl <sup>-</sup> , (CO <sub>3</sub> <sup>2-</sup> )	243.3 ± 0.1	35.57 ± 0.28	1,975**	1.0 ± 0.1	86.6 ± 1.8	0.14 ± 0.01	30.3 ± 0.8
6LFh 2	6-line Fh	Fh, Lepidocrocite, Goethite	NO <sub>3</sub> <sup>-</sup> , CO <sub>3</sub> <sup>2-</sup>	Fe <sup>2+</sup> , (CO <sub>3</sub> <sup>2-</sup> )	313.7 ± 1.2	0	162 / 7	0.5 ± 0.02	77.8 ± 6.8	0.06 ± 0.00	16.4 ± 2.2

\* differences between FTIR and XRD have to be assigned to different sensitivities of both methods

\*\* sedimenting aggregates

## 4 Discussion

### 4.1 Reevaluation of colorimetric Fe determination methods commonly used in geomicrobiology<sup>4</sup>

This study compares the application of the colorimetric phenanthroline and ferrozine assays for the determination of Fe(II) and Fe(tot) in microbiological samples. The experiments were focused on different acidic strengths, incubation temperature, and incubation time. Based on these data, I can now provide a robust dataset for choosing the appropriate method for the determination of Fe concentrations in geomicrobiological studies.

#### 4.1.1 Quantification of total Fe content

The comparison of photometric Fe quantifications with external validation by ICP-AES of different Fe oxides proved the general suitability of both the phenanthroline and ferrozine assays for the Fe(tot) determination of typical geomicrobiological Fe samples. Especially the easy dissolvable species such as aqueous Fe(II) and Fe(III) solutions, and amorphous ferrihydrite were reliably determined, independent of the assay type or dissolution procedure, with phenanthroline being slightly more accurate.

The main problem for the analysis of crystalline Fe oxides was their poor solubility. Dissolution procedures turned out to be decisive for precise Fe quantification. Mean values of several measurements of the growth experiment showed that the results obtained with the ferrozine assay fitted best, regardless of acidic strength or dissolution temperature. During growth of *G. sulfurreducens*, ferrihydrite recrystallized to magnetite which is hardly soluble in 1 M HCl. However,

---

<sup>4</sup> This chapter was published in *Journal of Microbiological Methods* 89 (2012) 41-48

results of the phenanthroline method were frequently higher than results obtained with ferrozine and the ICP-AES reference concentrations. This effect is already described by Anastácio et al. [153] and is attributed to the complete dissolution of minerals by phenanthroline.

Interferences with  $\text{Co}^{2+}$ ,  $\text{Cu}^{2+}$ ,  $\text{Mn}^{2+}$ , and  $\text{Zn}^{2+}$  [154-158], which have absorption maxima between 300 and 530 nm, could be excluded. These cations were present in the applied freshwater medium with concentrations of 0.96, 0.01, 0.76, and 0.84  $\mu\text{M}$ , respectively. Besides,  $\text{Fe}(\text{tot})$  determination of  $\text{Fe}(\text{II})$  solutions spiked with trace elements led to underestimated values for both methods. Taylor et al. [159] showed that metabolic products of cells can form strong complexes with  $\text{Fe}(\text{II})$  and  $\text{Fe}(\text{III})$  which are characterized by pH independent thermodynamic stability. To my knowledge, it is not described until now whether *G. sulfurreducens* is also able to produce such strong complexation agents which are not destroyable by 1 M HCl. Possibly, phenanthroline can dissolve these complexes in contrast to ferrozine which may explain lower values obtained with ferrozine compared to phenanthroline in biological samples in contrast to the abiotic experiments (Fig. 3.5A). Vitamins, having similar complexing properties, might explain the underestimation of the  $\text{Fe}(\text{tot})$  content with ferrozine and phenanthroline by 5 and 16%, respectively. Independent from the additives and flushing with  $\text{N}_2/\text{CO}_2$ , the values were slightly higher for ferrozine (Fig. 3.5A). However, the overestimation of the  $\text{Fe}(\text{tot})$  content with phenanthroline in biological samples still remained unclear.

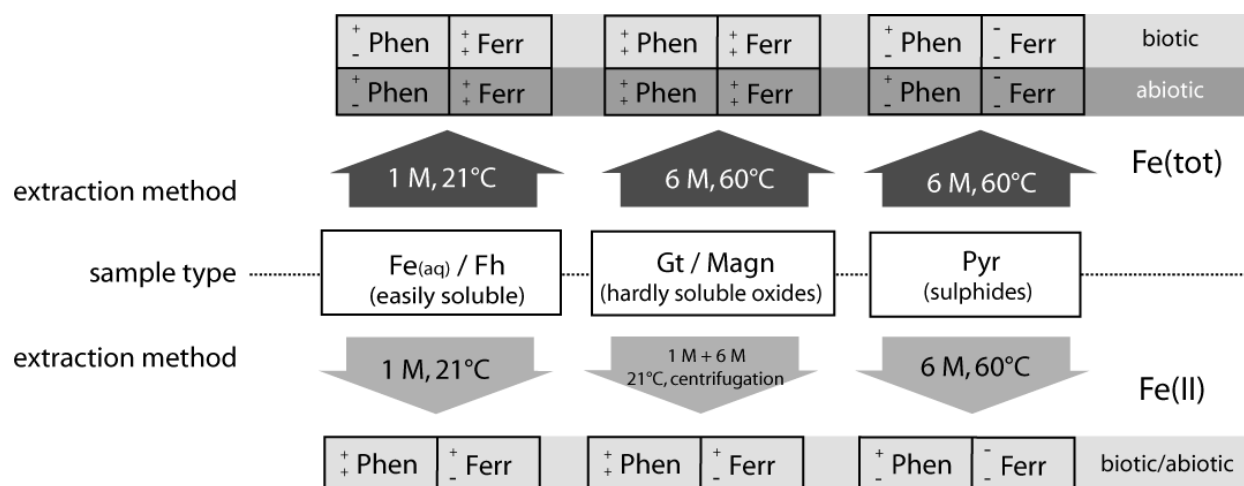


**Fig. 4.1:** Proposed extraction methods and Fe determination assays for different sample types. + depicts combinations of extraction and analysis methods producing very accurate results. ± stands for less accurate but recommended methods whereas combinations labeled with - are not recommended to use. The upper part of the figure shows combinations for total Fe ( $\text{Fe}(\text{tot})$ ), the lower for ferrous Fe ( $\text{Fe}(\text{II})$ ) analysis.

The phenanthroline method proved to be suited best for the determination of total pyritic Fe after dissolution in 6 M HCl at 60 °C. High concentrations of sulphide seem to affect the ferrozine complex [160], leading to overestimation in the photometric measurements. However, a brownish precipitate, as described by these authors, was not observed in this study.

The best results for Fe(tot) determination of highly crystalline Fe oxides, such as goethite and magnetite, were obtained with the ferrozine assay after dissolution in 6 M HCl at 60 °C (Fig. 4.1). However, the increase of acidic strength without increasing temperature did not improve the results apart from goethite and a mixture of goethite and magnetite. For easily dissolvable compounds in biotic samples such as ferrihydrite or Fe(II)<sub>aq</sub> which were incubated in 1 M HCl at 21 °C, the best results are obtained by the phenanthroline assay. Mean values of several measurements with the ferrozine method were in excellent accordance with the external validation. Therefore, and due to the time consuming procedure of the phenanthroline method, I advocate the ferrozine assay for measurements of large sample numbers.

#### 4.1.2 Ferrous Fe determination

Ferrous Fe concentrations were measured with highest accuracy at 21 °C. Nevertheless, both photometric methods tended to overestimate actual Fe(II) concentrations in biological samples. For ferrozine, this can be attributed to a photochemical reduction of the Fe(III)-ferrozine complex which was also observed by Anastácio et al. [153]. For the phenanthroline assay, photochemical reduction can be excluded due to the addition of a masking agent. A similar overestimation of Fe(II) determination was observed for the mixed valence sample Fe(II)/(III). I assigned this overestimation to a decreasing reliability of both assays with decreasing concentrations.

Iron determinations of the growth experiment frequently showed higher concentrations for the phenanthroline method compared to ferrozine (Fig. 3.4B). However, the exact Fe(II) concentrations are not known. Nevertheless, in the context of overestimation for Fe(tot) with phenanthroline in biotic samples, I assume an overestimation here as well. Conspicuously, single measurements of the same sample are more erratic for ferrozine than for phenanthroline. Anastácio et al. [153] explained these fluctuations with the light sensitivity of ferrozine and the partial dissolution of highly crystalline Fe oxides. For Fe(II), interferences with medium additives could be excluded for both methods. Independently of the additive, values obtained by phenanthroline are mostly up to 5% higher than ICP data, whereas ferrozine showed up to 5% lower concentrations. The high concentrations after addition of the vitamin solution could be attributed to interference with the vitamin's self-absorption with two maxima at 552 and 517 nm.

As described for determination of the total Fe content, the low solubility of highly crystalline samples reduced the measurable concentration of Fe(II). The detected concentrations of Fe(II) in the mixture of goethite and magnetite at 21 °C were not convincing due to the low solubility of goethite and magnetite and the resulting high turbidity of the sample. Ferrous Fe incorporated into the crystal lattice could probably not react with phenanthroline and ferrozine.

The low Fe(II) concentrations determined for incubations at 60 °C might be due to a fast abiotic oxidation of Fe(II) [161, 162]. Porsch and Kappler [163] explained this observation with the formation of Fe(II) – Cl<sup>-</sup> complexes and undissociated HCl, leading to Fe – HCl complexes. Both complexes lead to a faster oxidation of Fe(II). Anoxic sampling improved the Fe(II) recovery, but the underestimation was still significant, indicating that Fe(II) might oxidize during the 4 days incubation in 6 M HCl. The only mineral which was not affected by oxidation was pyrite. Schoonen et al. [164] attributed this effect to the faster sulfide oxidation, causing suppression of Fe oxidation at pH values below 3 and under illumination with visible light. A concentration close to the reference ICP-AES concentration of the pyrite sample was measured with phenanthroline. The lower results with ferrozine could also be evoked by the interference between ferrozine and sulphide.

In summary, for easily dissolvable compounds such as ferrihydrite and Fe(II)<sub>aq</sub>, I recommend 1 M HCl for dissolution with an incubation time of 24 hours (Fig. 4.1). More crystalline minerals such as goethite or magnetite have to be dissolved in 6 M HCl at 60 °C for accurate Fe measurement. In contrast to the Fe(tot) determination, heating of the acidified samples is not recommended for subsequent measurements of Fe(II) because Fe(II) will oxidize. An opportunity to overcome the difficulty of Fe(II) determination in samples with hardly soluble Fe oxides is the partial dissolution of the samples in 6 M HCl at 21 °C. To avoid the interference of the turbid solutions with the colored ferrozine or phenanthroline complexes, the acidified samples should be centrifuged with subsequent determination of the Fe<sup>2+</sup> content in the supernatant. Most accurate results for pyrite were obtained using the time consuming phenanthroline assay. To avoid possible interferences with different cations, I recommend using the ferrozine assay which is usually accurate within ± 10% for both Fe(II) and Fe(tot) measurements.

## 4.2 Low molecular weight organic acids influence microbial Fe oxide reduction via a dissolution-disaggregation mechanism

### 4.2.1 Sample characterization

Mössbauer spectroscopy showed that the pure ferrihydrite incubated in citrate-free microbial low salt medium and ferrihydrite incubated with citrate are 2-line ferrihydrites. The onset of magnetic ordering at 77 K of pure ferrihydrite revealed a slightly higher crystallinity compared to ferrihydrite incubated with citrate. Different publications [165-167] described the recrystallization of synthetic 2-line ferrihydrite to a mixture of 6-line ferrihydrite, hematite, and hydromaghemite in the presence of citrate at elevated temperatures of at least 100 °C. An increase of magnetic susceptibility was observed for ferrihydrite-citrate coprecipitates at moderate temperatures of 25 and 50 °C [168]. Those recrystallization processes can be excluded for ferrihydrite samples with adsorbed citrate in the present study because no evidence for increased magnetic splitting was found. It could be that starting transformation to higher crystalline Fe oxides of pure ferrihydrite at incubation temperatures of 30 °C can cause the slightly higher crystallinity compared to ferrihydrite-citrate incubations, although no hematite was detected [166]. Most likely recrystallization of citrate-incubated ferrihydrite (citr/Fe = 0.16) was inhibited due to less aggregation caused by adsorbed citrate [169].

Adsorption of citrate onto ferrihydrite surfaces led to an intense increase of symmetric and asymmetric C-O stretching modes (Fig. 3.6A). Three COO<sup>-</sup> groups of citrate are responsible for its anchoring on surfaces resulting in peak maxima near 1590 cm<sup>-1</sup> for asymmetric stretching and at 1380 and 1440 cm<sup>-1</sup> for symmetric stretching deformations [146]. Dialysis of ferrihydrite-citrate samples resulted in a single symmetric stretching peak at 1380 cm<sup>-1</sup> [146], probably due to formation of inner-sphere complexes [170]. The symmetric C-O stretch at 1346 cm<sup>-1</sup> shifted also to higher wavenumbers for adsorbed humic acids at C/Fe ratios of 0.3 and 0.9, suggesting a similar inner-sphere complexation as for Fe-citrate (Fig. 3.6B). Furthermore, the asymmetric C-O stretching mode shifts to lower frequencies at a C/Fe ratio of 0.9, caused by weaker outer-sphere complexes [171].

### 4.2.2 Dissolution and colloid stabilization

Abiotic citrate-induced dissolution rates of ferrihydrite increased with increasing initial citrate concentrations (Fig. 3.7A) which is in accordance with findings of Liang et al. [172]. Since ferrihydrite is a macroaggregate consisting of crystallites in the size range between 2 to 6 nm [8] the surface site density for citrate adsorption is higher compared to other Fe oxides. Citrate adsorption onto these “inner surfaces” between single aggregated particles leads to repulsive

forces between these particles. According to the DLVO theory [6, 7] attractive forces dominate if the electrochemical double layer shrinks due to neutralization of the positive surface charge with few adsorbed citrate anions. This effect can be seen at a citr/Fe ratio of 0.01 (Fig. 3.7A). Here, no ferrihydrite disaggregation was detected. At increasing citrate concentrations, the surface charge of ferrihydrite turned to negative values, resulting in electrostatic repulsion forces between single particles and colloid stabilization from ferrihydrite macroaggregates. Similar observations were described in a study about ferrihydrite coated quartz sand columns [172]. The citrate-containing influent led to the release of ferrihydrite colloids from the ferrihydrite surface coating. The authors suggested interfacial forces between citrate coated quartz sand and citrate coated ferrihydrite led to repulsion between these different compounds. However, the authors did not take into account that citrate coatings may cause also electrostatic repulsive forces between small ferrihydrite aggregates. In my experiments, these electrostatic repulsion forces resulted in the disintegration of ferrihydrite macroaggregates to colloids of about 100 – 200 nm in diameter at citr/Fe ratios of at least 0.1 (Fig. 3.7C). No stably dispersed colloids were detectable at a citr/Fe ratio  $> 1$  because of a complete dissolution of ferrihydrite with excess citrate. Stabilization of colloids also explained the higher Fe concentrations relative to citrate in filtrates of samples with citr/Fe ratios of 0.1 – 0.5. According to Martin [173],  $\text{FeCitrH}_1^-$  complexes dominate over  $\text{FeCitr}_2^{3-}$  at pH values between 6 and 7. Consequently, I expected citr/Fe ratios of about 1 in filtrates if dissolution is the only process taking place. However, the results showed an actual ratio of  $\sim 0.4$ , which can be well explained by the presence of citrate-coated colloids.

The stabilization of colloids may also cause the nonlinear dissolution of Fe over time (Fig. 3.9A). Liang et al. [172] attributed the nonlinear dissolution to the polydisperse nature of ferrihydrite, with aggregates and smaller particles present. Smaller particles dissolve faster than aggregated ferrihydrite resulting in a decrease of initial reduction after consumption of small particles. In my experiments, the decreasing dissolution rate within the first 10 h could be described by equation 2.1 and represents the decreasing fast initial dissolution caused by vanishing of small particles. After citrate adsorption to the ferrihydrite aggregate surfaces, ligand exchange reactions between ferrihydrite and citrate started. These dissolution reactions weaken the intra-aggregate structure. Together with electrostatic repulsion forces between smaller aggregates, this leads to separation and colloid stabilization. At a citr/Fe ratio of 0.1 approximately all citrate molecules were adsorbed at the time point of colloid stabilization. After ligand exchange, ferric citrate detached from the surfaces. Further dissolution was not possible since all citrate was saturated with ferric Fe. Therefore, the dissolution could be perfectly described with equation 2.1. At citr/Fe ratios  $> 0.1$  a certain amount of citrate remained in solution when all surface sites of the ferrihydrite macroaggregates were occupied with citrate. After formation of a stable colloidal suspension



(after ~10 h) the available surface area and the amount of sorption sites increased, leading to adsorption of “free” citrate and subsequently to an accelerated dissolution, described by equation 2.2. With increasing citr/Fe ratios the influence of the dissolution of these approximately spherical colloids increased (equation 2.3).

Based on these results I propose an extended dissolution mechanism (Fig. 4.2):

- (i) adsorption of citrate on initially present ferrihydrite colloid surfaces
- (ii) fast dissolution of small, less aggregated particles
- (iii) adsorption of citrate onto surfaces of ferrihydrite macroaggregates until saturation of sorption sites occurs
- (iv) weakening of the surface structure induced by ligand exchange
- (v) electrostatic stabilization of smaller, aggregated particles due to citrate coating and stabilization of colloids, resulting in an increased amount of available surface sorption sites
- (vi) fast adsorption of residual citrate onto new colloidal surfaces and dissolution according to the model of Furrer and Stumm [174].

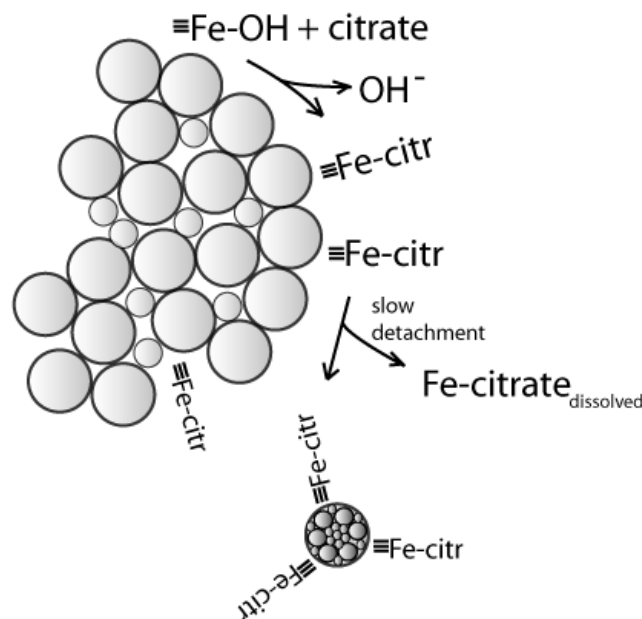


**Fig. 4.2:** Schematic illustration of ferrihydrite dissolution and colloid stabilization in the presence of citrate. Citrate dissolves ferrihydrite via ligand exchange. Adsorbed citrate species on ferrihydrite surfaces stabilize single colloids by electrostatic repulsion.

The used Gohy humic acids did not lead to the stabilization of colloids from ferrihydrite macroaggregates. In contrast to citrate, humic acids dissolved less Fe from ferrihydrite (Fig. 3.7B) leading to less disaggregation of the macroaggregate surfaces compared to citrate. I propose that weakening of macroaggregate surfaces and cracking of intra-aggregate bonds by dissolution is required for colloid stabilization.

#### 4.2.3 Microbial reduction of ferrihydrite in the presence of citrate

Initial microbial reduction rates of ferrihydrite incubated with *G. sulfurreducens* increased with increasing citrate concentrations exceeding a critical minimum concentration (Fig. 3.8). No enhanced reduction was observed at a citr/Fe ratio of 0.03 compared to a ratio of 0.0. This observation was probably caused by the strengthening of aggregates due to surface charge neutralization and therefore decreased bioaccessibility of Fe. Differences of initial reduction rates of samples with citr/Fe ratios between 0.14 and 0.58 are rather low (0.146 – 0.184 mM h<sup>-1</sup>) suggesting that maximum reduction rates are almost reached at a citr/Fe ratio of 0.14.

Calculations of microbial ferrihydrite reduction, which are based on the reduction of dissolved Fe, cannot describe the fast reduction during the first 10-20 h (citr/Fe = 0.14-0.58). This indicates that dissolved Fe is not the only highly available Fe source in the system (Fig. 3.9D). I propose that the differences between calculated and measured microbial reduction rates are caused by the formation of a stable colloidal suspension which was neglected in the calculations. Stably dispersed colloids, as a highly bioavailable Fe source, can be reduced by *G. sulfurreducens* within a few hours, leading to prolonged high reduction rates. My results indicated that the influence of stabilized colloids is more pronounced at low citrate concentrations because the dissolved Fe citrate fraction is rather small. With increasing ratios this difference decreases. I interpret this observation as a decrease of the concentration of stably dispersed colloids, caused by citrate-mediated dissolution of the colloidal fraction. This means that the dissolved fraction increases. Therefore, calculated and measured kinetics converge, because the calculations were based on dissolved Fe only, and not on colloidal Fe. This shows that stable suspensions of ferrihydrite colloids are highly bioavailable, in the same range as dissolved Fe.

The coupled mechanism of citrate-induced dissolution and colloid stabilization from ferrihydrite macroaggregates also explains the catalytic effect of colloidal ferrihydrite on macroaggregate ferrihydrite reduction in a recent study [33]. Similar to the present study, cell suspension experiments with *G. sulfurreducens*, grown on ferric citrate were conducted. In contrast to my study, the cell pellets were washed only once instead of twice, leading to higher residual citrate concentrations in the cell suspension which were then added to the ferrihydrite phase. In experiments with only ferrihydrite macroaggregates, this added citrate had no effect because the concentration was too low. According to the results presented here and without further addition of citrate-containing colloids, the molar citr/Fe ratio of  $\leq 0.04$  resulted in a stronger aggregation of ferrihydrite particles and therefore no enhancement of microbial Fe oxide reduction. In contrast, by addition of 10% colloidal ferrihydrite, the influence of citrate became more important, because the used ferrihydrite colloids were synthesized with ferric citrate. With addition of these colloids the citrate concentration increased, most likely to a citr/Fe ratio of at

least 0.1, leading to slight dissolution and colloid stabilization. Regarding my results, this cannot be ascribed to a catalytic effect of ferrihydrite colloids on microbial ferrihydrite reduction but to an increased amount of stabilized colloids. In the light of this finding I exclude the formerly proposed function of ferrihydrite colloids as electron shuttles [33].

Gohy humic acids did not induce colloid stabilization in my experiments. Enhancement of microbial Fe oxide reduction in the presence of humic acids can therefore completely be attributed to electron shuttling between microbial cells and Fe oxides [40, 42, 45, 175]. However, colloids produced by coprecipitation of humics with ferric Fe might exhibit other properties.

### 4.3 Reduced biotic and abiotic reactivity of ferrihydrite nanoparticles below a critical aggregate size<sup>5</sup>

#### 4.3.1 Secondary minerals

XRD and FTIR confirmed the presence of different higher crystalline Fe oxides (lepidocrocite, goethite, and akaganeite) in the ferrihydrite samples 2LFh 3 and 6LFh 2 (Tab. 3.3). I termed these Fe oxides secondary minerals even though they were likely precipitated at the same time as ferrihydrite. Differences between the two methods have to be assigned to different sensitivities. FTIR analysis revealed the presence of lepidocrocite and goethite for 6LFh 2; the latter could not be confirmed by XRD analysis. Due to the absence of Cl<sup>-</sup> during synthesis, the peak in the diffractogram at 14.5°2θ cannot be ascribed to akaganeite [ $\beta$ -FeO(OH,Cl)]. Therefore, it is assigned to a contaminating phase, which could not be definitely identified.

The lowest abiotic and biotic reduction rates were observed for 2LFh 3 and 6LFh 2, the samples with the highest amounts of akaganeite and a variety of lepidocrocite, goethite, and akaganeite, respectively (Fig. 3.12). Literature describing biotic and abiotic reduction rates of akaganeite are scarce but biotic reduction by *G. sulfurreducens* revealed a two-fold faster initial reduction of 2-line ferrihydrite ( $4.1 \cdot 10^{-7} \text{ mol L}^{-1}\text{m}^{-2}\text{min}^{-1}$ ) compared to akaganeite ( $1.4\text{-}2.4 \cdot 10^{-7} \text{ mol L}^{-1}\text{m}^{-2}\text{min}^{-1}$ ) [176]. A study of Larsen and Postma revealed much lower abiotic reduction rates with ascorbic acid as reducing agent for lepidocrocite and goethite ( $k' = 5.4 \cdot 10^{-6} - 8.1 \cdot 10^{-5} \text{ s}^{-1}$ ) compared to 2-line ferrihydrite ( $k' = 6.6 - 7.6 \cdot 10^{-4} \text{ s}^{-1}$ ), but similar to 6-line ferrihydrite ( $k' = 7.4 \cdot 10^{-5} \text{ s}^{-1}$ ) [21]. Several other studies proved lower reduction rates for higher crystalline Fe oxides compared to ferrihydrite [20, 25]. These results might explain the low abiotic reactivity of 6LFh 2 in my experiments, as it was a mixture of 6-line ferrihydrite, goethite, and lepidocrocite. However, my results were reproducible also with other 6LFh 2 nanoparticles which did not contain XRD

---

<sup>5</sup> This chapter was submitted to *Geochimica et Cosmochimica Acta* on 27.02.2013

detectable amounts of secondary minerals like goethite and lepidocrocite (Appendix Fig. A4.2). Not all the 6-line ferrihydrite samples were less reactive than 2-line ferrihydrite. 6LFh 1 showed similar biotic and abiotic reduction rates as 2-line ferrihydrite (Fig. 3.12).

#### 4.3.2 *Influence of specific surface area and micropores on initial reduction rates*

The comparison of biotic and abiotic reduction rates with the specific surface areas of the respective ferrihydrites showed no correlation (Fig. 3.12). This is in good agreement with the findings of Larsen and Postma [21]. An underestimation of the specific surface areas of the ferrihydrites is likely a result of the freeze-drying procedure, leading to the formation of larger aggregates [177]. Therefore, 6LFh 2 did not have a larger specific surface area as the other samples, although this ferrihydrite was the only stable, non-aggregated suspension with hydrodynamic diameters of 7 nm (Tab. 3.3). Although hydrodynamic diameters of 162 nm were also measured, the 7 nm particles dominate the larger aggregates. Additionally, the accuracy of the BET method is limited because the relatively large N<sub>2</sub> molecule cannot enter small pores [134]. I hypothesize that correlations between the initial reduction rates and the specific surface areas, as it was shown in several studies [25, 178], are valid for comparisons of Fe oxides with different crystallite sizes. Ferrihydrite, as a nanomineral consisting of 2-6 nm sized particles, forms large aggregates during the freeze-drying procedure. Here, the aggregation mechanism, which is triggered by e.g. ionic strength or initial pH, is decisive for controlling the aggregate size in the freeze-dried state and therefore determines the BET specific surface area [126]. It is likely that the influence of the aggregation state on the BET specific surface area is more pronounced for ferrihydrites with similar crystallite sizes than for Fe oxides with crystallites of a larger size range.

For the samples 2LFh 1, 2LFh 2, and 6LFh 1 micropores were detectable by N<sub>2</sub> physisorption measurements (Tab. 3.3). Consequently, these ferrihydrites were faster reduced with ascorbic acid than 2LFh 3 and 6LFh 2 because microporosity facilitates reduction [179]. This is also valid for the initial biotic reduction rates, except for 2LFh 1. It is likely that the low reduction rates of 2LFh 3 and 6LFh 2 are attributed to the high amount of higher crystalline Fe oxides associated with the ferrihydrite. 6LFh 1, a pure ferrihydrite without secondary minerals, possesses a lower degree of crystal order than 2LFh 3 and 6LFh 2. Consequently, the initial biotic and abiotic reduction rates of 6LFh 1 are much higher [25].

#### 4.3.3 *Adsorbed anions*

The presence of nitrate in 2LFh 1 and 6LFh 2 as residue from the synthesis (Fig. 3.10) might cause enhanced abiotic reduction rates for macroaggregates (2LFh 1) but slightly lower reduction

rates for nanoparticles (6LFh 2). This was already observed with goethite nano- and microrods [66]. Here, the lower reduction rate for nanorods was explained by a stronger aggregation behavior, leading to smaller surface areas and therefore to a lower reactivity. FTIR data indicated a high amount of nitrate in the sample of 6LFh 2 but the nanoparticles did not aggregate. Single particles of 7 nm remained stable in suspension in MilliQ water or in 10 mM ascorbic acid. Adsorbed chloride from synthesis, as it was detected in XPS spectra of 2LFh 3 and 6LFh 1 in my preparations (Tab. 3.2), is probably also able to promote stronger aggregation of these samples. However, a decisive inhibitory effect of adsorbed chloride can be excluded because of the high reactivity of 6LFh 1. The low reactivity of 2LFh 3 is most likely attributed to the high amount of associated akaganeite.

In the study of Rubasinghege et al., adsorbed carbonate had a more pronounced effect than nitrate [66]. The authors explained these differences with different adsorption mechanisms of carbonate for micro- and nanorods. They proposed the formation of monodentate complexes of carbonate on the goethite microrod surface but stronger bidentate binuclear complexes with nanorod surfaces. Depending on the adsorption mechanism, the splitting between the symmetric ( $\sim 1360\text{ cm}^{-1}$ ) and asymmetric ( $\sim 1477\text{ cm}^{-1}$ ) C-O stretching is smaller for monodentate complexes than for bidentate or binuclear complexes. For monodentate binding of carbonate to the Fe oxide phase, splitting values of  $\sim 113\text{ cm}^{-1}$  were observed [180], which is in good agreement with the splitting values of all used ferrihydrites in this study with  $102 - 123\text{ cm}^{-1}$ , except for 6LFh 2 with a higher value of  $142\text{ cm}^{-1}$ .

This finding suggests, in accordance with Rubasinghege et al., an increasing tendency of carbonate to form both monodentate and bidentate complexes with ferrihydrite nanoparticles, leading to a stronger passivation of the surface and therefore to lower reactivities [66]. However, the FTIR spectroscopic and XPS results were obtained with freeze-dried samples under atmospheric conditions, leading to contamination with ambient C species prior to XPS and FTIR spectroscopic measurements. Fe oxides used for these studies were prepared under atmospheric conditions, leading to complex formation of C species with the Fe oxide surfaces. After synthesis, all aqueous Fe oxide solutions were flushed with  $\text{N}_2$  for at least 30 min to make the samples anoxic. Fast desorption of 70-80% carbonate from the Fe oxide surface under inert gas conditions after 20 min has been observed before [180]. Assuming a similar carbonate desorption behavior for Fe oxides used in this study, the inhibitory effect caused by adsorbed carbonate on ferrihydrite nanoparticle surfaces of 6LFh 2 can be neglected.

#### 4.3.4 *The role of adsorbed Fe<sup>2+</sup>*

Fitting of the Fe2p<sub>3/2</sub> peak of the XPS spectra resulted in ferrous Fe concentrations in a range of 2-16% for most ferrihydrite samples and a range of 15-20% for 2LFh 2. The presence of detectable amounts of Fe<sup>2+</sup> is peculiar in oxic, freeze-dried samples, but it has to be taken into account that the respective Fe<sup>2+</sup> concentrations are even higher in aqueous, anoxic samples. Adsorbed Fe<sup>2+</sup> has been shown to passivate Fe oxide surfaces and therefore inhibit long-term microbial Fe oxide reduction [181]. The highest concentration of adsorbed Fe<sup>2+</sup> was detected for 2LFh 2. Consequently, microbial reduction of 2LFh 2 should be suppressed by Fe<sup>2+</sup>. Surprisingly, 2LFh 2 was the most reactive ferrihydrite in microbial reduction experiments. Recent studies revealed coupled dissolution via electron transfer from adsorbed Fe<sup>2+</sup> to mineral bound Fe(III), and mineral growth at separate crystallographic mineral sites [182-184]. The authors proposed that electrons flow through the crystal bulk in a “conveyor belt” mechanism. I speculate that a similar mechanism for ferrihydrite with adsorbed Fe<sup>2+</sup> is valid, so that the effect of dissolution and mineral overgrowth should be most pronounced for 2LFh 2. Abiotic recrystallisation of ferrihydrite to goethite and lepidocrocite induced by aqueous Fe<sup>2+</sup> was already confirmed [185]. The presence of different ions from the microbial low salt medium probably led to the incorporation of ions and therefore to increased structural disorder of the fresh precipitates [62]. Higher bioavailability due to the lower crystallinity of these newly formed Fe oxide layers compared to the initial ferrihydrite might lead to higher long-term reduction rates, explaining the high microbial reduction rate of 2LFh 2 compared to the other ferrihydrite samples. This means that, in contrast to the study of Pedersen et al. [185], less crystalline Fe oxide phases than goethite or lepidocrocite might have been formed, possibly triggered by the presence of different salts, trace elements, and vitamins in the microbiological medium. Lepidocrocite in particular forms easily during aeration of FeCl<sub>2</sub> solutions [134] whereas oxidation of reduced, Fe<sup>2+</sup> bearing soil column effluents, containing significant amounts of natural organic matter and ions, led to the formation of ferrihydrite [9].

This effect occurred in the present experimental setup because the rate of microbial reduction by *G. sulfurreducens* is rather slow compared to other studies [9], potentially providing enough time for the development of mineral surface layers.

#### 4.3.5 *Structural properties of ferrihydrite*

The structural model of Drits et al. proposes a three-component-system for ferrihydrite: (i) a nanoporous defect-free ferrihydrite phase, (ii) defective ferrihydrite, and (iii) fine dispersed hematite [186]. According to this theory, all ferrihydrites are mixtures of 6-line ferrihydrite and hematite at different ratios and with different coherent scattering domains. The XRD

diffractograms of 2LFh 1 and 2LFh 2 fit very well to calculated XRD curves of a mixture of defective and defect-free ferrihydrite and fine dispersed hematite, with all components having very small scattering domains [186]. The diffractogram of 6LFh 2 is also in accordance with this theory. Differences between 6LFh 1 and 6LFh 2 were broader full widths at half maximum of the peaks for 6LFh 1, meaning lower crystallinity of 6LFh 1 compared to 6LFh 2. The diffractogram of 6LFh 2 showed a very diffuse maximum at  $\sim 38^\circ 2\theta$ , which is not present in the diffractogram of 6LFh 1 (Fig. 3.11). According to Drits et al. such diffuse maxima derive from the fine dispersed hematite phase, which is more dominant in 6LFh 2 [186]. The peak at  $31.12^\circ 2\theta$  of 6LFh 2, which was previously assigned to akaganeite or lepidocrocite, might also be explained by a super lattice reflection of the defective ferrihydrite phase [186].

An important aspect of the structural ferrihydrite model of Drits et al. is the presence of channels and cavities in the defect-free ferrihydrite phase [186]. A recent study with three different 2-line ferrihydrites observed a proportional relationship between solubility of the samples in HCl and the presence of micropores [179]. In accordance with these findings, 10 mM of the samples 2LFh 1, 2LFh 2, and 6LFh 1, respectively, were immediately dissolved in 1 M HCl, whereas 6LFh 2 was only partly dissolved after 30 min (Fig. 3.13). Micropore analysis of the ferrihydrite samples revealed the presence of micropores for 2LFh 1, 2LFh 2, and 6LFh 1, but no micropores for 2LFh 3 (which is mainly akaganeite) and 6LFh 2 (Tab. 3.3). These findings, together with the XRD peak at  $31.1^\circ 2\theta$ , suggest the dominant presence of defective ferrihydrite and fine dispersed hematite in sample 6LFh 2, but low concentration of porous defect-free ferrihydrite.

#### 4.3.6 *Dissolution self-inhibition for small aggregates*

This study showed that non-aggregated ferrihydrite nanoparticles like 6LFh 2 are less reactive than larger aggregates. This is in conflict with other studies. In a recent publication, the abiotic dissolution of nanoparticulate goethite with  $\text{HNO}_3$  decreased significantly with increasing particle size and with an increased aggregation state [187]. Initial dissolution rates of hematite with ascorbic acid were faster for 7 nm particles ( $9.11 \pm 2.24 \cdot 10^{-7} \text{ mol m}^{-2} \text{ h}^{-1}$ ) than for 30 nm particles ( $4.48 \pm 1.62 \cdot 10^{-7} \text{ mol m}^{-2} \text{ h}^{-1}$ ) [22]. The main reason for the higher reactivity of the 7 nm particles was attributed to the presence of fine dispersed nanoparticles which dissolved much faster than aggregates, whereas the reductive dissolution of the larger nanoparticles was initiated from surface defects like pits and edges. These observations cannot be confirmed for ferrihydrite in the present study.

Mineral dissolution starting from edges and ledges on the surface very likely has a bigger influence on bulk dissolution than the dissolution at atomic-scale defects and dislocations [188]. The dissolution “stepwave” model extended this theory: at the beginning of dissolution, etch pits

open up on the mineral surface, causing the development of stepwaves [189]. Those stepwaves can travel over the mineral surface and might control the bulk dissolution. Furthermore, only larger pits (of size greater than a critical value) are active for dissolution of hydroxyapatite [23]. If the crystallite size decreases to the same size range as the critical pit size, the dissolution of hydroxyapatite was inhibited because dominantly smaller pits were formed, which are not active in dissolution. Assuming that these mechanisms can be applied also to the dissolution of ferrihydrite, two properties of 6LFh 2 have to be taken into account: (i) the low aggregation state and (ii) the low porosity. I postulate that aggregation of particles produces a certain amount of edges and steps on the aggregate surface which are not present on surfaces of single crystals. Those surface defects, present in aggregated ferrihydrites, can act as nucleating holes for etch pits and become a constant source of stepwaves [189], leading to fast dissolution. In 6LFh 2, these aggregation-mediated defects are absent and only small etch pits can develop, which are less reactive, resulting in lower dissolution kinetics. This effect is reproducible with an akaganeite-containing ferrihydrite, which was prepared according to the protocol of Larsen and Postma [21]. The particles were in the same size range as 6LFh 2 and did not aggregate, but showed a similarly low abiotic reactivity in ascorbic acid (Appendix Fig. A4.3). The reactivity of these nanoparticles are below the reactivity of 2LFh 3, which also contained akaganeite as dominant Fe species. In both preparations no micropores were detected, meaning that the higher reactivity of the aggregates was not determined by a higher porosity.

The low porosity of 6LFh 2 might have the same effect on its reactivity as the low aggregation state. Similar to higher surface roughness arising from aggregation, pores can function as nucleating holes for etch pits. Both effects are hard to distinguish during abiotic reductive dissolution experiments with ascorbic acid because aggregation was inhibited for all ferrihydrite samples. This implies that the observed reduction rates were mainly triggered by pore sizes ( $2LFh\ 1 = 2LFh\ 2 > 6LFh\ 1$ ) and eventually crystallite size. In contrast, all ferrihydrites aggregated in microbial low salt medium in biotic batch incubations due to the presence of ions and the near neutral pH. Therefore, the influence of aggregation and surface defects increased. This effect is probably responsible for the reverse initial reduction rates for 2LFh 1 and 2LFh 2 in biotic and abiotic experiments. Whereas 2LFh 1 formed loose aggregates, 2LFh 2 formed large, mainly irreversible flakes. It is likely that these flakes stem from ferrihydrite attached to bacterial cell surfaces [31].

In summary, the low aggregation state and low porosity of 6LFh 2 seem to trigger its reactivity. My hypothesis implies that a stable nanoparticulate ferrihydrite suspension with low aggregation state is less reactive than a more aggregated suspension if both porosity and the amount of crystallite surface defects of the respective ferrihydrite preparation are very low.



## 5 Summary, conclusions, and outlook

Iron oxide reduction is a major respiratory process especially in anoxic soils and groundwaters. In contrast to other electron acceptors such as nitrate and sulphate, the microbial availability is limited by its poor solubility under circumneutral pH conditions. Microorganisms developed several strategies to overcome this limitation e.g. by shuttling substances that can facilitate the electron transfer between microbial cells and structural Fe(III) centers of Fe oxides. In other cases microbial reduction was promoted by partial dissolution of Fe oxides by excretion of complexing ligands or the presence of extracellular ligands. The solubility and its controlling factors are of major importance for microbial reduction processes and are the main focus of this study.

The goal of the thesis was to determine which mineralogical features are decisive for ferrihydrite reactivity and how organic ligands promote microbial accessibility.

The first objective of this study was to evaluate the commonly applied photochemical Fe determination methods using ferrozine and phenanthroline as complexing agents. Based on these results the applied Fe determination method for the other projects of the thesis was chosen. Both methods turned out to be reliable in determination of ferrous and total Fe concentrations of dissolved or easily soluble Fe species. For higher crystalline Fe oxides (e.g. goethite, magnetite) the extraction method is more important than the choice of the photometrical method. Especially heating of samples diluted with 6 M HCl is very efficient in dissolving all crystal bound Fe but fast abiotic oxidation makes ferrous Fe determination impossible after this treatment. Therefore, extraction at room temperature and subsequent centrifugation is needed to avoid abiotic oxidation and interference of turbid solutions with the photometric reagent. Attention has to be paid for microbial samples. Metabolic products of cells may form strong complexes with Fe

which are resistant against 1 M HCl, leading to underestimation of measured Fe with the ferrozine method. Possibly, phenanthroline can dissolve these complexes.

However, the harmful effects of phenanthroline to health and the smooth application of the ferrozine method for a large amount of samples led to the decision to use the ferrozine method for all experiments of the thesis. The recommendations on the proper usage of the Fe determination methods have been made available to the scientific community [144]. Now, based on a wide dataset the proper method for a specific application can be chosen what ensures reproducible measurements.

The chapters 3.2 and 4.2 are dealing with the influence of citrate on microbial Fe oxide reduction. Until now, the chelating effect of low molecular weight organic acids like oxalate or citrate was extensively investigated (e.g.[190-192]). This process is of environmental significance because plant roots excrete those substances in times of Fe or phosphorous deficiency to increase the concentration of accessible nutrients [193-195]. Only dissolution processes and factors involved were studied so far. However, chelator-induced dissolution of Fe oxides requires the adsorption of the chelating agent like citrate. The present study provides a theory involving the formation of stable colloidal suspensions from macroaggregate ferrihydrite driven by electrostatic stabilization of sub-aggregates in the nanosize range. These stabilized colloids are more reactive than macroaggregates and therefore better accessible to Fe-reducing microorganisms, leading to higher reduction rates.

In the environment, the formation of stably dispersed Fe oxide colloids induced by citrate or oxalate excretion in rhizospheres may be an important source for mobile colloids. Considering the results of this thesis, those colloids could increase the microbial availability of Fe oxides in soils significantly. This is of vital importance in soils with oxidic and reduced horizons as a result of contact with groundwater (gley) or stagnating surface water (stagnosol). Here, Fe oxide redox cycling [67, 68, 74] is taking place, involving the coupling of Fe oxide reduction in anoxic zones and the subsequent oxidation of ferrous Fe in oxic compartments. The presence of Fe oxide colloids could significantly facilitate this mechanism. At sites contaminated with organic compounds like BTEX, higher turnover rates of Fe oxide colloids might then probably result in faster degradation of these organic substances, used as electron donor for Fe reducing microorganisms.

Furthermore, the generation of stably dispersed colloids could increase the mobility of Fe oxides in soils. Those particles can be relocated by e.g. seepage water. Caused by the high affinity of heavy metals and metalloids to Fe oxide surfaces, a co-transport and further distribution of these pollutants is likely.

The increased reactivity of nanosized ferrihydrite aggregates compared to their macroaggregate counterparts is in accordance with observations of other studies [9, 33]. Nanoparticles are considered to be highly reactive due to their large specific surface area, higher amount of reactive surface sites, and variations in their atomic structure. With increasing aggregation state, the surface area and the reactive surface sites decrease, leading to reduced reactivity. The findings presented in the chapters 3.3 and 4.3 cannot support this commonly applied theory. They rather show that ferrihydrite with a weak aggregation state loses its reactivity drastically. Caused by fewer surface defects or structural changes the reactivity decreases below the level of macroaggregates. With a low aggregation state structural properties like microporosity determine the reactivity of ferrihydrite. These results indicate that the reactivity of minerals does not necessarily increase if size decreases to a few nanometres. These findings are of critical importance for Fe-based remediation technologies like permeable reactive barriers. Furthermore, ferrous Fe adsorbed onto ferrihydrite surfaces seemed to promote microbial Fe oxide reduction by a coupled mineral growth – dissolution mechanism instead of inhibition as it was described previously [181].

The results of the thesis have shown that a decreasing aggregate size to a certain extent of about 100-200 nm enhances microbial reactivity drastically. Disintegration of macroaggregates to the nano-scale may provide a pool of highly bioaccessible Fe oxides in the environment. However, with decreasing aggregation state below a critical size, reactivity diminishes again. This is the first time a break in the usual pattern of Fe oxide nanoparticle reactivity was reported, highlighting the need for deeper investigations. Therefore, indications are given that at least ferrihydrite needs the assemblage of several particles to provide the maximal reactivity.

These findings can be of special interest for material science and biotechnology where the field of engineered nanoparticles is thriving. Nanoparticles and nanofluids have seen an enormous growth in popularity during the last two decades [196] because of their outstanding properties compared to larger particles. They are widely applied e.g. as catalysts, solar absorbers, microwave absorbers, and in biomedicine. The distribution of a variety of nanoparticles in the environment is concomitant with the increased production of engineered nanoparticles. The investigation of their fate in soils, sediment, and groundwaters as well as their interactions with micro- and soil organisms, plants and fungi is a growing research field. Surfaces of those nanoparticles alter under environmental conditions, causing changes of their properties and therefore their interactions with the environment. The toxicity of nanoparticles is strongly discussed. The awareness that some materials lose their reactivity with decreasing particle or aggregate size by changed surface properties can be of importance for the development of production processes. Probably, engineered nanoparticle production might be optimized towards less toxicity. The

design of nanoparticles is decisive for their interactions with biological systems and determines their interactions with serum proteins or cell membrane receptors and therefore also the toxicity and gene expression [197].

This directly leads to the question if the mechanism of Fe reduction depends on the particle or aggregate size and surface properties of the respective Fe oxides. For *Geobacter sulfurreducens* 111 putative c-type cytochromes were identified and led to the suggestion of multiple electron transport pathways [2]. The production of electrically conductive pili (“nanowires”) but also electron hopping between single cells in a *G. sulfurreducens* biofilm to an electrode were discussed [198]. An interesting question is if different cytochromes are involved if *G. sulfurreducens* is exposed to large ferrihydrite aggregates (>1 µm), highly bioavailable colloids (100-200 nm), or single crystallites with a low reactivity, or how *Geobacter* biofilms adapt to changes in particle structure.

The results of this thesis are also of use for novel remediation technologies as it is under development by the Nanosan-Project. Here, Fe oxide nanoparticles are planned to be injected into a highly BTEX-contaminated aquifer to stimulate microbial Fe oxide reduction and therefore the oxidation of organic contaminants. The choice of appropriate nanoparticles is of decisive importance for the success of the remediation procedure. Nanoparticles with a low aggregation state do not have the potential to enhance microbial Fe oxide reduction. Furthermore their low reactivity would prevent possible synergistic effects with substances present in the aquifer. However, more reactive ferrihydrite colloids possibly coated with humic substances to enhance their colloidal stability under groundwater conditions are more promising. The thesis also demonstrates the large range of reactivities of pure synthetic ferrihydrite and how such an “artificial” reactivity increases under slightly more “natural” conditions. Increasing the complexity of the system only by adding one substance (citrate) increases the reactivity of ferrihydrite drastically. It was already shown that natural ferrihydrite colloids exceed synthetic ferrihydrite reactivities [9]. This rises the question whether the reactivity and the turnover of natural Fe oxides is significantly underestimated until now.

Synthesis of impurity-bearing ferrihydrites as they occur in nature and the observation of reactions of synthetic ferrihydrite colloids under environmentally relevant conditions could be essential to improve the understanding on the fate of Fe oxides in soils and aquifers. This would also improve the application of Fe oxides in natural remediation technologies. Follow-up projects could pick out the adsorption of BTEX compounds or metabolites onto ferrihydrite surfaces as a central theme. The question is whether those substances have the potential to stabilize colloids from larger aggregates in a similar way as citrate does. In case that the electrostatic stabilization mechanism is valid also for BTEX compounds the injection of colloids to a contaminated aquifer

could potentially induce a self-sustaining process. Enhanced microbial reduction may affect also Fe oxides of the aquifer or soil matrix, leading to a certain destruction of aggregates present in the porous medium. Additional electrostatic repulsive forces lead than possibly to colloid stabilization from soil aggregates.

Synthesis of ferrihydrite colloids under more environmentally relevant conditions would include the coprecipitation of ferrihydrite with natural organic matter or different salts and a combination of both. The synthesis of ferrihydrite in a microbial medium (containing different salts and vitamins) in the presence of not Fe-reducing microorganisms is conceivable. The incorporation of these substances and microbial cells or cell debris probably leads to distorted crystal structures and a lower crystallinity. Structural characterization of changed crystal properties and the determination of changing microbial reduction rates would provide new insights into the understanding of the high reactivities of natural Fe oxides. Furthermore, incorporation of cations into the crystal lattice probably has a huge impact on the aggregation state of ferrihydrite. Experiments with those ferrihydrites have the potential to support or to refute the hypothesis, based on the outcomes of the present thesis, that the aggregation state of ferrihydrite triggers its reactivity.

The use of natural organic matter for coprecipitation or adsorption experiments with ferrihydrite is important for the evaluation of electron shuttling substances in the environment. Reduction of those coprecipitates by an Fe-reducing strain may show if natural organic matter, containing e.g. lignin, fatty acids, cellulose and hemicellulose, has the potential to shuttle electrons between Fe reducing microorganisms and Fe oxides, similar to humic acids. Doubts about the environmental relevance of shuttling processes by humic acids are justified because these substances are only extracts of natural organic matter under strong alkaline conditions and probably do not exist in nature.

Results of the present thesis gave indications that adsorption of  $\text{Fe}^{2+}$  onto ferrihydrite surfaces led to recrystallization and therefore to higher bioavailability of ferrihydrite. Further experiments can prove if such a process is really taking place. Incubation of ferrihydrite with an Fe(II) salt in a sterile microbial medium and subsequent determination of the mineralogy and crystallinity may show if  $\text{Fe}^{2+}$  really triggers recrystallization processes in this special case. Furthermore, the impact of possible new Fe oxide phases on microbial accessibility can be determined.

Overall, this thesis provided deeper and novel sights into the reactivity of Fe oxides. It turned out that the surface structure of ferrihydrite is a key factor for its solubility and microbial bioavailability. Furthermore, this work provides an extended mechanism for ligand-induced dissolution of ferrihydrite, including a colloid stabilization step via electrostatic stabilization,

which plays a significant role in microbial Fe oxide reduction. Thereby, the study opens a new perspective of nanoparticle reactivity in general and facilitates new approaches for investigations.

## References

- [1] Waychunas GA, Kim CS, Banfield JF. Nanoparticulate iron oxide minerals in soils and sediments: unique properties and contaminant scavenging mechanisms. *J. Nanopart. Res.* 2005; 7: 409-433.
- [2] Weber KA, Achenbach LA, Coates JD. Microorganisms pumping iron: anaerobic microbial iron oxidation and reduction. *Nat. Rev. Microbiol.* 2006; 4: 752-764.
- [3] Navrotsky A, Mazeina L, Majzlan J. Size-driven structural and thermodynamic complexity in iron oxides. *Science* 2008; 319: 1635-1638.
- [4] Hochella MF, Lower SK, Maurice PA, Penn RL, Sahai N, Sparks DL, Twining BS. Nanominerals, mineral nanoparticles, and Earth systems. *Science* 2008; 319: 1631-1635.
- [5] Christian P, von der Kammer F, Baalousha M, Hofmann T. Nanoparticles: structure, properties, preparation and behaviour in environmental media. *Ecotoxicology* 2008; 17: 326-343.
- [6] Derjaguin B, Landau L. Theory of the stability of strongly charged lyophobic sols and of the adhesion of strongly charged particles in solutions of electrolytes. *Acta Physico Chemica* 1941; 14: 633.
- [7] Verwey E JW, Overbeek J TG. Theory of the stability of lyophobic colloids. Elsevier 1948.
- [8] Vodyanitskii YN. Iron hydroxides in soils: a review of publications. *Eurasian Soil. Sci.* 2010; 43: 1244-1254.
- [9] Fritzsche A, Bosch J, Rennert T, Heister K, Braunschweig J, Meckenstock RU, Totsche KU. Fast microbial reduction of ferrihydrite colloids from a soil effluent. *Geochim. Cosmochim. Acta* 2012; 77: 444-456.
- [10] Aiken GR, Hsu-Kim H, Ryan JN. Influence of dissolved organic matter on the environmental fate of metals, nanoparticles, and colloids. *Environ. Sci. Technol.* 2011; 45: 3196-3201.
- [11] Wiesner MR, Lowry GV, Casman E, Bertsch PM, Matson CW, Di Giulio RT, Liu J, Hochella MF. Meditations on the ubiquity and mutability of nano-sized materials in the environment. *ACS Nano* 2011; 5: 8466-8470.
- [12] Hochella MF. Nanogeoscience: from origins to cutting-edge applications. *Elements* 2008; 4: 373-379.
- [13] van der Zee C, Slomp CP, Rancourt DG, de Lange GJ, van Raaphorst WA. A Mössbauer spectroscopic study of the iron redox transition in eastern Mediterranean sediments. *Geochim. Cosmochim. Acta* 2005; 69: 441-453.
- [14] Ryan JN, Elimelech M. Colloid mobilization and transport in groundwater. *Colloids Surf.* 1996; 107: 1-56.
- [15] Banfield JF, Zhang HZ, in: *Nanoparticles and the Environment*, Mineralogical Soc. America: Washington, 2001; Vol. 44, pp 1-58.
- [16] Gilbert B, Banfield JF. Molecular-scale processes involving nanoparticulate minerals in biogeochemical systems. *Rev. Mineral. Geochem.* 2005; 59: 109-155.

- [17] Bosch J, Lee K-Y, Jordan G, Kim K-W, Meckenstock RU. Anaerobic, nitrate-dependent oxidation of pyrite nanoparticles by *Thiobacillus denitrificans*. Environ. Sci. Technol. 2012; 46: 2095-2101.
- [18] Madden AS, Hochella MF. A test of geochemical reactivity as a function of mineral size: manganese oxidation promoted by hematite nanoparticles. Geochim. Cosmochim. Acta 2005; 69: 389-398.
- [19] Bonneville S, Behrends T, Van Cappellen P. Solubility and dissimilatory reduction kinetics of iron(III) oxyhydroxides: a linear free energy relationship. Geochim. Cosmochim. Acta 2009; 73: 5273-5282.
- [20] Bonneville S, van Cappellen P, Behrends T. Microbial reduction of iron(III) oxyhydroxides: effects of mineral solubility and availability. Chem. Geol. 2004; 212: 255-268.
- [21] Larsen O, Postma D. Kinetics of reductive bulk dissolution of lepidocrocite, ferrihydrite and goethite. Geochim. Cosmochim. Acta 2001; 65: 1367-1379.
- [22] Echigo T, Aruguete DM, Murayama M, Hochella Jr MF. Influence of size, morphology, surface structure, and aggregation state on reductive dissolution of hematite nanoparticles with ascorbic acid. Geochim. Cosmochim. Acta 2012; 90: 149-162.
- [23] Tang RK, Wang LJ, Nancollas GH. Size-effects in the dissolution of hydroxyapatite: an understanding of biological demineralization. J. Mater. Chem. 2004; 14: 2341-2346.
- [24] Wigginton NS, Haus KL, Hochella MF, Jr. Aquatic environmental nanoparticles. J. Environ. Monitor. 2007; 9: 1306-1316.
- [25] Roden EE. Fe(III) oxide reactivity toward biological versus chemical reduction. Environ. Sci. Technol. 2003; 37: 1319-1324.
- [26] Lanzl CA, Baltrusaitis J, Cwiertny DM. Dissolution of hematite nanoparticle aggregates: influence of primary particle size, dissolution mechanism, and solution pH. Langmuir 2012; 28: 15797-15808.
- [27] Cismasu AC, Michel FM, Tcaciuc AP, Tyliszczak T, Brown Jr GE. Composition and structural aspects of naturally occurring ferrihydrite. CR Geosci. 2011; 343: 210-218.
- [28] Delay M, Frimmel FH. Nanoparticles in aquatic systems. Anal. Bioanal. Chem. 2012; 402: 583-592.
- [29] Yan B, Wrenn BA, Basak S, Biswas P, Giammar DE. Microbial reduction of Fe(III) in hematite nanoparticles by *Geobacter sulfurreducens*. Environ. Sci. Technol. 2008; 42: 6526-6531.
- [30] Bonneville S, Behrends T, van Cappellen P, Hyacinthe C, Röling WFM. Reduction of Fe(III) colloids by *Shewanella putrefaciens*: a kinetic model. Geochim. Cosmochim. Acta 2006; 70: 5842-5854.
- [31] Bose S, Hochella Jr MF, Gorby YA, Kennedy DW, McCready DE, Madden AS, Lower BH. Bioreduction of hematite nanoparticles by the dissimilatory iron reducing bacterium *Shewanella oneidensis* MR-1. Geochim. Cosmochim. Acta 2009; 73: 962-976.



- [32] Bosch J, Fritzsche A, Totsche KU, Meckenstock RU. Nanosized ferrihydrite colloids facilitate microbial iron reduction under flow conditions. *Geomicrobiol. J.* 2010; 27: 1-7.
- [33] Bosch J, Heister K, Hofmann T, Meckenstock RU. Nanosized iron oxide colloids strongly enhance microbial iron reduction. *Appl. Environ. Microbiol.* 2010; 76: 184-189.
- [34] Kato S, Nakamura R, Kai F, Hashimoto K. Respiratory interactions of soil bacteria with (semi)conductive iron oxide minerals. *Environ. Microbiol.* 2010; 12: 3114-3123.
- [35] Kato S, Hashimoto K, Watanabe K. Microbial interspecies electron transfer via electric currents through conductive minerals. *Proc. Natl. Acad. Sci. USA* 2012; 109: 10042-10046.
- [36] Lalonde K, Mucci A, Oullet A, Gélinas Y. Preservation of organic matter in sediments promoted by iron. *Nature Lett.* 2012; 483: 198-200.
- [37] Djajadi, Abbott LK, Hinz C. Synergistic impacts of clay and organic matter on structural and biological properties of a sandy soil. *Geoderma* 2012; 183: 19-24.
- [38] Kaiser M, Ellerbrock RH, Wulf M, Dultz S, Hierath C, Sommer M. The influence of mineral characteristics on organic matter content, composition, and stability of topsoils under long-term arable and forest land use. *J. Geophys. Res.-Biogeo.* 2012; 117.
- [39] Coates JD, Ellis DJ, Blunt-Harris EL, Gaw CV, Roden EE, Lovley DR. Recovery of humic-reducing bacteria from a diversity of environments. *Appl. Environ. Microbiol.* 1998; 64: 1504-1509.
- [40] Lovley DR, Blunt-Harris EL. Role of humic-bound iron as electron transfer agent in dissimilatory Fe(III) reduction. *Appl. Environ. Microbiol.* 1999; 65: 4252-4254.
- [41] Lovley DR, Coates JD, Blunt-Harris EL, Phillips EJP, Woodward JC. Humic substances as electron acceptors for microbial respiration. *Nature* 1996; 382: 445-448.
- [42] Roden EE, Kappler A, Bauer I, Jiang J, Paul A, Stoesser R, Konishi H, Xu HF. Extracellular electron transfer through microbial reduction of solid-phase humic substances. *Nat. Geosci.* 2010; 3: 417-421.
- [43] Chen J, Gu B, Royer RA, Burgos WD. The roles of natural organic matter in chemical and microbial reduction of ferric iron. *Sci. Total Environ.* 2003; 307: 167-178.
- [44] Jiang J, Kappler A. Kinetics of microbial and chemical reduction of humic substances: implications for electron shuttling. *Environ. Sci. Technol.* 2008; 42: 3563-3569.
- [45] Wolf M, Kappler A, Jiang J, Meckenstock RU. Effects of humic substances and quinones at low concentrations on ferrihydrite reduction by *Geobacter metallireducens*. *Environ. Sci. Technol.* 2009; 43: 5679-5685.
- [46] Buffle J, Wilkinson KJ, Stoll S, Filella M, Zhang JW. A generalized description of aquatic colloidal interactions: the three-colloidal component approach. *Environ. Sci. Technol.* 1998; 32: 2887-2899.

- [47] Wilkinson KJ, Negre JC, Buffle J. Coagulation of colloidal material in surface waters: the role of natural organic matter. *J. Contam. Hydrol.* 1997; 26: 229-243.
- [48] Baalousha M. Aggregation and disaggregation of iron oxide nanoparticles: influence of particle concentration, pH and natural organic matter. *Sci Total Environ* 2009; 407: 2093-2101.
- [49] Moedl C, Woermann H, Amelung W. Contrasting effects of different types of organic material on surface area and microaggregation of goethite. *Geoderma* 2007; 141: 167-173.
- [50] Perret D, Gaillard JF, Dominik J, Atteia O. The diversity of natural hydrous iron oxides. *Environ. Sci. Technol.* 2000; 34: 3540-3546.
- [51] Gunnars A, Blomqvist S, Johansson P, Andersson C. Formation of Fe(III) oxyhydroxide colloids in freshwater and brackish seawater, with incorporation of phosphate and calcium. *Geochim. Cosmochim. Acta* 2002; 66: 745-758.
- [52] Hiemstra T, Antelo J, Rahnemaie R, Riemsdijk WHv. Nanoparticles in natural systems I: the effective reactive surface area of the natural oxide fraction in field samples. *Geochim. Cosmochim. Acta* 2010; 74: 41-58.
- [53] Rose J, Vilge A, Olivie-Lauquet G, Masion A, Frechou C, Bottero J-Y. Iron speciation in natural organic matter colloids. *Colloid. Surface. A* 1998; 136: 11-19.
- [54] Gaffney JW, White KN, Boulton S. Oxidation state and size of Fe controlled by organic matter in natural waters. *Environ. Sci. Technol.* 2008; 42: 3575-3581.
- [55] Mikutta C. X-ray absorption spectroscopy study on the effect of hydrobenzoic acids on the formation and structure of ferrihydrite. *Geochim. Cosmochim. Acta* 2011; 75: 5122-5139.
- [56] Lofts S, Tipping E, Hamilton-Taylor J. The chemical speciation of Fe(III) in freshwaters. *Aquat. Geochem.* 2008; 14: 337-358.
- [57] Mikutta C, Mikutta R, Bonneville S, Wagner F, Voegelin A, Christl I, Kretzschmar R. Synthetic coprecipitates of exopolysaccharides and ferrihydrite. Part I: characterization. *Geochim. Cosmochim. Acta* 2008; 72: 1111-1127.
- [58] Eusterhues K, Wagner FE, Häusler W, Hanzlik M, Knicker H, Totsche KU, Kögel-Knabner I, Schwertmann U. Characterization of ferrihydrite-soil organic matter coprecipitates by X-ray diffraction and Mössbauer spectroscopy. *Environ. Sci. Technol.* 2008; 42: 7891-7897.
- [59] Lovley DR, Woodward JC. Mechanisms for chelator stimulation of microbial Fe(III)-oxide reduction. *Chem. Geol.* 1996; 132: 19-24.
- [60] Pédrot M, Le Boudec A, Davranche M, Dia A, Henin O. How does organic matter constrain the nature, size and availability of Fe nanoparticles for biological reduction. *J. Colloid Interface Sci.* 2011; 359: 75-85.
- [61] Lovley DR, Woodward JC, Chapelle FH. Stimulated anoxic biodegradation of aromatic hydrocarbons using Fe(III) ligands. *Nature* 1994; 370: 128-31.

- [62] Cismasu AC, Michel FM, Stebbins JF, Levard C, Brown Jr GE. Properties of impurity-bearing ferrihydrite I. Effects of Al content and precipitation rate on the structure of 2-line ferrihydrite. *Geochim. Cosmochim. Acta* 2012; 92: 275-291.
- [63] Mikutta C, Kretzschmar R. Synthetic coprecipitates of exopolysaccharides and ferrihydrite. Part II: siderophore-promoted dissolution. *Geochim. Cosmochim. Acta* 2008; 72: 1128-1142.
- [64] Urrutia MM, Roden EE, Zachara JM. Influence of aqueous and solid-phase Fe(II) complexants on microbial reduction of crystalline iron(III) oxides. *Environ. Sci. Technol.* 1999; 33: 4022-4028.
- [65] Waite TD, Morel FM. Photoreductive dissolution of colloidal iron oxides in natural waters. *Environ. Sci. Technol.* 1984; 18: 860-8.
- [66] Rubasinghe G, Kyei PK, Scherer MM, Grassian VH. Proton-promoted dissolution of  $\alpha$ -FeOOH nanorods and microrods: size dependence, anion effects (carbonate and phosphate), aggregation and surface adsorption. *J. Colloid Interface Sci.* 2012; 385: 15-23.
- [67] Sobolev D, Roden EE. Evidence for rapid microscale bacterial redox cycling of iron in circumneutral environments. *Anton. Leeuw. Int. J. G.* 2002; 81: 587-597.
- [68] Roden EE, Sobolev D, Glazer B, Luther GW. Potential for microscale bacterial Fe redox cycling at the aerobic-anaerobic interface. *Geomicrobiol. J.* 2004; 21: 379-391.
- [69] Pierson BK, Parenteau MN, Griffin BM. Phototrophs in high-iron-concentration microbial mats: physiological ecology of phototrophs in an iron-depositing hot spring. *Appl. Environ. Microbiol.* 1999; 65: 5474-5483.
- [70] Kashefi K, Holmes DE, Baross JA, Lovley DR. Thermophily in the *Geobacteraceae*: *Geothermobacter ehrlichii* gen. nov., sp nov., a novel thermophilic member of the *Geobacteraceae* from the "Bag city" hydrothermal vent. *Appl. Environ. Microbiol.* 2003; 69: 2985-2993.
- [71] Peine A, Tritschler A, Kusel K, Peiffer S. Electron flow in an iron-rich acidic sediment - evidence for an acidity-driven iron cycle. *Limnol. Oceanogr.* 2000; 45: 1077-1087.
- [72] Emerson D, Revsbech NP. Investigation of an iron-oxidizing microbial mat community located near Aarhus, Denmark: field studies. *Appl. Environ. Microbiol.* 1994; 60: 4022-31.
- [73] Emerson D, Weiss JV, Magonigal JP. Iron-oxidizing bacteria are associated with ferric hydroxide precipitates (Fe-plaque) on the roots of wetland plants. *Appl. Environ. Microbiol.* 1999; 65: 2758-2761.
- [74] Bloethe M, Roden EE. Microbial iron redox cycling in a circumneutral-pH groundwater seep. *Appl. Environ. Microbiol.* 2009; 75: 468-473.
- [75] Weber KA. Anaerobic redox cycling of iron by freshwater sediment microorganisms. *Environ. Microbiol.* 2006; 8: 100-113.
- [76] Coby AJ, Picardal F, Shelobolina E, Xu H, Roden EE. Repeated anaerobic microbial redox cycling of iron. *Appl. Environ. Microbiol.* 2011; 77: 6036-6042.

- [77] Schieber J, Glamoclija M, *Microbial mats built by iron bacteria: a modern example from southern Indiana*. Elsevier: Amsterdam, 2007; p 233-244.
- [78] Roden EE, McBeth JM, Blothe M, Percak-Dennett EM, Fleming EJ, Holyoke RR, Luther GW, 3rd, Emerson D, Schieber J. The microbial ferrous wheel in a neutral pH groundwater seep. *Front. Microbiol.* 2012; 3: 172-172.
- [79] Pokrovsky OS, Dupré B, Schott J. Fe-Al-organic colloids control of trace elements in peat soil solutions: results of ultrafiltration and dialysis. *Aquat. Geochem.* 2005; 11: 241-278.
- [80] Pédrot M, Dia A, Davranche M, Bouhnik-Le Coz M, Henin O, Gruau G. Insights into colloid-mediated trace element release at the soil/water interface. *J. Colloid Interface Sci.* 2008; 325: 187-197.
- [81] Hassellöv M, v. d. Kammer F. Iron oxides as geochemical nanovectors for metal transport in soil-river systems. *Elements* 2008; 4: 401-406.
- [82] Jun Y-S, Lee B, Waychunas GA. In situ observations of nanoparticle early development kinetics at mineral-water interfaces. *Environ. Sci. Technol.* 2010; 44: 8182-8189.
- [83] Yu C, Gao B, Munoz-Carpena R, Tian Y, Wu L, Perez-Ovilla O. A laboratory study of colloid and solute transport in surface runoff on saturated soil. *J. Hydrol.* 2011; 402: 159-164.
- [84] Kretzschmar R, Sticher H. Transport of humic-coated iron oxide colloids in a sandy soil: influence of Ca<sup>2+</sup> and trace metals. *Environ. Sci. Technol.* 1997; 31: 3497-3504.
- [85] Seaman JC, Bertsch PM, Strom RN. Characterization of colloids mobilized from southeastern coastal plain sediments. *Environ. Sci. Technol.* 1997; 31: 2782-2790.
- [86] Petosa AR, Brennan SJ, Rajput F, Tufenkji N. Transport of two metal oxide nanoparticles in saturated granular porous media: role of water chemistry and particle coating. *Water Res.* 2012; 46: 1273-1285.
- [87] Morales VL, Zhang W, Gao B, Lion LW, Bisogni JJ, Jr., McDonough BA, Steenhuis TS. Impact of dissolved organic matter on colloid transport in the vadose zone: deterministic approximation of transport deposition coefficients from polymeric coating characteristics. *Water Res.* 2011; 45: 1691-1701.
- [88] Bin G, Cao X, Dong Y, Luo Y, Ma LQ. Colloid deposition and release in soils and their association with heavy metals. *Crit. Rev. Env. Sci. Tec.* 2011; 41: 336-372.
- [89] van de Weerd H, Leijnse A. Assessment of the effect of kinetics on colloid facilitated radionuclide transport in porous media. *J. Contam. Hydrol.* 1997; 26: 245-256.
- [90] Baik MH, Hahn PS. Radionuclide transport facilitated by polydispersed pseudo-colloids in the fractured rock media. *J. Nucl. Sci. Technol.* 1997; 34: 41-49.
- [91] Schaefer T, Huber F, Seher H, Missana T, Alonso U, Kumke M, Eidner S, Claret F, Enzmann F. Nanoparticles and their influence on radionuclide mobility in deep geological formations. *Appl. Geochem.* 2012; 27: 390-403.

- [92] Bao Q, Lin Q, Tian G, Wang G, Yu J, Peng G. Copper distribution in water-dispersible colloids of swine manure and its transport through quartz sand. *J. Hazard. Mater.* 2011; 186: 1660-1666.
- [93] Regelin IC, Weng L, van Riemsdijk WH. The contribution of organic and mineral colloidal nanoparticles to element transport in a podzol soil. *Appl. Geochem.* 2011; 26: S241-S244.
- [94] Kuznar ZA, Elimelech M. Direct microscopic observation of particle deposition in porous media: role of the secondary energy minimum. *Colloid. Surface. A* 2007; 294: 156-162.
- [95] Loux NT, Savage N. An assessment of the fate of metal oxide nanomaterials in porous media. *Water Air Soil Pollut.* 2008; 194: 227-241.
- [96] Loux NT. Simulating the stability of colloidal amorphous iron oxide in natural water. *Water Air Soil Pollut.* 2011; 217: 157-172.
- [97] Johnson WP, Pazmino E, Ma H. Direct observations of colloid retention in granular media in the presence of energy barriers, and implications for inferred mechanisms from indirect observations. *Water Res.* 2010; 44: 1158-1169.
- [98] Bradford SA, Yates SR, Bettahar M, Simunek J. Physical factors affecting the transport and fate of colloids in saturated porous media. *Water Resour. Res.* 2002; 38: 63.1-63.12.
- [99] Ko C-H, Elimelech M. The "shadow effect" in colloid transport and deposition dynamics in granular porous media: measurements and mechanisms. *Environ. Sci. Technol.* 2000; 34: 3681-3689.
- [100] Chen G, Flury M, Harsh JB, Lichtner PC. Colloid-facilitated transport of cesium in variably saturated Hanford sediments. *Environ. Sci. Technol.* 2005; 39: 3435-3442.
- [101] Tosco T, Bosch J, Meckenstock RU, Sethi R. Transport of ferrihydrite nanoparticles in saturated porous media: role of ionic strength and flow rate. *Environ. Sci. Technol.* 2012; 46: 4008-4015.
- [102] Mylon SE, Chen KL, Elimelech M. Influence of natural organic matter and ionic composition on the kinetics and structure of hematite colloid aggregation: implications to iron depletion in estuaries. *Langmuir* 2004; 20: 9000-9006.
- [103] Sander S, Mosley LM, Hunter KA. Investigation of interparticle forces in natural waters: effects of adsorbed humic acids on iron oxide and alumina surface properties. *Environ. Sci. Technol.* 2004; 38: 4791-4796.
- [104] EEA *Progress in management of contaminated sites. Report CSI 015*; European Environmental Agency: Copenhagen, Denmark, 2007.
- [105] Xu P, Zeng GM, Huang DL, Feng CL, Hu S, Zhao MH, Lai C, Wei Z, Huang C, Xie GX, Liu ZF. Use of iron oxide nanomaterials in wastewater treatment: a review. *Sci. Total Environ.* 2012; 424: 1-10.
- [106] Cundy AB, Hopkinson L, Whitby RLD. Use of iron-based technologies in contaminated land and groundwater remediation: a review. *Sci. Total Environ.* 2008; 400: 42-51.

- [107] Scherer MM, Richter S, Valentine RL, Alvarez PJJ. Chemistry and microbiology of permeable reactive barriers for *in situ* groundwater clean up. Environ. Sci. Technol. 2000; 30: 363-411.
- [108] Borch T, Kretzschmar R, Kappler A, van Cappellen P, Ginder-Vogel M, Voegelin A, Campbell K. Biogeochemical redox processes and their impact on contaminant dynamics. Environ. Sci. Technol. 2010; 44: 15-23.
- [109] Elsner M, Haderlein SB, Kellerhals T, Luzi S, Zwank L, Angst W, Schwarzenbach RP. Mechanisms and products of surface-mediated reductive dehalogenation of carbon tetrachloride by Fe(II) on goethite. Environ. Sci. Technol. 2004; 38: 2058-2066.
- [110] Elsner M, Schwarzenbach RP, Haderlein SB. Reactivity of Fe(II)-bearing minerals toward reductive transformation of organic contaminants. Environ. Sci. Technol. 2004; 38: 799-807.
- [111] Heijman CG, Holliger C, Glaus MA, Schwarzenbach RP, Zeyer J. Abiotic reduction of 4-chloronitrobenzene to 4-chloroaniline in a dissimilatory iron-reducing enrichment culture. Appl. Environ. Microbiol. 1993; 59: 4350-3.
- [112] Borch T, Inskeep WP, Harwood JA, Gerlach R. Impact of ferrihydrite and anthraquinone-2,6-disulfonate on the reductive transformation of 2,4,6-trinitrotoluene by a gram-positive fermenting bacterium. Environ. Sci. Technol. 2005; 39: 7126-7133.
- [113] Amonette JE, Workman DJ, Kennedy DW, Fruchter JS, Gorby YA. Dechlorination of carbon tetrachloride by Fe(II) associated with goethite. Environ. Sci. Technol. 2000; 34: 4606-4613.
- [114] Hakala JA, Chin Y-P, Weber EJ. Influence of dissolved organic matter and Fe(II) on the abiotic reduction of pentachloronitrobenzene. Environ. Sci. Technol. 2007; 41: 7337-7342.
- [115] Vikesland PJ, Valentine RL. Iron oxide surface-catalyzed oxidation of ferrous iron by monochloramine: implications of oxide type and carbonate on reactivity. Environ. Sci. Technol. 2002; 36: 512-519.
- [116] Colon D, Weber EJ, Anderson JL. QSAR study of the reduction of nitroaromatics by Fe(II) species. Environ. Sci. Technol. 2006; 40: 4976-4982.
- [117] Cwiertny DM, Handler RM, Schaefer MV, Grassian VH, Scherer MM. Interpreting nanoscale size-effects in aggregated Fe-oxide suspensions: reaction of Fe(II) with goethite. Geochim. Cosmochim. Acta 2008; 72: 1365-1380.
- [118] McCormick ML, Bouwer EJ, Adriaens P. Carbon tetrachloride transformation in a model iron-reducing culture: relative kinetics of biotic and abiotic reactions. Environ. Sci. Technol. 2002; 36: 403-410.
- [119] Tobler NB, Hofstetter TB, Straub KL, Fontana D, Schwarzenbach RP. Iron-mediated microbial oxidation and abiotic reduction of organic contaminants under anoxic conditions. Environ. Sci. Technol. 2007; 41: 7765-7772.
- [120] Smedley PL, Kinniburgh DG. A review of the source, behaviour and distribution of arsenic in natural waters. Appl. Geochem. 2002; 17: 517-568.
- [121] Yuan T, Hu JY, Ong SL, Luo QF, Ng WJ. Arsenic removal from household drinking water by adsorption. J. Environ. Sci. Heal. A 2002; 37: 1721-1736.

- [122] Mohan D, Pittman CU, Jr. Arsenic removal from water/wastewater using adsorbents - a critical review. *J. Hazard. Mater.* 2007; 142: 1-53.
- [123] Fritzsche A, Rennert T, Totsche KU. Arsenic strongly associates with ferrihydrite colloids formed in a soil effluent. *Environ. Pollut.* 2011; 159: 1398-1405.
- [124] Hu H, Wang Z, Pan L. Synthesis of monodisperse Fe<sub>3</sub>O<sub>4</sub>@silica core-shell microspheres and their application for removal of heavy metal ions from water. *J. Alloy. Compd.* 2010; 492: 656-661.
- [125] Ozmen M, Can K, Arslan G, Tor A, Cengeloglu Y, Ersoz M. Adsorption of Cu(II) from aqueous solution by using modified Fe<sub>3</sub>O<sub>4</sub> magnetic nanoparticles. *Desalination* 2010; 254: 162-169.
- [126] Gilbert B, Ono RK, Ching KA, Kim CS. The effects of nanoparticle aggregation processes on aggregate structure and metal uptake. *J. Colloid Interface Sci.* 2009; 339: 285-295.
- [127] Caccavo F, Lonergan DJ, Lovley DR, Davis M, Stolz JF, McInerney MJ. *Geobacter sulfurreducens* sp. nov., a hydrogen- and acetate oxidizing dissimilatory metal-reducing microorganism. *Appl. Environ. Microbiol.* 1994; 60: 3752-3759.
- [128] Widdel F, Bak F, in: *The Prokaryotes*, Balows A, Trüper HG, Dworkin M, Harder W, Schleifer KH, (Eds.) Springer-Verlag: New York, 1992; pp 3352-3378.
- [129] Widdel F, Hansen TA, in: *The Prokaryotes*, Balows A, Trüper HG, Dworkin M, Harder W, Schleifer KH, (Eds.) Springer-Verlag: Berlin, 1992; pp 583-624.
- [130] Widdel F, Kohring GW, Mayer F. Studies in dissimilatory sulfate-reducing bacteria that decompose fatty acids. III. Characterization of the filamentous gliding *Desulfonema limicola* ge. nov. sp. nov., and *Desulfonema magnum* sp. nov. *Arch. Microbiol.* 1983; 134: 286-294.
- [131] Widdel F, Pfennig N. Studies in dissimilatory sulfate-reducing bacteria that decompose fatty acids. III. Isolation of a new sulfate-reducer enriched with acetate from saline environments. Description of *Desulfobacter postgatei* gen. nov. sp. nov. *Arch. Microbiol.* 1981; 129: 395-400.
- [132] Lovley DR, Phillips BL. Organic matter mineralization with reduction of ferric iron in anaerobic sediments. *Appl. Environ. Microbiol.* 1986; 51: 683-689.
- [133] Conrad R, Klose M, Claus P. Phosphate inhibits acetotrophic methanogenesis on rice roots. *Appl. Environ. Microbiol.* 2000; 66: 828-831.
- [134] Cornell RM, Schwertmann U. The iron oxides. Structure, properties, reactions, occurrences and uses. 2 ed. Weinheim: Wiley-VCH Verlag GmbH & Co.KGaA; 2003.
- [135] Smith SJ, Page K, Kim H, Campbell BJ, Boerio-Goates J, Woodfield BF. Novel synthesis and structural analysis of ferrihydrite. *Inorg. Chem.* 2012; 51: 6421-6424.
- [136] Cornell RM, Schwertmann U. Iron oxides in the laboratory. Preparation and characterization. 2 ed. Weinheim: Wiley-VCH; 2000.

- [137] Anschutz AJ, Penn RL. Reduction of crystalline iron(III) oxyhydroxides using hydroquinone: influence of phase and particle size. *Geochem. Trans.* 2005; 6: 60-66.
- [138] JCPDS. Mineral powder diffraction file data book. International Centre for Diffraction Data; 2001.
- [139] Downs RT, Hall-Wallace M. The american mineralogist crystal structure database. *Am. Mineral.* 2003; 88: 247-250.
- [140] Brunauer S, Emmett PH, Teller E. Adsorption of gases in multimolecular layers. *J. Am. Chem. Soc.* 1938; 60: 309-319.
- [141] de Boer JH, Lippens BC, Linsen BG, Broekhoff JCP, van den Heuvel A, Osinga TJ. The *t*-curve of multimolecular N<sub>2</sub>-adsorption. *J. Colloid Interface Sci.* 1966; 21: 405-414.
- [142] Harris DC. Quantitative Chemical Analysis. Heidelberg: Springer; 2002.
- [143] Stookey LL. Ferrozine - a new spectrophotometric reagent for iron. *Anal. Chem.* 1970; 42: 779-781.
- [144] Braunschweig J, Bosch J, Heister K, Kuebeck C, Meckenstock RU. Reevaluation of colorimetric iron determination methods commonly used in geomicrobiology. *J. Microbiol. Methods* 2012; 89: 41-48.
- [145] Hausner DB, Bhandari N, Pierre-Louis A-M, Kubicki JD, Strongin DR. Ferrihydrite reactivity toward carbon dioxide. *J. Colloid Interface Sci.* 2009; 337: 492-500.
- [146] Wulandari P, Li XH, Tamada K, Hara M. Conformational study of citrates adsorbed on gold nanoparticles using Fourier transform infrared spectroscopy. *J. Nonlinear Opt. Phys.* 2008; 17: 185-192.
- [147] Mohapatra M, Mohapatra L, Anand S, Mishra BK. One-pot synthesis of high surface area nano-akaganeite powder and its cation sorption behavior. *J. Chem. Eng. Data* 2010; 55: 1486-1491.
- [148] Music S, Krehula S, Popovic S. Thermal decomposition of  $\beta$ -FeOOH. *Mater. Lett.* 2004; 58: 444-448.
- [149] Fang L, Cao Y, Huang Q, Walker SL, Cai P. Reactions between bacterial exopolymers and goethite: a combined macroscopic and spectroscopic investigation. *Water Res.* 2012; 46: 5613-5620.
- [150] Naumkin AV, Kraut-Vass A, Gaarenstroom SW, Powell CJ. NIST X-ray Photoelectron Spectroscopy Database, 4.1, National Institute of Standards and Technology, Gaithersburg 2012, <http://srdata.nist.gov/xps/>, Dec. 20, 2012
- [151] McIntyre NS, Zetaruk DG. X-ray photoelectron spectroscopic studies of iron oxides. *Anal. Chem.* 1977; 49: 1521-1529.
- [152] Pratt AR, Muir IJ, Nesbitt HW. X-ray photoelectron and Auger electron spectroscopic studies of pyrrhotite and mechanism of air oxidation. *Geochim. Cosmochim. Acta* 1994; 58: 827-841.



- [153] Anastácio AS, Harris B, Yoo H-I, Fabris JD, Stucki JW. Limitations of the ferrozine method for quantitative assay of mineral systems for ferrous and total iron. *Geochim. Cosmochim. Acta* 2008; 72: 5001-5008.
- [154] Ali A-E-E. Ternary complexes of copper(II) and their use in the spectrophotometric determination of copper in alloys and rocks. *Can. J. Chem.* 1993; 71: 1002-1005.
- [155] Evans CH. The spectrophotometric determination of micromolar concentrations of  $\text{Co}^{2+}$  using o-phenanthroline. *Anal. Biochem.* 1983; 135: 335-9.
- [156] Jyothi T, Reddy MLP, Prasada Rao T, Damodaran AD. Liquid-liquid extraction and higher order derivative spectrophotometric determination of cobalt with 1,10-phenanthroline and rose bengal. *Anal. Lett.* 1987; 20: 1729-1749.
- [157] Kompany-Zareh M, Massoumi A. Multicomponent determination of cobalt, copper, and iron with 1,10-phenanthroline by principal component regression modelling of spectrophotometric data. *Fresenius J. Anal. Chem.* 1999; 363: 219-223.
- [158] Mutaftchiev K, Tzachev K, Alexiev A. Spectrophotometric catalytic method for determination of manganese(II) in human blood serum. *Bull. Chem. Technol. Maced.* 1999; 18: 37-40.
- [159] Taylor SW, Luther III GW, Waite JH. Polarographic and spectrophotometric investigation of iron(III) complexation to 3,4-dihydroxyphenylalanine-containing peptides and proteins from *Mytilus edulis*. *Inorg. Chem.* 1994; 33: 5819-5824.
- [160] Chapin TP, Jannasch HW, Johnson KS. In situ osmotic analyzer for the year-long continuous determination of Fe in hydrothermal systems. *Anal. Chim. Acta* 2002; 463: 265-274.
- [161] Millero FJ, Sotolongo S, Izaguirre M. The oxidation kinetics of Fe(II) in seawater. *Geochim. Cosmochim. Acta* 1987; 51: 793-801.
- [162] Sung W, Morgan JJ. Kinetics and product of ferrous iron oxygenation in aqueous systems. *Environ. Sci. Technol.* 1980; 14: 561-568.
- [163] Porsch K, Kappler A.  $\text{Fe}^{\text{II}}$  oxidation by molecular  $\text{O}_2$  during HCl extraction. *Environ. Chem.* 2011; 8: 190-197.
- [164] Schoonen M, Elsetinow A, Borda MS, D. Effect of temperature and illumination on pyrite oxidation between pH 2 and 6. *Geochem. Trans.* 2000; 4.
- [165] Barrón V, Torrent J. Evidence for a simple pathway to maghemite in Earth and Mars soils. *Geochim. Cosmochim. Acta* 2002; 66: 2801-2806.
- [166] Barrón V, Torrent J, de Grave E. Hydromaghemite, an intermediate in the hydrothermal transformation of 2-line ferrihydrite into hematite. *Am. Mineral.* 2003; 88: 1679-1688.
- [167] Michel FM, Barrón V, Torrent J, Morales MP, Serna CJ, Boily J-F, Liu Q, Ambrosini A, Cismasu AC, Brown Jr GE. Ordered ferrimagnetic form of ferrihydrite reveals links among structure, composition and magnetism. *Proc. Natl. Acad. Sci. USA* 2010; 107: 2787-2792.

- [168] Cabello E, Morales MP, Serna CJ, Barrón V, Torrent J. Magnetic enhancement during the crystallization of ferrihydrite at 25 and 50 °C. *Clay. Clay Min.* 2009; 57: 46-53.
- [169] Cornell RM. Comparison and classification of the effects of simple ions and molecules upon the transformation of ferrihydrite into more crystalline products. *Z. Pflanzenernähr. Bodenk.* 1987; 150: 304-307.
- [170] Mudunkotuwa IA, Grassian VH. Citric acid adsorption on TiO<sub>2</sub> nanoparticles in aqueous suspensions at acidic and circumneutral pH: surface coverage, surface speciation, and its impact on nanoparticle-nanoparticle interaction. *J. Am. Chem. Soc.* 2010; 132: 14986-14994.
- [171] Eusterhues K, Rennert T, Knicker H, Koegel-Knabner I, Totsche KU, Schwertmann U. Fractionation of organic matter due to reaction with ferrihydrite: coprecipitation versus adsorption. *Environ. Sci. Technol.* 2011; 45: 527-533.
- [172] Liang L, Hofmann A, Gu B. Ligand-induced dissolution and release of ferrihydrite colloids. *Geochim. Cosmochim. Acta* 2000; 64: 2027-2037.
- [173] Martin RB. Citrate binding of Al<sup>3+</sup> and Fe<sup>3+</sup>. *J. Inorg. Biochem.* 1986; 28: 181-187.
- [174] Furrer G, Stumm W. The coordination chemistry of weathering: I. Dissolution kinetics of  $\alpha$ -Al<sub>2</sub>O<sub>3</sub> and BeO. *Geochim. Cosmochim. Acta* 1986; 50: 1847-1860.
- [175] Kappler A, Benz M, Schink B, Brune A. Electron shuttling via humic acids in microbial iron(III) reduction in a freshwater sediment. *FEMS Microbiol. Ecol.* 2004; 47: 85-92.
- [176] Cutting RS, Coker VS, Fellowes JW, Lloyd JR, Vaughan DJ. Mineralogical and morphological constraints on the reduction of Fe(III) minerals by *Geobacter sulfurreducens*. *Geochim. Cosmochim. Acta* 2009; 73: 4004-4022.
- [177] Raiswell R, Vu HP, Brinza L, Benning LG. The determination of labile Fe in ferrihydrite by ascorbic acid extraction: methodology, dissolution kinetics and loss of solubility with age and de-watering. *Chem. Geol.* 2010; 278: 70-79.
- [178] Roden EE, Zachara JM. Microbial reduction of crystalline iron(III) oxides: influence of oxide surface area and potential for cell growth. *Environ. Sci. Technol.* 1996; 30: 1618-1628.
- [179] Liu H, Wang Y, Ma Y, Wei Y, Pan G. The microstructure of ferrihydrite and its catalytic reactivity. *Chemosphere* 2010; 79: 802-806.
- [180] Foerstendorf H, Heim K, Rossberg A. The complexation of uranium(VI) and atmospherically derived CO<sub>2</sub> at the ferrihydrite-water interface probed by time-resolved vibrational spectroscopy. *J. Colloid Interface Sci.* 2012; 377: 299-306.
- [181] Roden EE. Analysis of long-term bacterial vs. chemical Fe(III) oxide reduction kinetics. *Geochim. Cosmochim. Acta* 2004; 68: 3205-3216.
- [182] Rosso KM, Yanina SV, Gorski CA, Larese-Casanova P, Scherer MM. Connecting observations of hematite ( $\alpha$ -Fe<sub>2</sub>O<sub>3</sub>) growth catalyzed by Fe(II). *Environ. Sci. Technol.* 2010; 44: 61-67.

- [183] Yanina SV, Rosso KM. Linked reactivity at mineral-water interface through bulk crystal conduction. *Science* 2008; 320: 218-222.
- [184] Handler RM, Beard BL, Johnson CM, Scherer MM. Atom exchange between aqueous Fe(II) and goethite: an Fe isotope tracer study. *Environ. Sci. Technol.* 2009; 43: 1102-1107.
- [185] Pedersen HD, Postma D, Jakobsen R, Larsen O. Fast transformation of iron oxyhydroxides by the catalytic action of aqueous Fe(II). *Geochim. Cosmochim. Acta* 2005; 69: 3967-3977.
- [186] Drits VA, Sakharov BA, Salyn AL, Manceau A. Structural model for ferrihydrite. *Clay Miner.* 1993; 28: 185-207.
- [187] Rubasinghege G, Lentz RW, Park H, Scherer MM, Grassian VH. Nanorod dissolution quenched in the aggregated state. *Langmuir* 2010; 26: 1524-1527.
- [188] Schott J, Brantley S, Crerar D, Guy C, Borcsik M, Willaime C. Dissolution kinetics of strained calcite. *Geochim. Cosmochim. Acta* 1989; 53: 373-382.
- [189] Lasaga AC, Luttge A. Variation of crystal dissolution rate based on a dissolution stepwave model. *Science* 2001; 291: 2400-2404.
- [190] Kraemer SM, Hering JG. Influence of solution saturation state on the kinetics of ligand-controlled dissolution of oxide phases. *Geochim. Cosmochim. Acta* 1997; 61: 2855-2866.
- [191] Reichard PU, Kretzschmar R, Kraemer SM. Dissolution mechanisms of goethite in the presence of siderophores and organic acids. *Geochim. Cosmochim. Acta* 2007; 71: 5635-5650.
- [192] Miller WP, Zelazny LW, Martens DC. Dissolution of synthetic crystalline and noncrystalline iron oxides by organic acids. *Geoderma* 1986; 37: 1-13.
- [193] Johnson SE, Loeppert RH. Role of organic acids in phosphate mobilization from iron oxide. *Soil Sci. Soc. Am. J.* 2006; 70: 222-234.
- [194] Kirk GJD, Santos EE, Santos MB. Phosphate solubilization by organic anion excretion from rice growing in aerobic soil: rates of excretion and decomposition, effects on rhizosphere pH and effects on phosphate solubility and uptake. *New Phytol.* 1999; 142: 185-200.
- [195] Gahoonia TS, Asmar F, Giese H, Gissel-Nielsen G, Erik Nielsen N. Root-released organic acids and phosphorus uptake of two barley cultivars in laboratory and field experiments. *Europ. J. Agronomy* 2000; 12: 281-289.
- [196] Taylor R, Coulombe S, Otanicar T, Phelan P, Gunawan A, Lv W, Rosengarten G, Prasher R, Tyagi H. Small particles, big impacts: a review of the diverse applications of nanofluids. *J. Appl. Phys.* 2013; 113.
- [197] Albanese A, Tang PS, Chan WCW, in: *Annu. Rev. Biomed. Eng.*, Yarmush ML, Duncan JS, Gray ML, (Eds.) 2012; Vol. 14, pp 1-16.

[198] Bonanni PS, Schrott GD, Busalmen JP. A long way to the electrode: how do *Geobacter* cells transport their electrons? *Biochem. Soc. T.* 2012; 40: 1274-1279.

## Appendix

**Tab. A3.1:** Measured values of Fig. 3.2 a. Data indicate total iron concentrations in mM, measured with phenanthroline (phen), ferrozine, or ICP-OES.

1 M HCl, 21 °C					
	phen	SD	ferrozine	SD	ICP
Fe(II)	9,5	0,2	8,0	0,4	9,2
Fe(III)	8,9	0,1	7,7	0,6	8,6
Fe(II)/(III)	9,6	0,2	9,9	0,7	8,6
Fh	54,1	0,7	48,4	2,1	51,4
Magn	29,8	0,7	27,7	1,3	31,3
GtM	7,9	0,1	14,6	1,6	36,0
Gt	0,8	0,0	0,5	0,1	9,5

6 M HCl, 21 °C					
	phen	SD	ferrozine	SD	ICP
Fe(II)	10,2	0,2	10,5	2,6	9,3
Fe(III)	9,4	0,2	7,7	0,6	8,6
Fe(II)/(III)	9,9	0,1	10,3	1,5	8,9
Fh	56,4	1,0	51,5	1,7	51,4
Magn	25,4	0,5	23,5	0,1	31,3
GtM	40,1	0,6	35,8	1,2	36,0
Gt	4,1	0,1	2,2	0,3	7,8
Py	4,3	0,1	11,7	0,3	34,7

6 M HCl, 60 °C					
	phen	SD	ferrozine	SD	ICP
Fe(II)	9,7	0,2	9,2	0,1	9,3
Fe(III)	9,3	0,1	8,5	0,2	8,6
Fe(II)/(III)	9,4	0,1	9,2	0,5	8,9
Fh	56,8	1,6	50,5	1,6	51,4
Magn	32,9	0,6	30,1	1,5	31,3
GtM	38,9	0,2	35,6	0,7	36,0
Gt	7,6	0,1	9,4	0,9	8,7
Py	31,7	0,7	50,3	1,3	34,7

**Tab. A3.2:** Measured values of Fig. 3.2 b. Data indicate ferrous iron concentrations in mM, measured with phenanthroline (phen) and ferrozine.

1 M HCl, 21 °C				
	phen	SD	ferrozine	SD
Fe(II)	9,1	0,1	10,6	0,1
Fe(II)/(III)	0,6	0,0	0,4	0,1
Fh	0,3	0,0	0,4	0,0
Magn	12,7	0,2	11,5	1,0
GtM	2,1	0,1	0,8	0,4

6 M HCl, 21 °C				
	phen	SD	ferrozine	SD
Fe(II)	10,8	0,3	9,7	0,2
Fe(II)/(III)	0,1	0,0	0,2	0,0
Fh	0,1	0,0	0,3	0,1
Magn	11,3	0,2	10,9	1,1
GtM	8,9	0,2	7,5	0,6
Py	10,1	0,1	6,2	0,6

6 M HCl, 60 °C				
	phen	SD	ferrozine	SD
Fe(II)	1,3	0,0	1,2	0,1
Fe(II)/(III)	0,0	0,0	0,0	0,0
Fh	0,5	0,0	0,5	0,0
Magn	2,3	0,0	3,0	0,1
GtM	1,7	0,1	2,2	0,0
Py	38,6	0,4	26,1	3,0

**Tab. A3.3:** Measured values of Fig. 3.2 c. Data indicate ferrous iron concentrations in mM, measured with phenanthroline and ferrozine.

	Phenanthroline				Ferrozine			
	oxic 60 °C	SD	anoxic 60 °C	SD	oxic 60 °C	SD	anoxic 60 °C	SD
Fe(II)	1,4	0,0	2,5	0,0	1,2	0,1	2,3	0,0
Fe(II)/(III)	0,0	0,0	-0,1	0,0	0,0	0,0	0,0	0,0
Magn	3,5	0,0	4,6	0,0	3,0	0,1	3,7	0,0
GtM	2,5	0,1	3,2	0,1	2,2	0,0	2,7	0,0
Fh	0,5	0,0	1,0	0,1	0,5	0,0	0,9	0,1

**Tab. A3.4:** Measured values of Fig. 3.3. Data indicate ferrous iron concentrations in mM, measured with ferrozine.

time [min]	Fe = 0,7 mM	SD	Fe = 1,4 mM	SD
0	0,00	0,00	0,00	0,00
3	0,07	0,02	0,06	0,05
5	0,11	0,05	0,11	0,04
7	0,13	0,03	0,30	0,03
10	0,14	0,02	0,33	0,03
30	0,12	0,03	0,27	0,05

**Tab. A3.5:** Measured values of Fig. 3.4a. Data indicate total iron concentrations in mM. Total Fe concentration measured with ICP-OES was 51.74 mM.

1M, 21 °C				6M, 21 °C				6M, 60 °C				
phen	SD	ferrozine	SD	phen	SD	ferrozine	SD	phen	SD	ferrozine	SD	
58,48	3,81	61,48	1,89	58,96	7,82	52,00	2,48	59,60	2,44	53,18	2,36	
57,64	0,99	43,71	4,58	56,51	0,63	51,29	3,58	57,70	0,43	50,02	2,12	
55,89	0,54	53,02	2,53	60,27	2,27	47,32	2,88	60,05	0,54	49,47	0,54	
57,74	0,60	52,51	1,63	59,78	1,28	49,85	2,74	59,60	1,87	48,88	1,00	
65,07	1,76	53,94	0,64	61,70	0,87	52,11	0,98	63,16	0,20	53,21	1,34	
58,23	1,22	51,88	2,75	58,33	1,00	47,83	0,78	60,19	1,39	47,92	2,62	
58,72	1,46	50,91	2,01	58,70	0,62	47,93	0,62	57,47	0,41	48,78	0,69	
53,66	0,90	50,97	0,50	54,79	0,20	52,92	0,48	57,93		55,43	0,93	
49,86	0,35	48,94	0,71	53,27	0,31	52,38	0,33	56,64	0,19	55,44	0,84	
49,27	0,37	47,62	0,75	57,04	0,43	55,82	0,61	57,56	0,03	56,67	0,80	
53,00	1,13	50,38	4,88	55,62	0,92	54,22	1,46	55,30	0,97	54,14	0,96	
<b>mean</b>	<b>56,14</b>	<b>4,51</b>	<b>51,40</b>	<b>4,39</b>	<b>57,72</b>	<b>2,53</b>	<b>51,24</b>	<b>2,74</b>	<b>58,65</b>	<b>2,14</b>	<b>52,10</b>	<b>3,16</b>

**Tab. A3.6:** Measured values of Fig. 3.4b. Data indicate ferrous iron concentrations in mM under anoxic conditions.

time [h]	1M, 21 °C				6M, 21 °C				6M, 60 °C			
	phen	SD	ferrozine	SD	phen	SD	ferrozine	SD	phen	SD	ferrozine	SD
0,00	1,4	0,1	0,6	0,2	0,3	0,0	0,8	0,0	0,0	0,0	-0,1	0,1
23,75	1,8	0,2	1,3	0,2	0,8	0,1	1,3	0,0	0,3	0,1	0,5	0,1
46,50	2,0	0,8	0,7	0,1	0,5	0,1	1,0	0,1	0,2	0,1	0,0	0,1
71,50	1,9	0,0	0,9	0,1	0,7	0,1	1,3	0,1	0,6	0,1	0,4	0,2
93,50	2,0	1,9	1,4	0,1	0,8	0,0	1,3	0,1	0,0	0,4	-0,5	0,1
164,50	3,5	0,1	2,5	0,2	2,1	0,1	2,3	0,3	1,1	0,1	0,5	0,1
237,00	15,3	0,4	10,5	1,3	12,5	0,3	10,7	0,3	6,5	0,1	5,0	0,6
351,50	26,9	1,3	23,4	1,9	24,9	3,0	30,4	9,8	-0,1	0,2	-0,1	0,2
503,75	24,8	0,2	24,0	3,0	23,6	1,0	27,9	11,2	9,2	0,1	7,2	1,7
552,00	26,1	0,8	25,0	2,3	23,3	0,3	22,8	2,2	16,4	0,7	12,3	2,7
597,50	26,9	0,3	34,4	1,4	24,7	0,8	16,4	4,8	1,4	0,1	1,0	0,7

**Tab. A3.7:** Measured values of Fig. 3.4c. Data indicate ferrous iron concentrations in mM under oxic conditions.

time [h]	1M, 21 °C				6M, 21 °C				6M, 60 °C			
	phen	SD	ferrozine	SD	phen	SD	ferrozine	SD	phen	SD	ferrozine	SD
0,00	2,1	0,2	2,1	0,1	0,1	0,0	0,6	0,0	0,0	0,0	0,5	0,0
23,75	1,6	0,1	1,7	0,0	0,1	0,0	0,5	0,0	0,0	0,0	0,3	0,0
46,50	1,6	0,0	2,0	0,0	0,1	0,0	0,7	0,0	0,0	0,0	0,6	0,0
71,50	1,8	0,1	2,0	0,2	0,1	0,0	0,7	0,0	0,0	0,0	0,3	0,0
93,50	1,9	0,0	2,1	0,2	0,1	0,0	0,9	0,0	0,0	0,0	0,4	0,1
164,50	3,5	0,0	3,4	0,1	0,1	0,0	1,3	0,0	0,0	0,0	0,5	0,1
237,00	15,5	0,1	15,8	0,5	0,1	0,0	4,3	0,4	0,0	0,0	0,5	0,0
351,50	25,1	1,1	19,7	0,8	1,7	0,0	1,9	0,0	0,2		0,3	0,0
503,75	25,1	0,4	20,5	1,8	6,6	0,0	7,0	0,1	0,3	0,1	0,3	0,0
552,00	24,5	0,2	11,3	2,9	9,4	0,0	9,6	0,2	0,3	0,0	0,4	0,0
597,50	24,0	0,6	9,8	0,7	3,9	0,0	4,2	0,1	0,2	0,0	0,4	0,0

**Tab. A3.8:** Measured values of Fig. 3.5. Data indicate total Fe (Fe(tot)), ferrous Fe (Fe(II)), and ICP-OES concentrations in mM.

	Fe(tot)				
	ferrozine	SD	phen	SD	ICP
Fe(II)	4,5	0,1	4,1	0,1	4,4
N <sub>2</sub> /CO <sub>2</sub>	4,6	0,0	4,2	0,1	4,4
Medium	5,9	0,1	5,4	0,0	5,5
Medium + N <sub>2</sub> /CO <sub>2</sub>	6,0	0,2	5,7	0,1	5,5
Acetate	4,9	0,1	4,4	0,0	4,5
Acetate + N <sub>2</sub> /CO <sub>2</sub>	5,2	0,0	4,5	0,0	4,5
TE	8,4	0,2	9,7	0,0	10,6
7Vits	7,1	0,1	6,3	0,1	7,5

	Fe(II)			
	ferrozine	SD	phen	SD
Fe(II)	3,9	0,1	4,6	0,2
N <sub>2</sub> /CO <sub>2</sub>	4,2	0,0	4,9	0,1
Medium	5,0	0,1	5,9	0,1
Medium + N <sub>2</sub> /CO <sub>2</sub>	5,1	0,1	6,1	0,1
Acetate	4,1	0,1	4,8	0,1
Acetate + N <sub>2</sub> /CO <sub>2</sub>	4,3	0,1	5,1	0,0
TE	10,1	0,4	9,7	0,1
7Vits	9,5	0,4	9,2	0,1



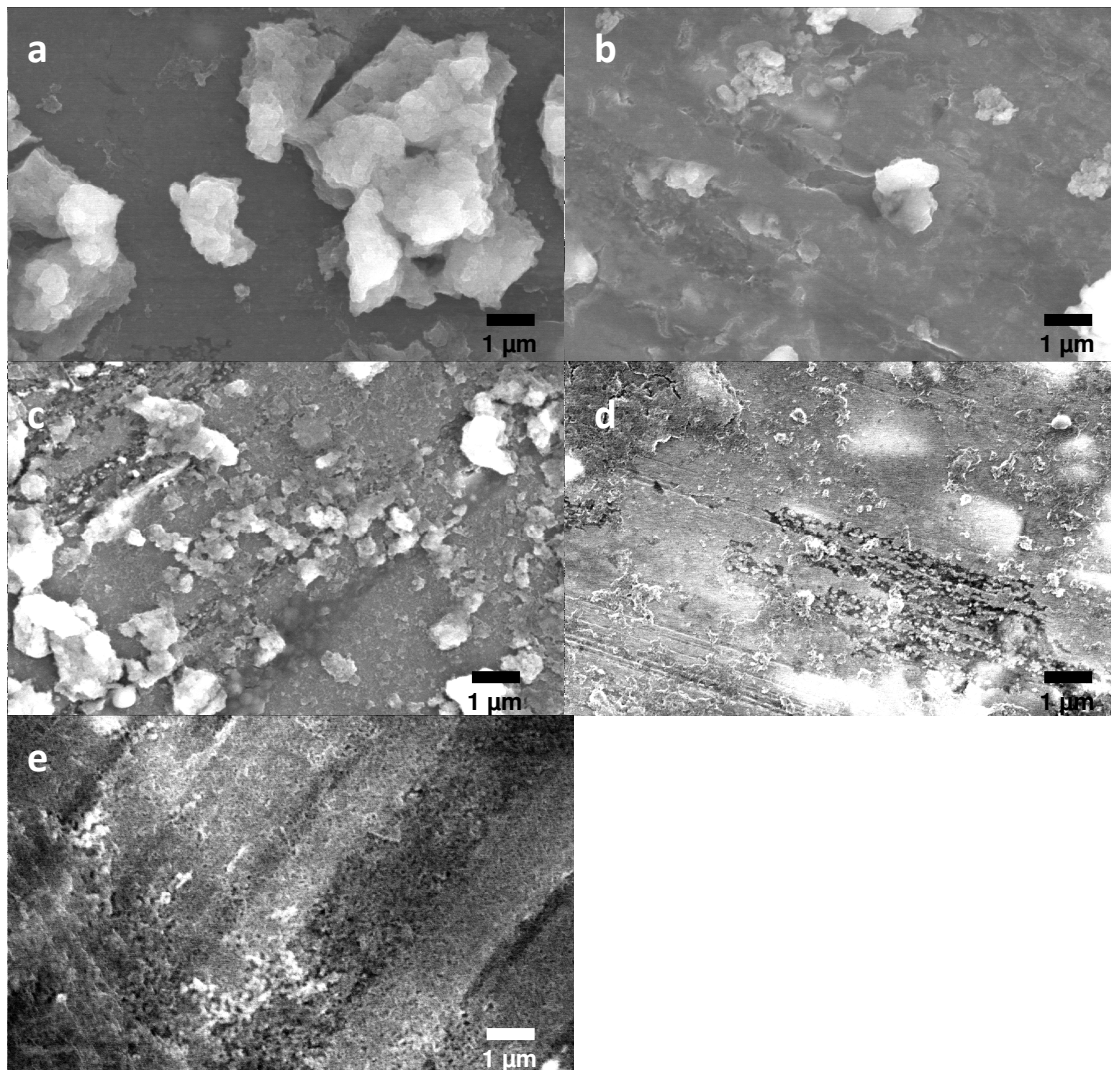
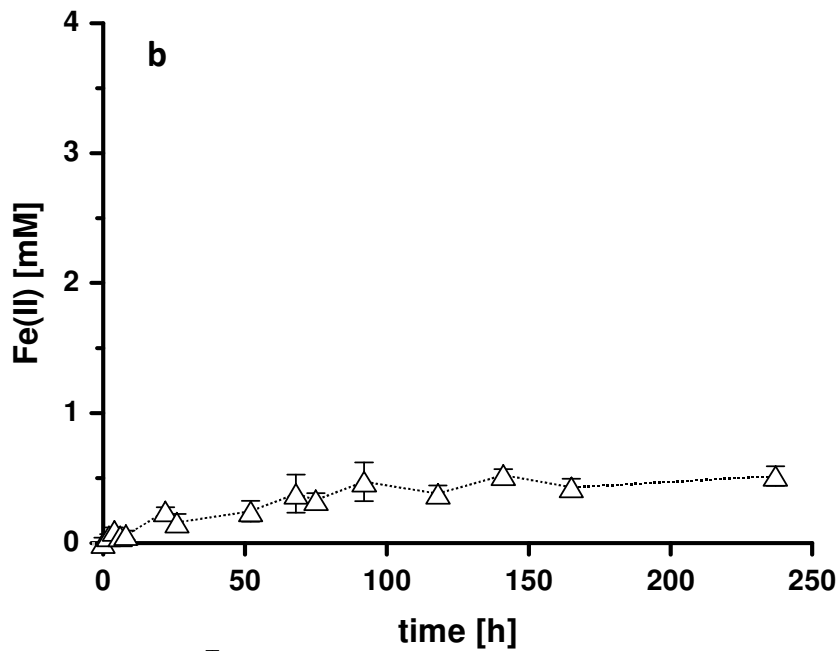
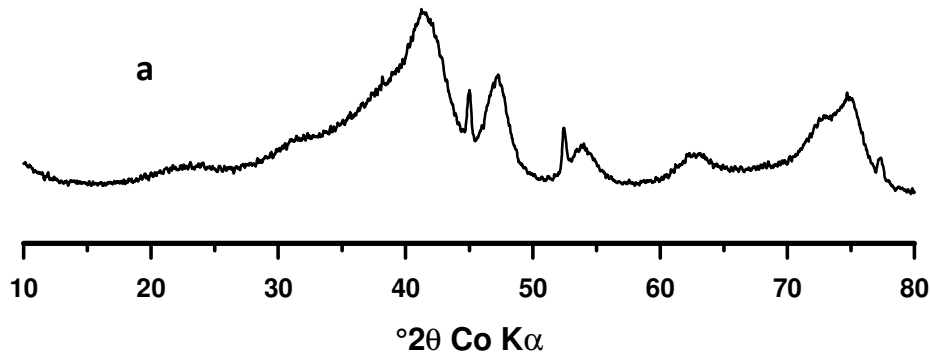
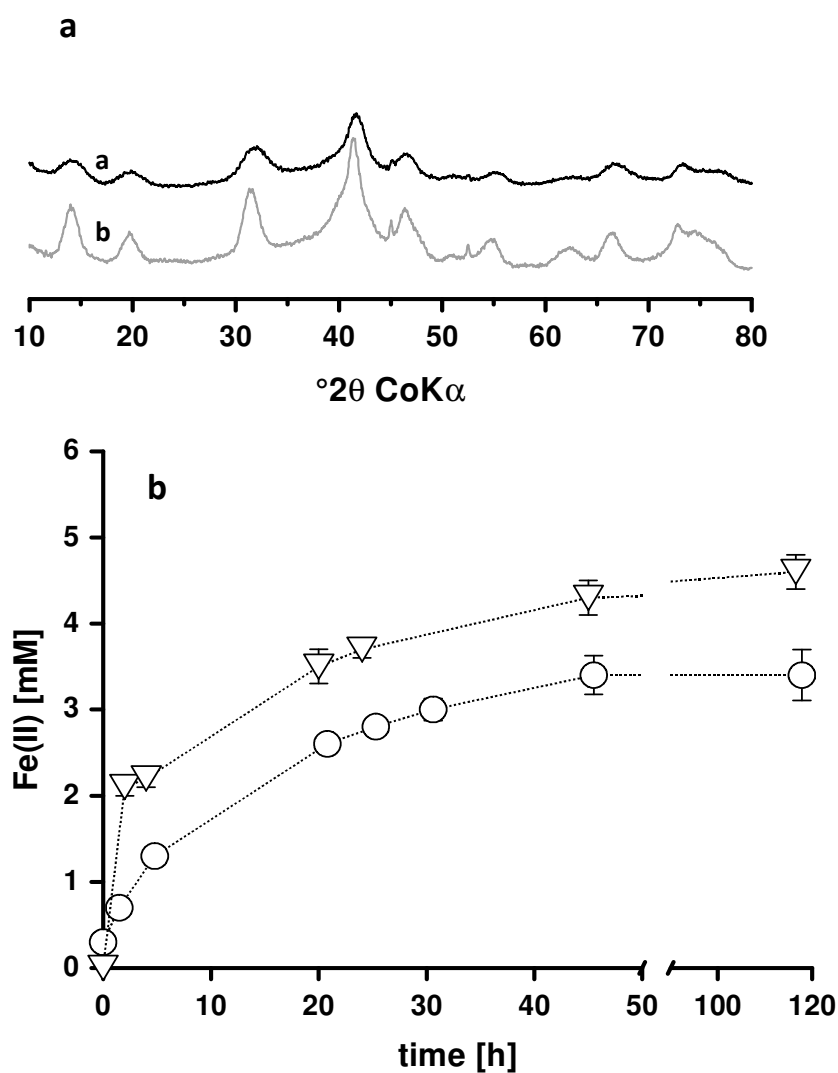


Fig. A4.1: SEM images of 2LFh 1 (a), 2LFh 2 (b), 2LFh 3 (c), 6LFh 1 (d), and 6LFh 2 (e). Single particles form crust-like structures of several  $\mu\text{m}$ . Furrows are caused from sample holder.



**Fig. A4.2:** XRD pattern of 6LFh 2 without detectable secondary minerals (a). Peaks at 44 and 52°2θ stem from aluminum sample holder. Microbial reduction by *G. sulfurreducens* of 6LFh 2 is very slow with 0.006 mM Fe(II) h<sup>-1</sup> (b). Error bars depict standard deviations of triplicate batch incubations.



**Fig. A4.3:** XRD diffractogram of additional ferrihydrite preparation after Larsen and Postma (LM, a), containing a significant amount of akaganeite, similar to 2LFh 3 (b) (a). Abiotic reduction kinetics of 2LFh 3 and the additional preparation (LM) in ascorbic acid (b). Experiments were conducted under anoxic conditions in 40 mL batch incubations. Samples for ferrous iron (Fe(II)) determination were taken at different time points and centrifuged for 30 sec at 9,660 x g. Aliquots of 100  $\mu$ L of the supernatant were stabilized against reoxidation in 1 M HCl and subsequently measured with the ferrozine assay. Total Fe concentration for 2LFh 3 ( $\nabla$ ) is  $5.8 \pm 0.2$  mM and for LM ( $\circ$ ) is  $3.8 \pm 0.2$ . Hydrodynamic diameter of LM is 5 nm with a BET specific surface area of  $267.2 \pm 0.6$   $\text{m}^2 \text{g}^{-1}$ . In both preparations no micropores were detected. Error bars depict standard deviations of triplicate batch incubations.

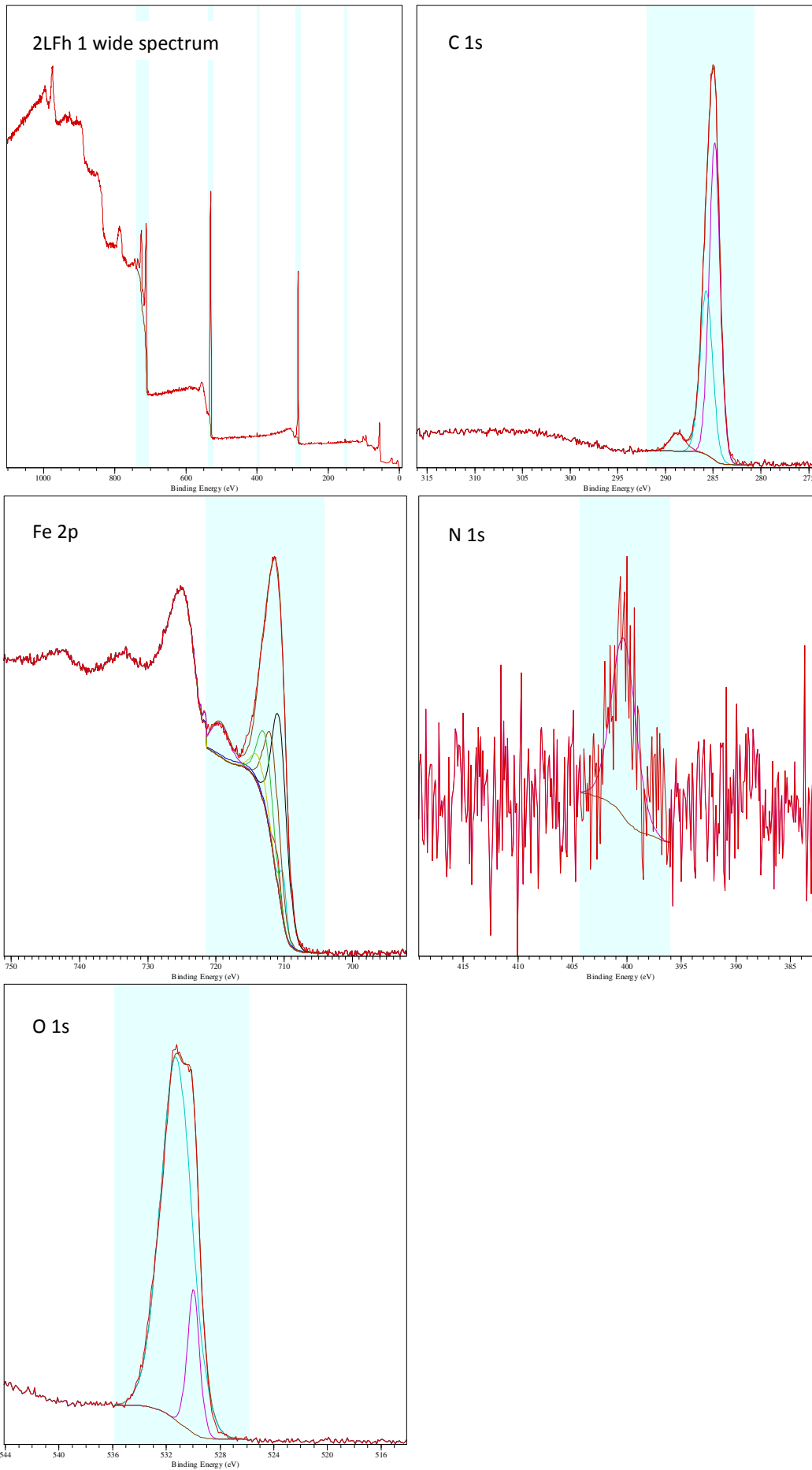


**Fig. A4.4:** XPS spectra of 2LFh 1.

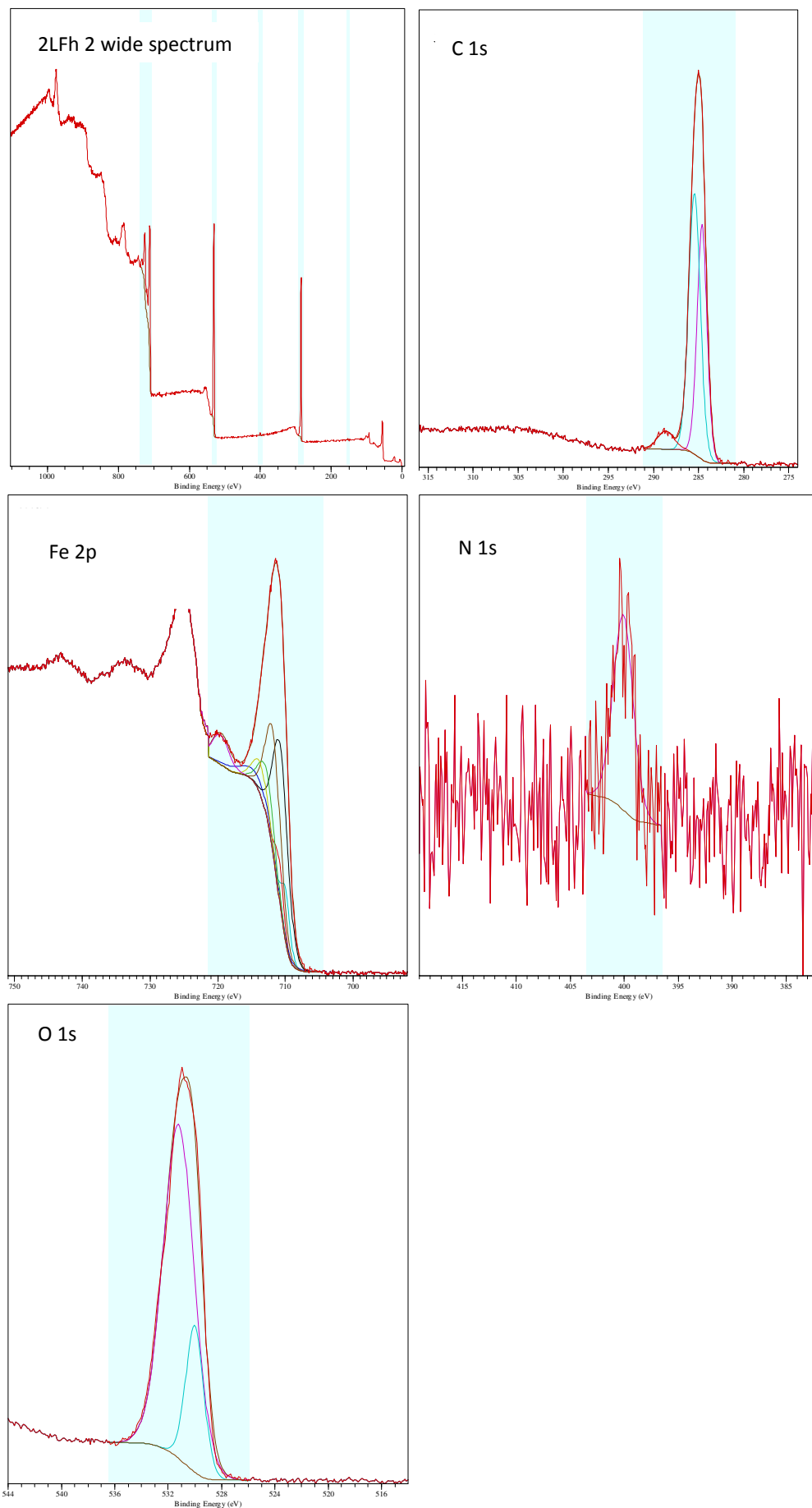


**Fig. A4.5:** XPS spectra of 2LFh 2.

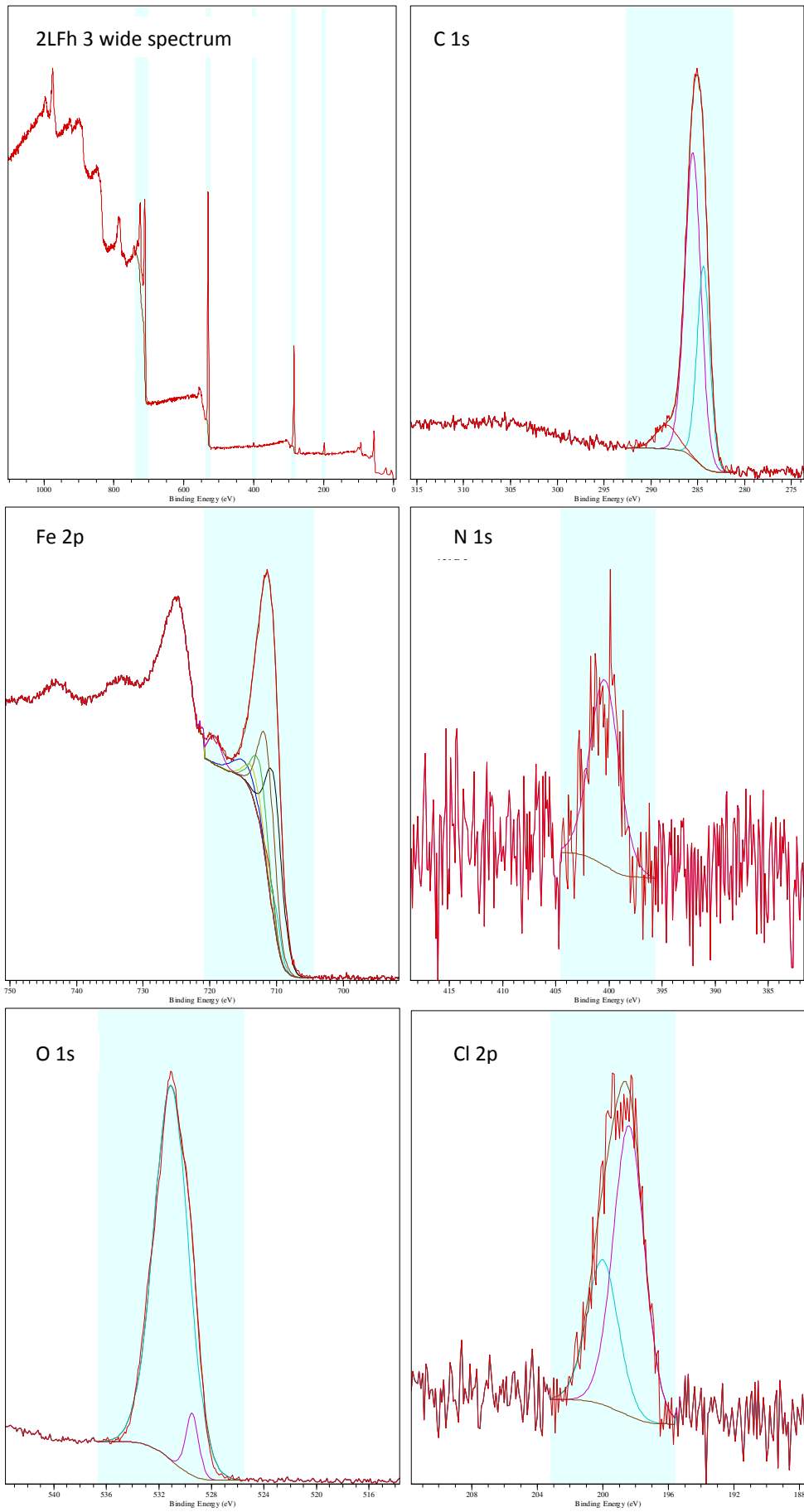


**Fig. A4.6:** XPS spectra of 2LFh 3.

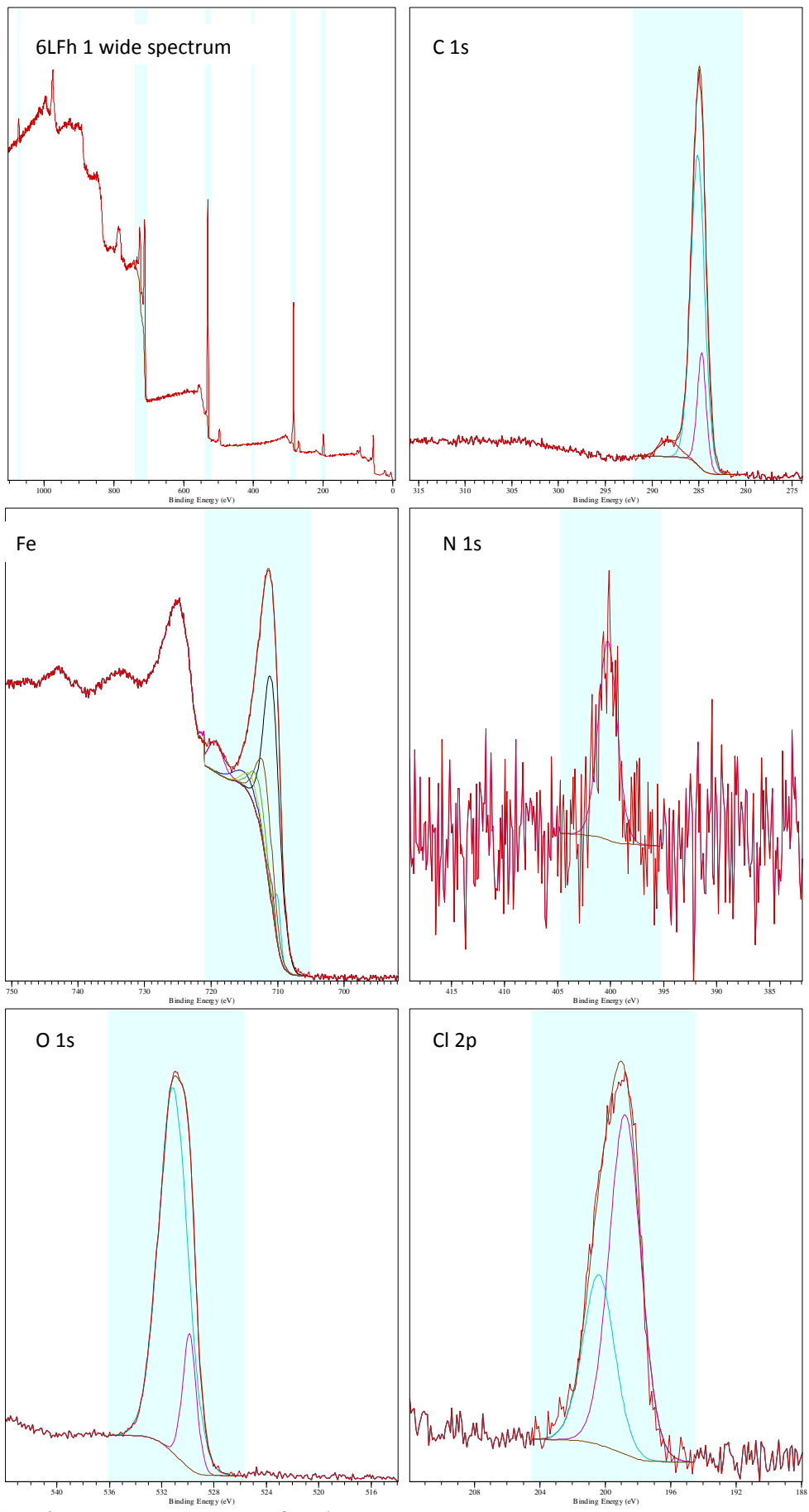


**Fig. A4.7:** XPS spectra of 6LFh 1.

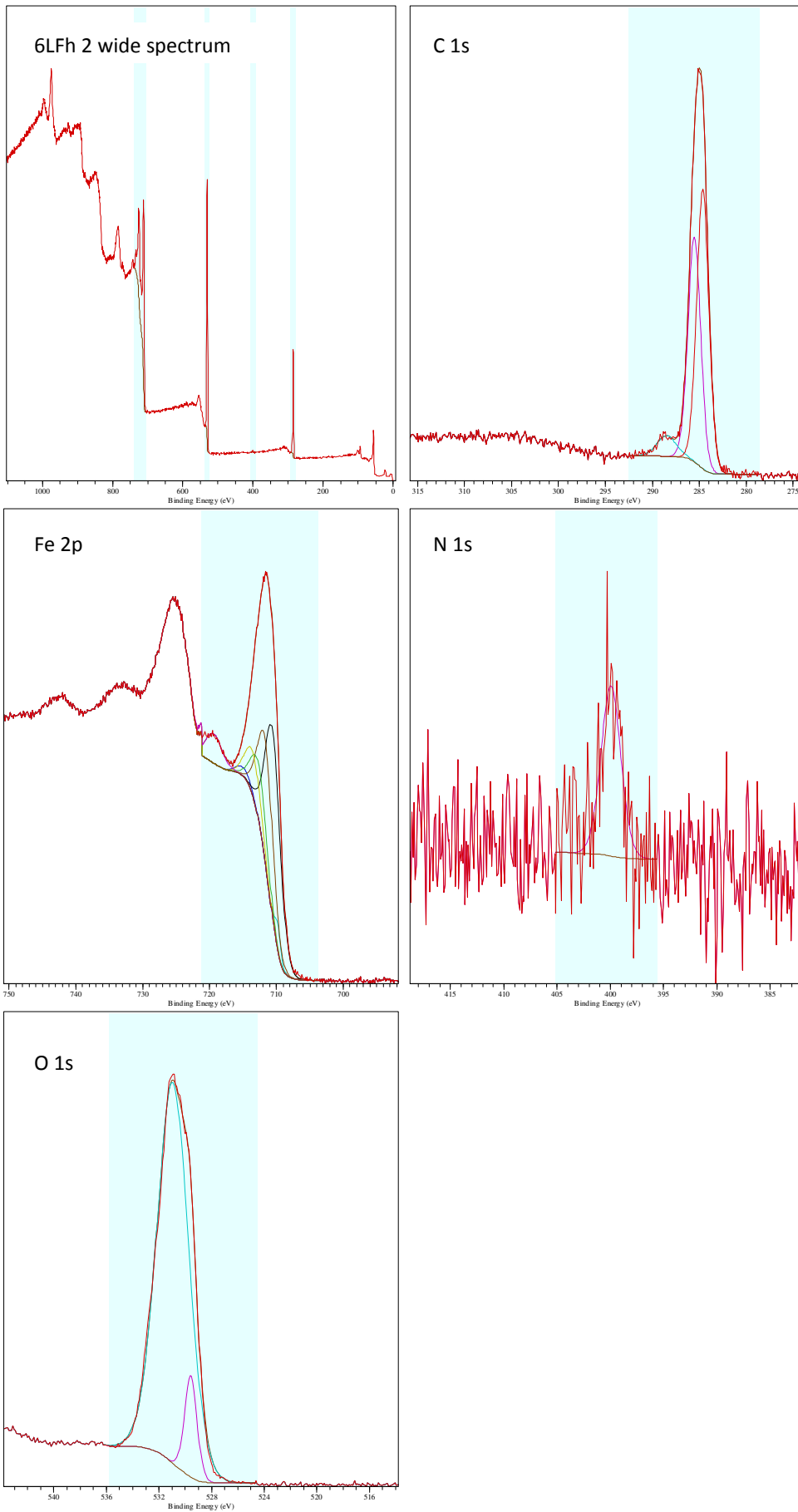


Fig. A4.8: XPS spectra of 6LFh 2.



**Tab. A4.1:** Measured values of Fig. 4.3a, the abiotic reduction experiment with ascorbic acid. Ferrous iron concentrations are given in mM.

time [h]	2LFh 1 (4,8 mM)	SD	time [h]	2LFh 2 (4,1 mM)	SD	time [h]	2LFh 3 (5,8 mM)	SD	time [h]	6LFh 1 (5,2 mM)	SD	time [h]	6LFh 2 (4,6 mM)	SD
0,0	0,0	0,1	0,0	0,0	0,1	0,0	0,0	0,0	0,0	0,0	0,0	0,0	0,0	0,0
0,5	1,6	0,1	0,5	0,9	0,1	2,0	2,1	0,1	0,5	1,2	0,1	2,0	1,6	0,1
2,0	3,0	0,2	3,7	2,8	0,2	4,0	2,2	0,1	3,0	3,0	0,2	4,0	1,9	0,1
17,7	3,6	0,0	19,0	3,4	0,1	20,0	3,5	0,2	19,0	3,9	0,1	20,0	2,9	0,2
22,0	3,5	0,2	24,0	3,7	0,2	24,0	3,7	0,1	23,0	4,0	0,1	24,0	2,9	0,1
43,0	4,9	0,6	45,0	4,2	0,4	45,0	4,3	0,2	44,0	4,5	0,1	45,0	3,5	0,2
114,5	4,6	0,1	116,5	4,3	0,1	116,5	4,6	0,2	115,5	4,5	0,1	116,5	3,6	0,3

**Tab. A4.2:** Measured values of Fig. 4.3b, the microbial reduction experiment with *Geobacter sulfurreducens*. Ferrous iron concentrations are given in mM.

time [h]	2LFh 1 (4,8 mM)	SD	2LFh 2 (4,7 mM)	SD	2LFh 3 (5,0 mM)	SD	6LFh 1 (4,9 mM)	SD	6LFh 2 (4,2 mM)	SD
0,0	0,17	0,02	0,15	0,03	0,14	0,01	0,10	0,01	0,13	0,02
3,25	0,09	0,00	0,08	0,01	0,08	0,01	0,08	0,01	0,08	0,00
7,75	0,09	0,01	0,08	0,00	0,07	0,01	0,09	0,01	0,08	0,01
22,25	0,08	0,02	0,08	0,02	0,07	0,01	0,12	0,03	0,08	0,01
27,75	0,07	0,01	0,10	0,02	0,07	0,00	0,12	0,01	0,08	0,01
46,25	0,07	0,01	0,16	0,06	0,08	0,01	0,15	0,01	0,08	0,02
54,75	0,06	0,00	0,19	0,08	0,08	0,02	0,18	0,02	0,08	0,01
94,25	0,23	0,02	0,46	0,17	0,20	0,01	0,29	0,01	0,20	0,02
171,25	0,18	0,03	0,72	0,19	0,14	0,04	0,44	0,04	0,14	0,06
215,25	0,72	0,07	1,29	0,18	0,64	0,05	0,96	0,05	0,61	0,02
382,25	0,87	0,16	1,89	0,43	0,72	0,14	1,43	0,05	0,60	0,08
440,5	0,90	0,10	1,94	0,56	0,52	0,15	1,15	0,07	0,32	0,08
503,25	1,51	0,09	2,36	0,52	1,09	0,19	1,58	0,04	0,82	0,09
575,25	0,91	0,17	2,26	0,57	0,52	0,19	1,26	0,05	0,29	0,08
669,25	0,90	0,22	2,51	0,59	0,45	0,22	1,22	0,07	0,19	0,11
935,25	1,97	0,36	5,42	1,04	1,07	0,54	2,54	0,10	0,39	0,24

**Tab. A4.3:** Measured values of Fig. 4.4, the dissolution of ferrihydrite in 1 M HCl. Total Fe concentrations are given in mM.

2LFh 1			2LFh 2			2LFh 3			6LFh 1			6LFh 2		
time [min]	(8,5 mM)	SD	time [min]	(9,2 mM)	SD	time [min]	(10,1 mM)	SD	time [min]	(9,1 mM)	SD	time [min]	(10,2 mM)	SD
0,0	9,00	0,21	0,0	7,74	1,57	0,0	4,93	0,31	0,0	8,11	1,30	0,0	4,66	0,20
2,0	9,01	0,14	2,0	9,48	0,10	2,0	6,96	0,26	2,0	9,46	0,11	2,0	4,47	0,11
5,0	8,76	0,26	5,0	9,59	0,31	5,0	6,44	0,13	5,0	9,59	0,07	5,0	5,21	0,15
8,0	8,50	0,05	8,0	9,28	0,30	8,0	6,77	0,02	8,0	9,31	0,28	8,0	5,84	0,26
11,0	8,40	0,05	11,0	9,46	0,43	11,0	6,82	0,17	11,0	9,05	0,27	11,0	6,43	0,19
15,0	8,11	0,18	15,0	9,50	0,38	15,0	7,38	0,19	15,0	9,00	0,26	15,0	7,13	0,14
30,0	7,82	0,30	30,0	9,67	0,33	30,0	9,82	0,23	30,5	8,91	0,32	30,0	8,22	0,26

**Tab. A5.1:** Measured values of Fig. 5.2a, the dissolution kinetics of ferrihydrite with citrate. Total Fe concentrations are given in mM.

time [h]	0.0 mM citrate	SD	0.05 mM citrate	SD	0.37 mM citrate	SD	0.75 mM citrate	SD	1.64 mM citrate	SD	4.75 mM citrate
0,0	0,00	0,00	0,00	0,01	0,00	0,02	0,00	0,01	0,00	0,01	0,00
2,5	0,03	0,01	0,03	0,02	0,08	0,05	0,08	0,00	0,13	0,01	0,13
5,0	0,02	0,01	0,02	0,01	0,09	0,01	0,14	0,01	0,21	0,01	0,20
8,0	0,02	0,01	0,04	0,03	0,09	0,01	0,18	0,03	0,28	0,03	0,27
22,75	0,03	0,01	0,02	0,01	0,11	0,02	0,31	0,02	0,63	0,02	0,75
30,5	0,02	0,01	0,02	0,02	0,16	0,05	0,37	0,04	0,88	0,02	1,19
46,25	0,04	0,01	0,02	0,01	0,14	0,04	0,53	0,05	1,49	0,07	1,89
54,75	0,10	0,10	0,05	0,01	0,14	0,04	0,62	0,05	1,78	0,13	2,34
70,25	0,05	0,01	0,02	0,01	0,16	0,06	0,88	0,03	2,49	0,13	2,79
173,5	0,05	0,03	0,05	0,03	0,18	0,11	1,29	0,04	3,38	0,25	2,98
total Fe	3,1	0,6	3,6	0,1	3,4	0,2	3,5	0,3	3,6	0,4	2,8

**Tab. A5.2:** Measured values of Fig. 5.2b, the dissolution kinetics of ferrihydrite with GoHy humic acids. Total Fe concentrations are given in mM.

time [h]	w/o OC	SD	1mg OC/L	SD	10mg OC/L	SD	30mg OC/L	SD
0,0	0,00	0,09	0,00	0,01	0,00	0,00	0,00	0,03
18,0	-0,02	0,03	0,04	0,04	-0,01	0,02	0,03	0,01
23,8	-0,01	0,05	0,03	0,04	-0,01	0,03	0,09	0,08
41,8	0,01	0,06	0,02	0,02	0,01	0,01	0,02	0,04
97,0	-0,05	0,02	0,08	0,05	-0,01	0,01	0,05	0,03
217,5	0,06	0,08	0,11	0,05	0,01	0,02	0,02	0,05
267,5	0,07	0,05	0,08	0,04	0,01	0,05	0,04	0,01
440,5	-0,02	0,03	0,06	0,09	0,02	0,02	0,03	0,03
1706,5	-0,01	0,04	0,10	0,09	0,11	0,08	0,10	0,03

**Tab. A5.3:** Measured values of Fig. 5.2c, colloid sizes, citrate, and Fe concentrations. Hydrodynamic diameters ( $d_h$ ) are given in nm, concentrations in mM.

Citr/Fe	citrate (0.45)		Citrate (0.22)		Fe (0.45)		Fe (0.22)		$d_h$ (0.45)		$d_h$ (0.22)		$d_h$ (not filt)	
		SD		SD		SD		SD		SD		SD		SD
0,0	0,00	0,02	-0,03	0,01	0,01	0,02	0,01	0,01						
0,01	0,00	0,03	0,05	0,01	0,03	0,00	0,02	0,01						
0,1	0,19	0,07	0,38	0,02	0,95	0,50	0,34	0,09	202	2	147	1		
0,2	0,59	0,05	0,75	0,04	2,02	0,21	1,33	0,11	196	13	134	11	612	147
0,5	1,62	0,03	1,64	0,07	3,45	0,29	3,41	0,21	153	11	106	6	128	54
1,7	4,78		4,75		3,13		3,20							

**Tab. A5.4:** Measured values of Fig. 5.3, the microbial reduction of ferrihydrite in presence of citrate. Ferrous Fe concentrations are given in mM.

time [h]	Citr/Fe = 0.0	SD	Citr/Fe = 0.03	SD	Citr/Fe = 0.14	SD	Citr/Fe = 0.27	SD	Citr/Fe = 0.58	SD
0,0	0,0	0,0	0,0	0,0	0,0	0,0	0,0	0,0	0,0	0,0
2,0	-0,3	0,0	0,0	0,0	0,2	0,0	0,1	0,0	0,1	0,0
4,0	-0,1	0,0	0,0	0,0	0,5	0,0	0,5	0,1	0,4	0,1
6,0	0,0	0,0	0,1	0,0	0,8	0,0	1,1	0,1	0,9	0,3
8,0	0,1	0,0	0,2	0,0	1,2	0,1	1,3	0,1	1,6	0,3
10,0	0,2	0,0	0,2	0,0	1,5	0,1	1,8	0,2	2,0	0,2
24,0	0,6	0,1	0,5	0,0	2,5	0,2	2,6	0,3	3,5	0,1
28,0	0,8	0,1	0,6	0,0	2,6	0,1	3,0	0,2	3,5	0,0
32,0	1,0	0,1	0,8	0,0	2,9	0,2	3,1	0,2	3,9	0,2
48,0	1,5	0,1	1,1	0,1	3,2	0,1	3,5	0,7	3,7	0,1
74,0	2,1	0,1	1,7	0,1	3,7	0,2	3,9	0,2	3,8	0,1
99,25	2,3	0,2	2,1	0,1	3,7	0,3	4,1	0,2	4,1	0,5
121,25	2,6	0,1	2,6	0,2	4,2	0,2	3,9	0,4	3,9	0,1
193,5	2,4	0,1	2,8	0,4	4,0	0,2	4,0	0,1	3,9	0,3

## **Authorship clarifications**

### **Introduction – “Iron Oxide Nanoparticles in Geomicrobiology: From Biogeochemistry to Bioremediation”**

The PhD candidate structured the concept of the review paper together with Dr. Julian Bosch and Prof. Rainer U. Meckenstock. The text was written by the PhD candidate. The manuscript was submitted to *New Biotechnology* on 19.07.2012

Inclusion of the manuscript in a thesis or dissertation is permitted by the journal ([http://cdn.elsevier.com/assets/pdf\\_file/0008/108674/AuthorUserRights.pdf](http://cdn.elsevier.com/assets/pdf_file/0008/108674/AuthorUserRights.pdf)).

### **Chapter 3.1 and 4.1 – “Reevaluation of colorimetric iron determination methods commonly used in geomicrobiology”**

The idea and the concept for the experimental design were carried out by the PhD candidate, Dr. Julian Bosch, and Prof. Rainer U. Meckenstock. All experiments were done by the PhD candidate. Dr. Katja Heister performed the XRD measurements and Dr. Christine Kübeck modelled impacts of different medium additives on ferrozine and phenanthroline methods. The results were evaluated together with Dr. Julian Bosch, Dr. Christine Kübeck, and Prof. Rainer U. Meckenstock. The manuscript was written by the PhD candidate and published in *Journal of Microbiological Methods*. Inclusion of the manuscript in a thesis or dissertation is permitted by the journal (<http://www.elsevier.com/authors/author-rights-and-responsibilities#rights>).

### **Chapter 3.2 and 4.2 – “Low molecular weight organic acids influence microbial Fe oxide reduction via a dissolution-disaggregation mechanism”**

The idea of the project was elaborated by the PhD candidate, Dr. Julian Bosch, and Prof. Rainer U. Meckenstock. All experiments were planned and done by the PhD candidate. Mössbauer spectroscopy and FTIR spectroscopy measurements were conducted by Dr. Christian Schröder and Matthias Händel, respectively. For HPLC measurements the PhD candidate received help from Sviatlana Marozava. Calculations of abiotic dissolution and microbial reduction kinetics were done by the PhD candidate with helpful comments from Dr. Christine Stumpp and Dr.

Christine Klier. Results were evaluated together with Dr. Julian Bosch, Matthias Händel, Dr. Christian Schröder, Dr. Christine Klier, and Prof. Rainer U. Meckenstock. The chapters were written by the PhD candidate and are planned for submission in *Geochimica et Cosmochimica Acta*. Inclusion of the manuscript in a thesis or dissertation is permitted by the journal (<http://www.elsevier.com/authors/author-rights-and-responsibilities#rights>).

### **Chapter 3.3 and 4.3 – “Reduced biotic and abiotic reactivity of ferrihydrite nanoparticles below a critical aggregate size”**

The idea and the concept of the project were elaborated by the PhD candidate and Prof. Rainer U. Meckenstock. The experiments were planned by the PhD candidate. Biotic and abiotic reduction and dissolution experiments were done by the students Jiachao Li and Andreas Just under supervision of the PhD candidate. XRD, FTIR, and XPS spectroscopy measurements were done by Dr. Katja Heister, Matthias Händel, and Dr. Paul L. Wincott, respectively. SEM images were taken by Gabriele Mettenleiter. Results were discussed and evaluated together with Dr. Katja Heister, Matthias Händel, Dr. Julian Bosch, Dr. Paul L. Wincott, Prof. Jonathan R. Lloyd, Dr. Michaela Aichler, and Prof. Rainer U. Meckenstock. The manuscript was written by the PhD candidate and submitted to *Geochimica et Cosmochimica Acta* on 27.02.2013. Inclusion of the manuscript in a thesis or dissertation is permitted by the journal (<http://www.elsevier.com/authors/author-rights-and-responsibilities#rights>).

Prof. Rainer U. Meckenstock, Dr. Julian Bosch, Dr. Katja Heister, Dr. Christine Kübeck, Matthias Händel, Dr. Christian Schröder, Prof. Kai U. Totsche, Johannes Najjar, Dr. Michaela Aichler, Dr. Paul L. Wincott, and Prof. Jonathan R. Lloyd participated in proof-reading various parts of the thesis.

## Publications

- Fritzsche, A., Bosch, J., Rennert, T., Heister, K., **Braunschweig, J.**, Meckenstock, R.U., Totsche, K.U. Fast microbial reduction of ferrihydrite colloids from a soil effluent. *Geochim. Cosmochim. Acta* 2012; 77: 444-456
- Braunschweig, J.**, Bosch, J. Heister, K., Kuebeck, C., Meckenstock, R.U. Reevaluation of colorimetric iron determination methods commonly used in geomicrobiology. *J. Microbiol. Methods* 2012; 89: 41-48.
- Braunschweig, J.**, Bosch, J., Meckenstock, R.U. Iron Oxide nanoparticles in geomicrobiology: from biogeochemistry to bioremediation. *New Biotechnol.* (submitted on 19.07.2012).
- Braunschweig, J.**, Bosch, J., Heister, K., Händel, M., Totsche, K.U., Aichler, M. Wincott, P.L., Lloyd, J.R., Meckenstock, R.U. Inhibition of biotic and abiotic reactivity of ferrihydrite nanoparticles below a critical aggregate size. *Geochimica et Cosmochimica Acta* (submitted on 27.02.2013).
- Braunschweig, J.**, Klier, C., Schroeder, C., Händel, M., Totsche, K.U., Bosch, J., Meckenstock, R.U. Low molecular weight organic acids influence microbial Fe oxide reduction via a dissolution-disaggregation mechanism. *Geochim. Cosmochim. Acta* (in preparation).

## Acknowledgments

In particular I thank my supervisor Prof. Dr. Rainer U. Meckenstock for the opportunity to work on this research project, his scientific input in many discussions, and for giving me the freedom to follow my own ideas.

Furthermore, I gratefully acknowledge Prof. Dr. Ingrid Kögel-Knabner for her support in three thesis committee meetings and for accepting the position as chairwoman of the examination board. I also thank Prof. Dr. Kai U. Totsche for his interest to review the work as examiner. For financial support and valuable ideas I thank the research group FOR 580 of the German Research Foundation (DFG) “Electron Transfer Processes in Anoxic Aquifers”. I thank the European Science Foundation with the research networking programme FIMIN (The Functionality of Iron Minerals in Environmental Processes) for giving me the opportunity to attend a PHREEQC modelling workshop.

Particularly, I want to express my deep gratitude to Dr. Julian Bosch, who patiently introduced an unknowing geologist to the mysteries of microbiology, for answering my questions, for the successful application of different motivation strategies, and for proof-reading my manuscripts and this thesis over and over again.

The Anaerobic Degradation Group and the entire staff of the IGOE are gratefully acknowledged for their help and support and the nice working atmosphere during the last years. Especially Denise Lehmann, Simone Täuber, Jiachao Li, and Andreas Just have to be mentioned here for their support in the lab. I thank Janina Kölschbach for proof-reading of this thesis. Furthermore, I thank Dr. Christian Griebler for his attendance in the thesis committee meetings.

For creative suggestions and technical support I thank Dr. Katja Heister, Matthias Händel, Prof. Dr. Jonathan R. Lloyd, Dr. Paul L. Wincott, Dr. Christian Schröder, Prof. Dr. Bernhard Michalke, Gabriele Mettenleiter, and Sviatlana Marozava.

For his friendship, cooperation, and help I thank Dr. Andreas Fritzsche.

Most importantly my family and Johannes deserve my deepest gratitude for providing unconditional support whenever I needed them – Thank you.



# Lebenslauf

## Juliane Braunschweig

Geboren am 15.05. 1984 in Jena

- |                   |   |
|-------------------|---|
| 12/2009 – 02/2013 | Doktorandin am Helmholtz Zentrum München, Institut für Grundwasserökologie<br>Thema: Impact of organic acids and mineral properties on microbial iron oxide reduction |
| 03/2009 – 10/2009 | Diplomarbeit bei Prof. Dr. K. U. Totsche (LS Hydrogeologie, Friedrich-Schiller-Universität Jena)<br>Thema: Charakterisierung von heterogenen kolloidalen Fe-Oxiden    |
| 10/2004 – 10/2009 | Geologiestudium an der Friedrich-Schiller-Universität Jena<br>Schwerpunkt: Hydrogeologie  |
| 10/2003 – 09/2004 | Chemiestudium an der Friedrich-Schiller-Universität Jena  |
| 1995 – 2003       | Anger Gymnasium Jena<br>Leistungskurse: Deutsch, Biologie   |